CHEMICAL
REVIEWS

pubs.acs.org/CR

Review

Stacking Order Engineering of Two-Dimensional Materials and Device Applications

Published as part of Chemical Reviews virtual special issue "Phase Engineering of Nanomaterials".

Carter Fox,[#] Yulu Mao,[#] Xiang Zhang, Ying Wang, and Jun Xiao*

Cite This: https://doi.org/10.1021/acs.chemrev.3c00618

Read Online

ACCESS | Metrics & More | Article Recommendations

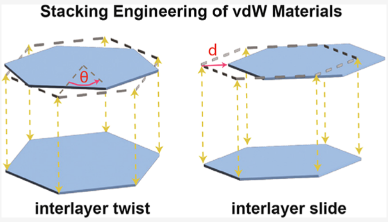

ABSTRACT: Stacking orders in 2D van der Waals (vdW) materials dictate the relative sliding (lateral displacement) and twisting (rotation) between atomically thin layers. By altering the stacking order, many new ferroic, strongly correlated and topological orderings emerge with exotic electrical, optical and magnetic properties. Thanks to the weak vdW interlayer bonding, such highly flexible and energy-efficient stacking order engineering has transformed the design of quantum properties in 2D vdW materials, unleashing the potential for miniaturized high-performance device applications in electronics, spintronics, photonics, and surface chemistry. This Review provides a comprehensive overview of stacking order engineering in 2D vdW materials and their device applications, ranging from the typical fabrication and characterization methods to the novel physical properties and the emergent slidetronics and twistronics device prototyping. The main emphasis is on the critical role of stacking orders affecting the interlayer charge transfer, orbital coupling and flat band formation for the design of innovative materials with on-demand quantum properties and surface potentials. By demonstrating a correlation between the stacking configurations and device functionality, we highlight their implications for next-generation electronic, photonic and chemical energy conversion devices. We conclude with our perspective of this exciting field including challenges and opportunities for future stacking order engineering research.

CONTENTS

1. Introduction B
1.1. Outline B
2. Stacking Order Engineering Enabled by Interlayer Sliding C
2.1. Characterization Methods to Probe Stacking Orders with Distinct Interlayer Sliding D
2.1.1. Raman Spectroscopy D
2.1.2. Second Harmonic Generation Spectroscopy E
2.1.3. Transmission Electron Microscopy F
2.1.4. Atomic Force Microscopy Techniques F
2.2. Sliding Ferroelectricity That Arises from Polar Stacking Orders F
2.2.1. Sliding Ferroelectricity in Natural and Artificial Stacking Orders G
2.2.2. Theoretical Understanding H
2.2.3. Experimental Realizations H
2.3. Engineering Approaches To Control Sliding Orders I
2.3.1. Ultrafast and Light-Driven Stacking Order Transitions I
2.3.2. Chemically Driven Sliding Order Transitions J
2.3.3. Mechanically Driven Sliding Order Transition K
2.4. Sliding Orders Coupled with Other Quantum Properties K
2.4.1. Sliding Orders Coupled with Magnetism L
2.4.2. Sliding Orders Coupled with Superconductivity L
3. Stacking Order Engineering Enabled by Interlayer Twist L
3.1. Moiré Geometry in Stacking Structures M
3.2. Assembly of Moiré Materials M
3.2.1. Tear-and-Stack Method for Homobilayer Moiré Superlattice M
3.2.2. Polymer Assisted Dry Transfer Method for Heterobilayer Moiré Superlattice N
3.2.3. Chemical Synthesis of Moiré Superlattice N
3.3. Twist Angle and Moiré Pattern Characterization N

Received: August 29, 2023
Revised: November 16, 2023
Accepted: December 6, 2023

- 3.3.1. Optical Spectroscopy to Identify Twist Angles N
- 3.3.2. Conductive AFM To Map Stacking Domains and Twist Angles O
- 3.3.3. TEM Imaging of Moiré Superlattices O
- 3.4. Novel Physical Properties in Twisted Stacking Orderings O
  - 3.4.1. Noncollinear Spin Textures in Moiré Magnets O
  - 3.4.2. Luttinger Liquid Phase in Rectangular Moiré Semimetals Q
  - 3.4.3. Topological Phenomena in Moiré Superlattices Q
  - 3.4.4. Novel Physical Properties in Multilayer Twist Systems S
  - 3.4.5. Surface Chemistry Influenced by Moiré Superlattices U
- 4. Stacking Order Engineering for Device Applications V
  - 4.1. Electrical Applications V
    - 4.1.1. Transistors V
    - 4.1.2. Memory Devices W
  - 4.2. Optical Applications W
    - 4.2.1. Photovoltaic Device W
    - 4.2.2. Quantum Emitter X
    - 4.2.3. Interlayer Exciton Laser Y
  - 4.3. Surface Chemical Applications Y
- 5. Summary and Prospect Z
  - 5.1. Repeatable and Large-Scale Stacking Material Synthesis and Processing Z
  - 5.2. Precise and High Throughput Theoretical Modeling AA
  - 5.3. Broadened Material Choices for Slidetronics and Twistronics AA
  - 5.4. Domain Kinetics and Ultrafast Dynamics in Stacking Engineered Materials and Devices AA
  - 5.5. New Chemical Functionality Enabled by Stacking Engineering AA
- Author Information AB
  - Corresponding Author AB
  - Authors AB
  - Author Contributions AB
  - Notes AB
  - Biographies AB
- Acknowledgments AB
- List of Abbreviations AB
  - Symbols AC
- References AC

1. INTRODUCTION

The emergence of artificial intelligence and 5G technology is transforming the world with novel applications such as the Internet of Things, smart manufacturing, and AI-empowered medical care. Driven by such an information revolution, global data usage is estimated to reach 175 zettabytes by 2025 and go beyond the capacity of current devices' capability. The relevant electricity consumption by 2030 would soar to more than 20% of global energy demand.[1,2] These aspects urge innovations in the materials and device platforms to surpass present units and the long-standing von Neumann architecture. To this end, the two-dimensional vdW materials are emerging as one of the top candidates thanks to their miniaturized dimensionality, various structural and electronic engineering degrees of freedom with atomically clean interface, as well as large electrical and strain tunability of their remarkable electronic, optical, and mechanical properties.[3−8]

vdW materials are built up by atomically thin layers with strong in-plane covalent bonds. Those atomic layers are weakly bonded together along out-of-plane via the weak vdW force, allowing for exfoliation down to the monolayer with atomically clean interfaces. This weak interlayer vdW bonding also unleashes the flexibility to form on-demand vdW stacking by controlling the relative crystallographic arrangement of atomic layers. Notably, this can be achieved without the need for lattice matching, a requirement that typically constrains the stacking of traditional 3D bulk materials. With the development of various synthesis methods and polymer-assisted transfer techniques,[9−13] the on-demand stacking of various vdW layers has become possible, leading to prior intriguing discoveries such as nontrivial topology in Weyl semimetals,[14,15] valleytronics in bulk 3R-MoS_2 and topological transport in bilayer-graphene domain walls.[16,17] More recently, sliding ferroelectricity arising from polar stacking of nonpolar monolayers such as WTe_2[18,19] and MoS_2[20] as well as strong electron correlation found in twisted bilayer graphene further motivate the control of phase competition to access hidden stacking orders for novel correlated physics and device applications.[21,22] These findings indicate the profound impact of the stacking order in determining crystal symmetry, redistributing charge and spin between neighboring layers, and thus controlling the strength of topological, electron correlation and spin properties.

The study of stacking orders and their phase transitions in vdW materials is intriguing, with multiple structural control degrees of freedom, including relative shifts and orientation angles between layers. This is fundamentally distinct from early studies focused on intralayer polymorphic phase changes, meaning atomic reconfiguration (e.g., ionic distortion, covalent bond breaking) occurs within one atomic layer including the 2H-1T-1T′ transition in $MoTe_2$,[23,24] ferroelectric-paraelectric transition in In_2Se_3 and SnTe,[25,26] and charge density wave formation in TaS_2,[27] which have been well reviewed.[7,28−30] However, phase transitions involving various stacking orders are fundamentally different, as they involve interlayer shifts and rotations governed by vdW forces, which are considerably weaker and thus more energy efficient than manipulating covalent bonds. The unbounded flexibility to integrate different compounds in stacking engineering for new heterostructures allows the exploration of the interplay of different quantum orderings from the parent components. For example, the formation of a moiré superlattice with controllable hopping strength and on-site Coulomb interactions enables a wide range of correlated quantum orderings that were previously inaccessible.[31−33] Finally, stacking orders can be controlled using various external stimuli such as electrical fields, optical pumping, and mechanical stress. These engineering approaches not only enable the creation of new stacking orders but also provide the foundation for the development of advanced electrical and optoelectronic devices based on stacking transitions.

1.1. Outline

The goal of this paper is to provide a comprehensive review on the stacking order engineering of two-dimensional materials and their device applications (Figure 1). We will primarily

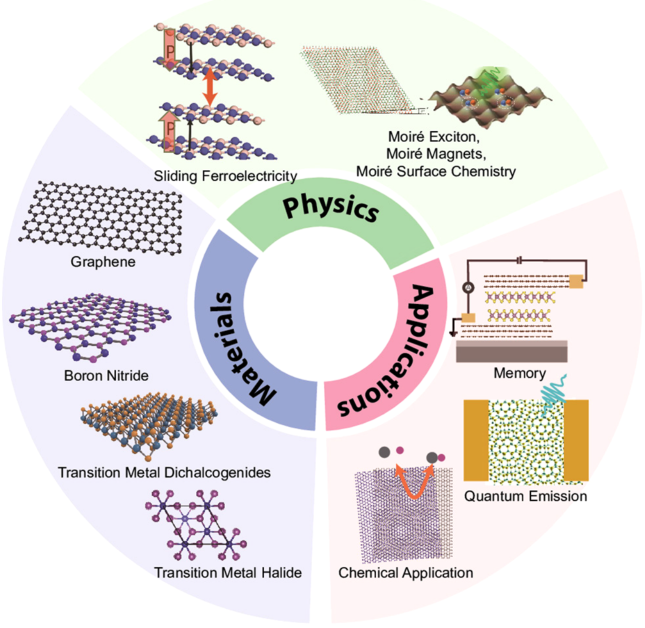

Figure 1. Overview of stacking order engineering of two-dimensional layered materials and their device applications.

cover the relevant literature after 2018, when studying physical properties associated with interlayer slide and twistronics began to emerge as a vital research frontier. Building upon the two distinct stacking degrees of freedom (slide and twist), we organize this Review into five sections. Following the Introduction, in section 2 we will first review the recent advance in sliding stacking orders and associated sliding phenomena such as sliding ferroelectricity, magnetism and their coupling with superconductivity. The section will introduce the background of sliding stacking orders in vdW materials and review characterization methods to identify stacking orders and reveal stacking transitions via sliding behaviors. Critical insights are offered on the structure−properties relationship and functional properties of sliding orderings. Along with such phase transitions, we will discuss how quantum orders are coupled to the sliding order, including sliding ferroelectricity, sliding controlled magnetism and superconductivity. Following this, engineering approaches to control the sliding behavior are also discussed to reveal their potential to control other properties like ferroelectricity and ferromagnetism. In section 3, we turn to interlayer twist, another degree of structural freedom in stacking orders and review the relevant advances in twistronics enabled by moiré superlattices with interlayer twist in bilayer or multilayer stackings. In particular, this section will cover the basics of moiré superlattices, the fabrication methods and the emergent research trends including large-scale chemical synthesis, the new spin textures, charge and topological orderings in bilayer twisted structures, correlated phenomena in multilayer moiré superlattices, as well as new surface chemistry that arises from interfacial moiré periodical potentials. In conjunction with sections 2 and 3 on the new physical properties enabled by stacking phase engineering, section 4 focuses on the development of novel and energy efficient devices based on stacking orders, such as memory, quantum emitter, solar cell, and chemical catalytic devices. This section highlights the exciting potential applications for these emergent stacking orders in vdW materials. In section 5, we conclude with a discussion of the current challenges and opportunities facing this field of research. In this section, we present the open issues that need future experimental and theoretical exploration pertaining to stacking phase engineering of 2D layered materials, including repeatable and large-scale stacking material synthesis and processing, precise and high throughput theoretical modeling, broadened material choice for slidetronics and twistronics, ultrafast dynamics and domain kinetics in stacking engineered materials and devices as well as new chemical functionality enabled by stacking.

2. STACKING ORDER ENGINEERING ENABLED BY INTERLAYER SLIDING

The layered nature of 2D vdW materials enables the possibility of different stacking orders composed of different intralayer crystal phases and/or vertical stacking sequences. Interlayer sliding, referring to the lateral displacement of one layer relative to another, enables control of or creating stacking orders, which can have a profound influence on the properties and quantum orders of the material/heterostructure. Control of interlayer sliding to change the stacking order is an exciting path to efficient low-energy electronics, as the energy barrier needed to overcome the weak interlayer vdW forces is often ∼1−10 meV/u.c.,[34,35] one to two orders smaller than conventional covalent or ionic bonds.[25,36] In this section, we will begin by reviewing the stacking order of layered 2D materials and the methods available to directly probe the crystal structures. We then provide a broad review of sliding ferroelectricity and electrical control of the sliding order, including experimental demonstrations and theoretical understandings. We discuss additional engineering approaches to achieve dynamical control of the stacking order, primarily through interlayer sliding, and remark on the coupling of other quantum orders to the sliding order, including sliding magnetism and superconductivity, which offer an exciting avenue to realize practical multiferroics.

Layered vdW materials may be synthesized in various stable crystalline phases, differing in intralayer atomic positions and/or the interlayer stacking sequence, leading to a vast array of accessible stacking orders. For example, there are several phases of transition metal dichalcogenide TMD monolayers, including the 1H hexagonal phase that can be stacked in parallel or antiparallel layers to form the 2H and 3R stacking orders, respectively.[37−40] Different crystalline phases and stacking orders may be obtained by bottom-up synthesis of individual atomic layers or by top-down exfoliation of bulk crystals. Bottom-up synthesis of atomically thin layers is often achieved by chemical vapor deposition (CVD),[37−39] as well as atomic layer deposition (ALD),[39,40] molecular beam epitaxy (MBE),[41] and physical vapor deposition (PVD).[42] Top-down techniques involve exfoliation of thin layers from bulk crystals. The most widely used is mechanical cleavage of pristine thin layers (the Scotch tape method), although the yield may be low and the size of exfoliated flakes may be on the micron scale. Chemical exfoliation via intercalants introduced to assist cleaving between layers, and physical exfoliation such as by sonication in liquid to produce shear forces that separate layers, are other common top-down exfoliation techniques.[43] For top-down methods, crystals are often synthesized by chemical vapor transport (CVT),[44] as well as the self-flux method,[45] which has been shown to enable defect densities up to two orders lower than CVT.[46] A variety of top-down and

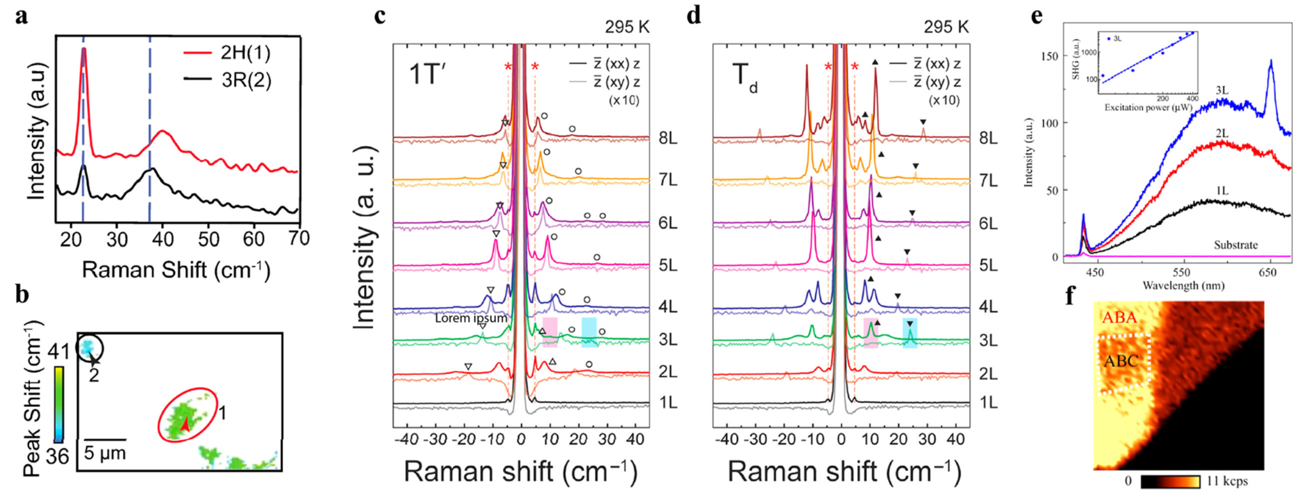

Figure 2. All-optical characterization methods that directly probe the stacking/sliding order. (a) Low-frequency Raman spectra of 2H and 3R stacking regions of bilayer MoS_2, showing the red shift of the interlayer breathing mode from the 2H to 3R stacking order. (b) Spatial mapping of the breathing mode peak shift, indicating 2H(1) and 3R(2) stacking domains. (a, b) Reproduced with permission from ref 57. Copyright 2020 Springer Nature.(c, d) Low-frequency polarized Raman spectra of the 1T′ (c) and T_d (d) phases of room temperature $MoTe_2$. Open circles and triangles in (c) indicate interlayer breathing and shear modes, respectively. Solid black triangles in (d) indicate extra interlayer shear modes that appear in the T_d phase. (c, d) Reprinted with permission from ref 60. Copyright 2021 American Chemical Society. (e) Up-converted optical spectrum for monolayer to trilayer graphene for 1300 nm excitation. SHG appears in the trilayer from noncentrosymmetric ABA stacking. (f) ABA and ABC stacking domains of trilayer region distinguished in SHG intensity mapping. (e, f) Reproduced with permission from ref 74. Copyright 2018 AAAS.

bottom-up synthesis methods enables access to exciting stacking orders. For instance, the noncentrosymmetric R-stacking order of MoS_2 and $MoTe_2$ was directly synthesized by CVT and CVD, respectively, for studies of their intriguing nonlinear properties.[37,47] Recently, a ferroelectric stacking order of SnSe was directly synthesized by PVD, in contrast to the conventional antiferroelectric stacking, yielding a strong nonlinear optical response from in-plane dipoles that add coherently upon stacking.[48] Beyond direct synthesis, arbitrary stacking orders may be engineered through assembly of heterostructures from atomically thin layers with polymer-assisted dry transfer approaches. The "tear and stack" technique,[49−51] widely used in studies of moiré physics (see section 3), enables precise control of the twist angle between artificially stacked layers. Controlling the twist angle between layers allows for on-demand generation of desired stacking orders. For example, 1H phase TMD monolayers can be artificially stacked in the R-stacking sequence by means of the tear and stack method.[20] The ability to fabricate desired stacking orders on demand enables a large bank of accessible stacking orders. We thus require direct sensitive probes to identify and characterize stacking orders and stacking order transitions, which will be reviewed in the following subsection.

2.1. Characterization Methods to Probe Stacking Orders with Distinct Interlayer Sliding

The vast array of crystalline phases and stacking sequences of layered materials provides an exciting opportunity to study their resulting physical properties and the possibility to tune properties through driven stacking order transitions. Achieving dynamical control of sliding orders first requires direct probes of key structural properties to identify and characterize the stacking/sliding order. In this section, we will review and compare characterization methods for stacking orders to reveal intra- and interlayer vibrational modes (phonons), lattice symmetry, underlying atomic structure, and other optoelectronic properties sensitive to the stacking order.

2.1.1. Raman Spectroscopy. Raman and infrared (IR) spectroscopy are noninvasive tools to directly probe the vibrational modes of 2D materials, sensitive to both intralayer vibrational modes from lattice distortion and interlayer vibrational modes where entire layers move uniformly.[52] A Raman-active mode must induce a change in the polarizability, whereas an IR-active mode must change the net dipole moment. In a conventional Raman setup, a focused incident laser excites vibrational modes of the sample (phonons), which returns red-shifted (Stokes) or blue-shifted (anti-Stokes) photons, where energy has been exchanged with vibrational modes. Low-frequency Raman spectroscopy emerged as an important probe of the shear mode (the adjacent layers slide relative to each other) and breathing mode (all layers move together in a direction perpendicular to the plane of layers) of layered materials, which are typically of much lower frequency than intralayer modes.[52−54] They are useful for understanding the interlayer coupling and can also indicate the number of layers present in a 2D material. To access the low-frequency Raman modes ($\lesssim 100\ cm^{-1}$), a narrow line width laser, along with bandpass and notch filters, are typically necessary to narrow the excitation spectrum and suppress Rayleigh scattered light.[52,53,55] Low-frequency Raman spectroscopy can be used as a clear indicator of the stacking sequence. For instance, in few-layer graphene the ABA and ABC stacking configurations can be distinguished by the low shear branch (C′) appearing in ABC stacking and the high shear branch (C) appearing in ABA stacking.[54,56] Identification of the stacking order through low frequency Raman spectroscopy has also been demonstrated in MoS_2, where the interlayer breathing mode of the 3R stacking order is red-shifted from that in the 2H stacking order (Figure 2a).[57,58] Sam et al.[57] employed this characteristic difference to spatially map 2H and 3R stacking order domains, as shown in Figure 2b. Polarized Raman spectroscopy, where the polarization components of the scattered light parallel and perpendicular to the incident light

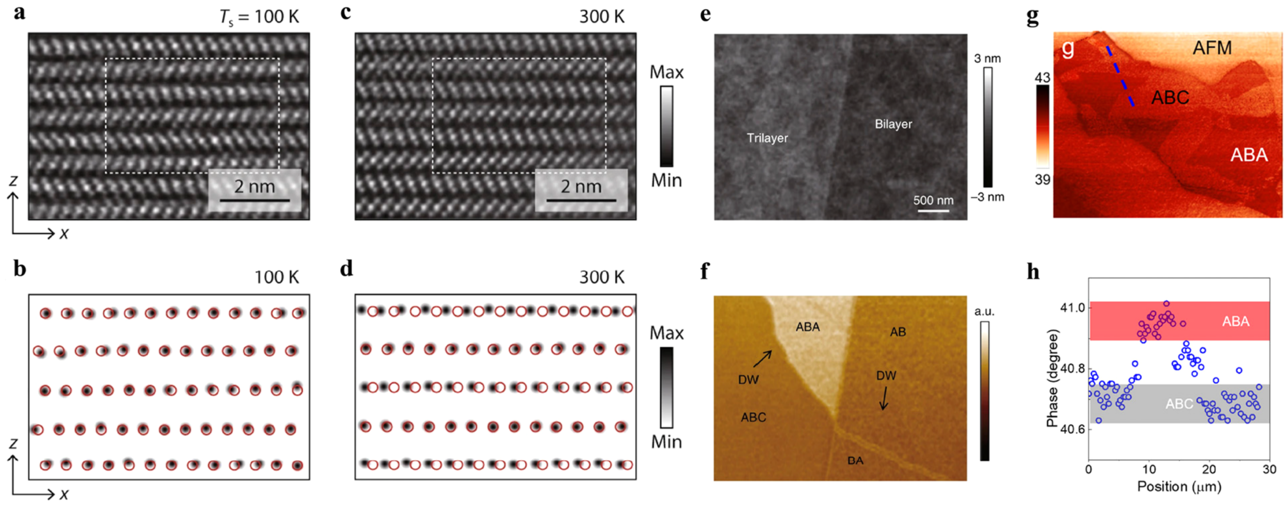

Figure 3. Characterization methods that directly probe the stacking/sliding order with atomic resolution. (a, c) HAADF-STEM images of PbI_2 below (a) and above (c) the order−disorder transition temperature. (b, d) Corresponding fits to the locations of Pb atoms below (b) and above (d) the transition temperature, compared to red circles indicating their expected position in the 4H-PbI_2 phase, showing the interlayer sliding. Reproduced with permission from ref 77. Copyright 2023 Springer Nature. (e, f) AFM topography (e) and near-field infrared nanoscopy (f) of bilayer and trilayer graphene, where different stacking domains show no height difference, whereas ABC and ABA domains have clear NIR contrast and domain walls are identified. Reproduced with permission from ref 86. Copyright 2018 Springer Nature. (g) AFM phase response imaging of trilayer graphene and corresponding line profile of blue dashed line (h), showing a clear change in the phase shift across domains. Reprinted with permission from ref 92. Copyright 2021 American Chemical Society.

are detected separately, can help reveal more distinctions in the spectra between stacking orders. For instance, polarized low-frequency Raman was used to distinguish the T_d and 1T′ stacking orders of $MoTe_2$, where extra interlayer shear modes appear in the T_d phase, which helped identify the existence of both T_d and 1T′ stacking orders in thin exfoliated $MoTe_2$.[59] Figure 2c,d show the 1T′ and T_d spectra, respectively, where open triangles (circles) indicate interlayer shear (breathing) modes and the solid triangles highlight the extra modes in the T_d phase.[60] Beyond the stacking order, the evolution of shear modes with layer thickness has been shown to be an indicator of layer number in TMDs,[60−63] which can also be seen in the different $MoTe_2$ thicknesses in Figure 2c,d. Furthermore, twisted moiré superlattices can host folded acoustic phonon modes, deemed "moiré phonons", that can be resolved by low frequency Raman spectroscopy.[64−66] Comparing the calculated dispersions with observed moiré phonons enables precise determination of the twist angle, as well as identification of regions of atomic reconstruction where low frequency shear modes dominate and moiré modes are absent. Although low-frequency Raman has emerged as a valuable means of probing the stacking order, it should be noted that intralayer modes at higher frequencies may also indicate the stacking order. For instance, the stacking order dependence of G and G′ (2D) modes of graphene have been used to distinguish ABA and ABC stacking orders.[67,68] Furthermore, the AA′ and AB stacking orders of MoS_2 could be distinguished by their differing Raman and photoluminescence spectra,[69,70] and the T_d phase of $MoTe_2$ shows splitting of peaks from intralayer modes, compared to the 1T′ phase.[60]

2.1.2. Second Harmonic Generation Spectroscopy.

Second harmonic generation (SHG) spectroscopy is an additional optical tool that is a nondestructive probe of lattice symmetry. When sufficiently high-power pulsed laser light is incident on a crystal lacking inversion symmetry, the oscillating electric field drives anharmonic oscillations of the electric dipoles, which can radiate harmonics of the incident light frequency.[71] The strength of the SHG signal is determined by the second order nonlinear susceptibility ($\chi^{(2)}$), which can be nonzero only for noncentrosymmetric materials, where the breaking of inversion symmetry enables a net nonzero contribution from the dipoles in the lattice.[71,72] This method has been widely used to identify crystal symmetry in a vdW intralayer and their phase transitions. For instance, gate-dependent SHG measurements revealed a structural transition in monolayer $MoTe_2$ driven by electrostatic doping, evidenced by the intensity drop at the transition to a centrosymmetric crystal structure.[23] Additionally, separating the polarization components of the SHG signal can help reveal the crystallographic orientation.[23,73] More importantly, different stacking sequences lead to different lattice symmetries; hence, SHG can be a noninvasive sensitive probe. For instance, in graphene, the trilayer shows a clear SHG signal, due to noncentrosymmetric ABA stacking, compared to the centrosymmetric monolayer and bilayer,[74] which are compared in Figure 2e. The ABC stacking sequence maintains inversion symmetry, enabling mapping of ABA and ABC stacking domains. As seen in the trilayer region on the left of the flake mapped in Figure 2f, the transition from ABA to ABC domains results in a drop in SHG intensity, as centrosymmetry is restored. A similar drop is seen at the transition to the centrosymmetric bilayer region on the right side of the flake.[74] Layer dependence of the lattice symmetry was explored with SHG in 2H-stacked MoS_2 and BN as well, where noncentrosymmetric odd layers show a large SHG signal, whereas inversion symmetric even layers show no significant SHG signal.[73] As SHG is an important tool to characterize the stacking order of layered materials, it can help elucidate stacking transitions driven by interlayer sliding, particularly accompanying inversion symmetry changes and therefore the observable SHG. For example, gate-dependent SHG measurements revealed an electrically driven sliding transition in few-layer WTe_2 from the T_d phase, where the inversion asymmetric P_m space group yields a large SHG intensity, to the 1T′ phase, where the centrosymmetric $P2_1/m$

space group disallows SHG.[19] Raman measurements showed the preservation of high-frequency intralayer modes and a large intensity reduction of the *b*-axis interlayer shear mode through the transition, confirming interlayer sliding as the mechanism of the T_d to 1T′ transition. SHG is also sensitive to magnetic order, which can break inversion and time reversal symmetry.[75,76] Optical measurements, including Raman spectroscopy and SHG, often employed together, have emerged as critical nondestructive sensitive tools to directly probe the stacking and sliding orders.

2.1.3. Transmission Electron Microscopy. Purely optical measurements, limited in spatial resolution by the diffraction limit, often provide macroscopic information, such as vibrational modes from Raman and overall lattice symmetry from SHG. It is also vital to probe the underlying atomic structure of layered materials to identify and distinguish between stacking orders on the atomic scale. Transmission electron microscopy (TEM) provides a means of directly imaging the atomic structure of 2D materials with atomic scale spatial resolution. For example, cross-sectional STEM was employed to reveal interlayer sliding as the mechanism of an order−disorder phase transition in lead iodides (PbI_2).[77] Figure 3a,c show high-angle annular dark-field scanning TEM (HAADF-STEM) images above versus below the transition temperature, and Figure 3b,d show corresponding fits to the locations of Pb atoms compared to red circles that denote their expected position in the 4H-PbI_2 phase, clearly showing the change in the stacking order from interlayer sliding, whereas the intralayer atomic structure remains the same.[77] The stacking order may also be visualized with TEM in plan view, normal to the surface, by directly viewing the vertical alignment of atoms between layers, for instance, to identify the stacking sequence in TMD.[70,78,79] Atomic imaging provides a direct visualization of the stacking order and is a vital element of 2D material characterization. Recently, Hart et al.[80] employed cross-sectional HAADF-STEM to directly image the debated stacking order of thin $MoTe_2$ flakes. They found the stacking to be highly disordered, including emergent stacking configurations alongside nanoscale domains of T_d and 1T′ stacking, compared to the nicely ordered T_d stacking of WTe_2. These findings reveal the rich stacking phases of thin $MoTe_2$, of great importance to investigations of the quantum orderings in thin $MoTe_2$, and emphasize the importance of atomic imaging to fully characterize the structural properties of emerging 2D materials. Electron diffraction can serve as another probe of the atomic structure, where the stacking order can modulate the intensity of diffraction peaks.[78−83] Additional examples of using cross-sectional TEM to visualize the stacking order include the study of yttrium doped γ-InSe,[84] where they used TEM to directly image the interlayer compression and layer-by-layer presliding, the real-time observation of shear-stress-induced interlayer sliding in MoS_2 nanoflakes,[85] and direct imaging of (anti)-ferroelectric stacking domains in PVD synthesized SnSe.[48] Electron microscopy techniques, particularly STEM, which has been extensively employed to image stacking orders, offer atomic scale resolution; however, the substrate and instrumentation requirements can pose a challenge, inviting the need for noninvasive atomic scale probes for quick characterization of the stacking order with minimal substrate and instrument requirements.

2.1.4. Atomic Force Microscopy Techniques. Techniques based on atomic force microscopy (AFM) can provide a noninvasive probe of the stacking order with nanoscale resolution, beyond the reach of purely optical measurements (e.g., Raman and SHG). Such techniques rely on obtaining a measurement contrast between stacking orders, enabling the identification of different stacking order and domain walls on the nanoscale. Near-field infrared nanoscopy offers a non-invasive probe with nanoscale resolution and has been extensively employed to map stacking order domains and identify domain walls in few-layer graphene.[16,86−90] Based on an AFM operating in tapping mode, infrared light is focused on a conductive tip and the back scattered light is detected in the far-field. The scattering amplitude is sensitive to the optoelectronic properties of the sample, and thus stacking domains with different optoelectronic properties may be distinguished.[90] For example, Jeong et al.[90] mapped out AA′ and AB domains in bilayer graphene based on the scattering amplitude contrast that arises from the differing intraband and interband optical conductivities of the stacking orders, and Jiang et al.[92] mapped ABA and ABC domains in trilayer graphene whose differing electronic band structures led to the contrast in the near-field images. The topography data, shown in Figure 3e, does not identify stacking domains, whereas the near-field nanoscopy image, shown in Figure 3f, clearly distinguishes stacking order domains and domain walls. More recently, Shen et al.[89] demonstrated a means of improving the IR contrast with excitation near graphene's 1585 cm^{-1} phonon frequency and applying a vertical electric field that activates the otherwise IR-inactive mode. This enhanced contrast enabled unambiguous determination between ABA and ABC domains. Scattering-type scanning near-field optical microscopy has proven to be a reliable noninvasive probe of the stacking order in few-layer graphene, offering spatial resolution much finer than Raman or SHG probes. This technique has also been applied to reveal surface plasmon polaritons in few-layer graphene dependent on the stacking order (ABA vs ABC).[88]

Although near-field infrared nanoscopy can probe the stacking order, it requires a more complex experiment platform than conventional AFM, making it advantageous to find contrast being stacking orders in a conventional AFM setup. Wu et al.[91] demonstrated the ability to distinguish ABA and ABC stacking domains in few-layer graphene by tracking the phase shift response in an AFM scan. The phase shift shows clear contrast between ABA and ABC domains, originating from their different energy dissipation in the interaction between the tip and the sample, and domain walls are easily identifiable, whereas the tomography data shows no height difference. Figure 3g shows a representative AFM phase image of trilayer graphene, showing the distinct domains, and Figure 3h shows the line profile for the dashed blue line in Figure 3g, highlighting the phase contrast between domains. Furthermore, domain walls could be manipulated by using the tapping of the tip to impart stress waves on domain walls, forcing them toward the edge where the stored strain can be released.

2.2. Sliding Ferroelectricity That Arises from Polar Stacking Orders

The discovery of ferroelectricity produced by particular polar stacking orders, either by natural growth or artificial stacking, has inspired much recent interest in "sliding ferroelectricity". Unlike a conventional ferroelectric material, such as lead zirconium titanate (PZT) whose spontaneous polarization forms inside the unit cell[93] or within the intralayer of In_2Se_3,[25,94,95] sliding ferroelectricity in 2D materials is caused

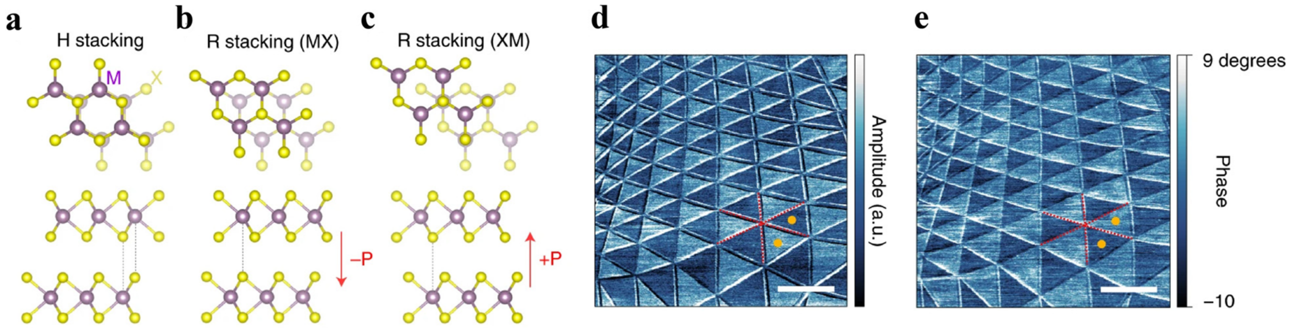

Figure 4. Polar stacking and PFM mapping of ferroelectric domains. (a−c) Nonpolar H-stacking (a) and polar R-stacking (b, c) of TMDs. (d, e) PFM amplitude (d) and phase (e) mapping of ferroelectric domains in twisted bilayer $MoSe_2$. Reproduced with permission from ref 20. Copyright 2022 Springer Nature.

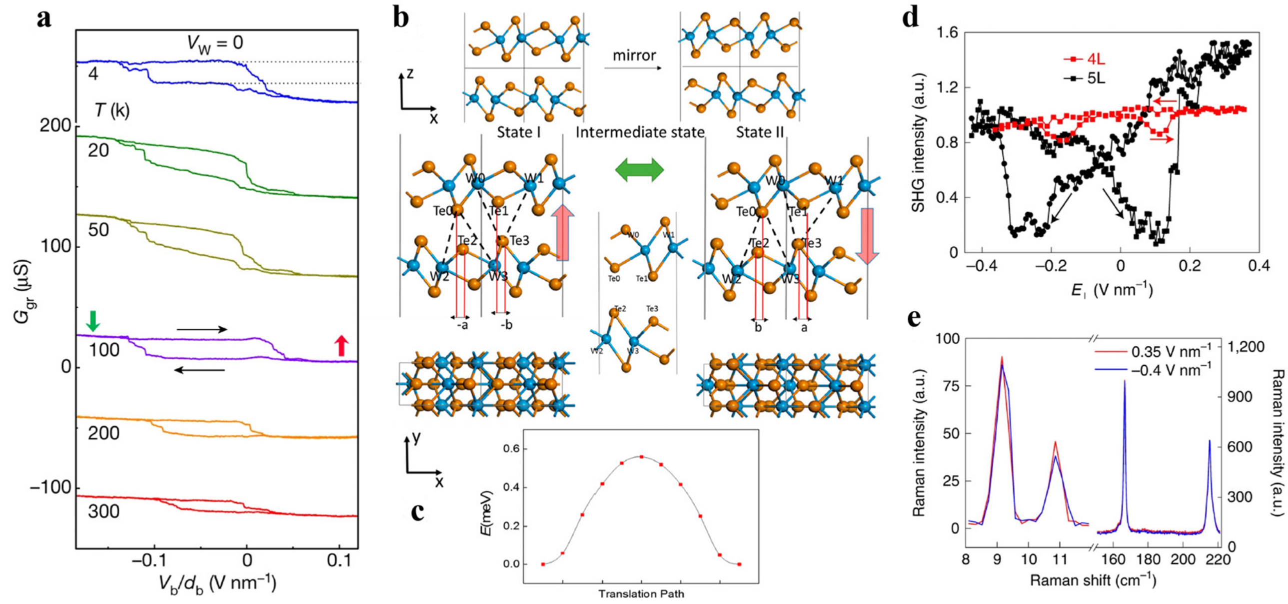

Figure 5. Early demonstrations of sliding ferroelectricity. (a) Ferroelectric switching of T_d-WTe_2 polarization by varying the out-of-plane electric field, shown by measured conductance of overlaid graphene. Reproduced with permission from ref 18. Copyright 2018 Springer Nature. (b, c) Proposed sliding ferroelectricity model via interlayer charge transfer induced by inequivalence between the layers (b) and computed ferroelectric switching pathway (c) to explain observations in (a). Reprinted with permission from ref 34. Copyright 2018 American Chemical Society. (d, e) Electrically driven sliding transition between polarization states of T_d-WTe_2, identified by butterfly shaped hysteresis in SHG intensity (d) and preservation of both low and high frequency Raman modes (e). Reproduced with permission from ref 113. Copyright 2020 Springer Nature.

by the interlayer polarization. The stacking order must break M_z mirror symmetry and inversion symmetry to allow for a net polarity, switchable by an interlayer translation. The weak interlayer vdW forces enable a low switching barrier, making sliding ferroelectrics an exciting platform to realize multiferroics and create practical devices for low energy electronics, such as nonvolatile random-access memory.[36,96] Here we discuss the nature of sliding ferroelectricity, theoretical understandings and experimental demonstrations.

2.2.1. Sliding Ferroelectricity in Natural and Artificial Stacking Orders.

Sliding ferroelectricity can exist naturally in noncentrosymmetric stacking configurations, such as T_d-WTe_2[18,19] and rhombohedral stacked (R-stacked) TMDs.[97] Moreover, artificial stacking provides the opportunity to create ferroelectricity on-demand by constructing a noncentrosymmetric stacking configuration.[36,98] For example, when artificially stacking 1H phase TMD monolayers in an R-stacking sequences, it creates a noncentrosymmetric stacking order that can exhibit ferroelectricity[20] and slightly twisted R-stacked bilayers to generate a moiré superlattice of ferroelectric domains. Figure 4a−c schematically shows the nonpolar H-stacking (a) and polar R-stacking (b,c) orders of TMDs, where the R-stacking breaks centrosymmetry.[20] In either case (natural or artificial stacking), ferroelectricity can be verified through piezo force microscopy (PFM), where ferroelectric domains can be spatially mapped with nanoscale resolution. An oscillating electric field is applied at the scanning tip, and the resulting mechanical response from deformation of the sample, due to piezoelectric or flexoelectric effects, is measured.[20,30,99] For example, Figure 4d,e shows vertical PFM mapping of ferroelectric domains in twisted bilayer $MoSe_2$.[20] Furthermore, the phase of the piezoresponse can reveal the directionality of the polarization and piezoelectric/flexoelectric coefficients can be determined.[100−102] For instance, the drastic contrast in the piezoelectric coefficients between even and odd layers of MoS_2 shows the need for noncentrosymmetry to host ferroelectric properties.[102] Lateral PFM may also be used to map in-plane ferroelectric domains, such as in the recently synthesized

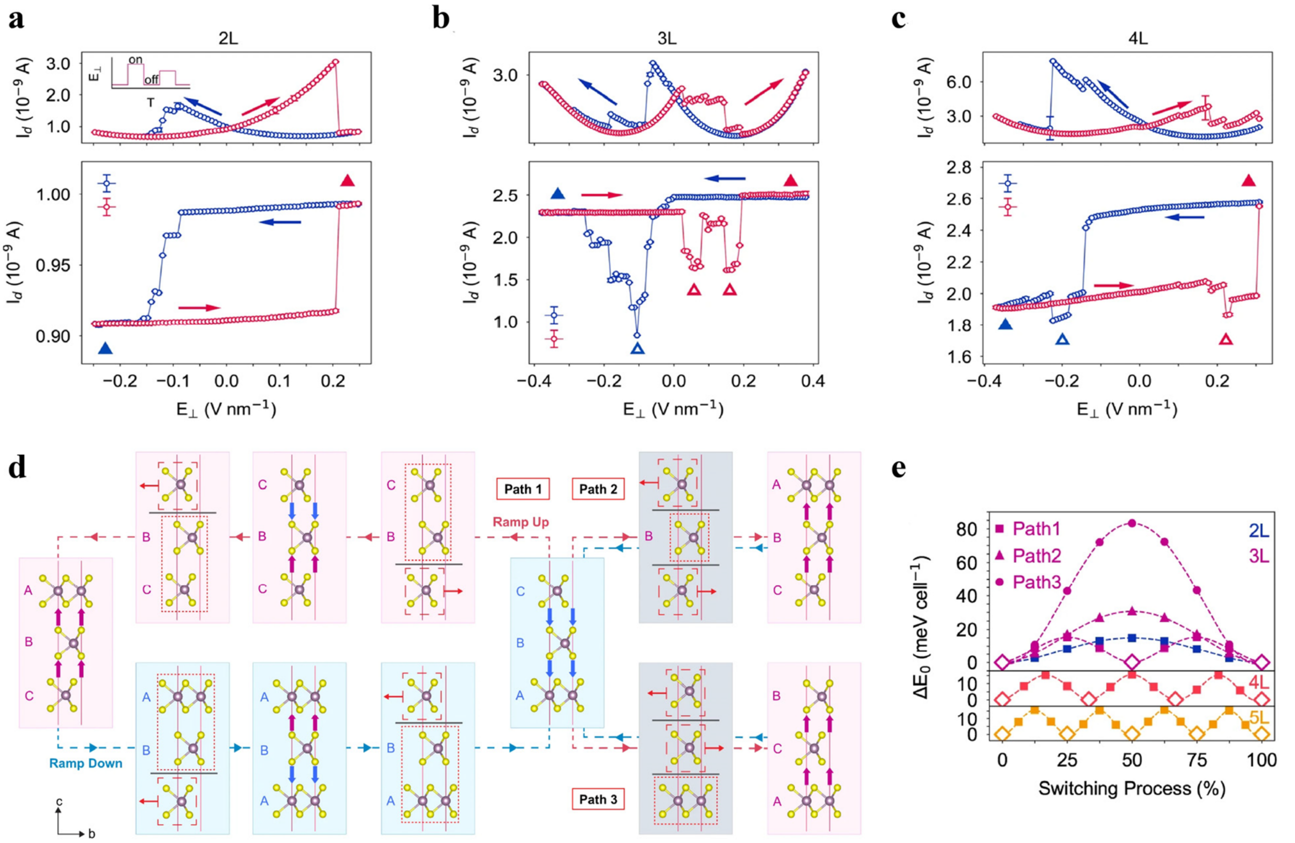

Figure 6. Multilayer sliding ferroelectricity. (a−c) Multiple stable polarization states induced by multilayer sliding ferroelectricity in bilayer (a), trilayer (b), and four-layer (c) MoS_2, where layers are understood to slide one at a time. Hollow triangles highlight the anomalous intermediate polarization states. (d) Schematic of the three possible sliding pathways during vertical electric field ramping in the trilayer. Dashed and dotted boxes indicate stationary and moving regions, respectively. Solid vertical arrows denote spontaneous polarization. Solid horizontal arrows denote sliding direction of unstable configurations, and gray lines indicate the sliding interfaces. (e) Total energy profiles for different sliding pathways in different layer devices, showing the energetic favorability of path 1 and existence of stable intermediate states. Reproduced with permission from ref 97. Copyright 2022 Springer Nature.

ferroelectric stacking order of SnSe,[48] as well as to probe the response of domain walls.[20,103] The surface electric potential can also be mapped with an atomic force microscope (AFM) operated in Kelvin probe mode (KPFM), which measures the difference in work functions between the surface and tip,[103] also enabling the spatial mapping of ferroelectric domains.[104]

2.2.2. Theoretical Understanding. The natural existence of sliding ferroelectricity in noncentrosymmetric stacking orders and ability to create artificial stacking orders on-demand yields a vast array of potential 2D ferroelectrics. 2D ferroelectricity was first observed in WTe_2.[18] As depicted in Figure 5a, the vertical polarization, probed by conductance measurements using graphene as an electric field sensor, shows clear ferroelectric switching and hysteretic behavior as the vertical electric field is swept.[18] The hysteresis path and width could be modified by carrier doping. In response to this discovery, through DFT calculations and computing ferroelectric switching pathways, the polarization switching has been attributed to uncompensated charge transfer between Te atoms,[34] arising from the centrosymmetry breaking that yields an inequivalence between the layers. Figure 5b,c shows the inequivalence between Te atoms in different layers (b), and computed ferroelectric switching pathway (c).[34] Many studies have now applied first-principles calculations with density functional theory (DFT), and calculated ferroelectric switching pathways with the nudged-elastic-band (NEB)[105] method, to understand and/or predict the nature of the spontaneous and switchable polarization in several 2D materials with appropriate stacking.[34,35,97,106−112] The generation of out-of-plane electric dipoles is generally attributed to charge redistribution in noncentrosymmetric van der Waals materials, through interlayer charge transfer[34,35] or orbital distortion,[107,111] that results in a net polarization. Although a powerful means of theoretically exploring and predicting the switching barrier for sliding ferroelectrics, the inherently small switching barrier, often on the order of 1−10 meV/u.c.,[34,35] is quite small compared to the typical accuracy of DFT calculations (~1 kcal/mol) employed by ab initio NEB calculations. Experimental studies are therefore imperative to directly probe the sliding process and switching barrier. As will be seen in the following section, experimental studies of sliding ferroelectricity are often combined with theoretical modeling to obtain a complete understanding of the sliding process and the switching barriers.

2.2.3. Experimental Realizations. Since the onset of sliding ferroelectricity, experimental demonstrations have been greatly expanded. After the first identification of sliding ferroelectricity in few-layer WTe_2,[113] researchers employed electrostatic hole doping to trigger the 1T′ to T_d stacking transition, through interlayer sliding. The same interlayer sliding mechanism was found to enable sliding ferroelectricity between the up and down polarization states of the T_d phase,

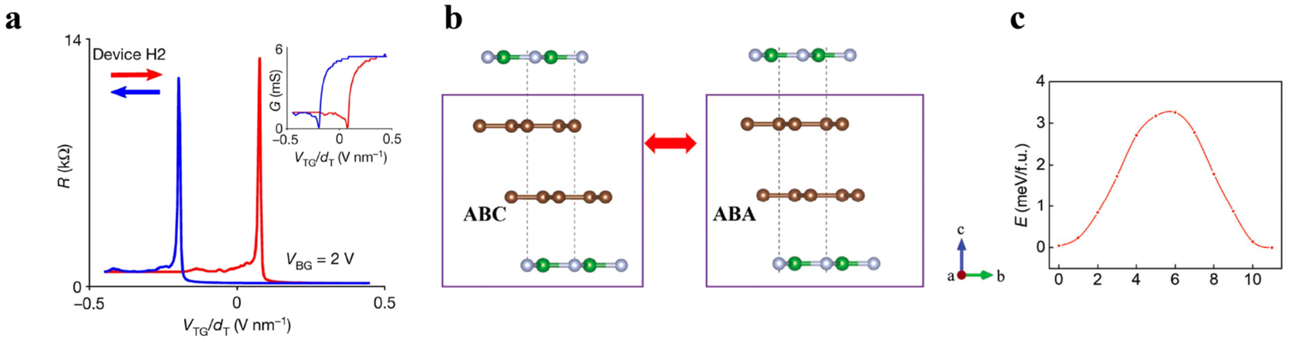

Figure 7. Across-layer sliding ferroelectricity. (a) Unconventional ferroelectric switching observed in graphene bilayer intercalated BN twisted heterostructure. Reproduced with permission from ref 118. Copyright 2020 Springer Nature. (b, c) Proposed across-layer sliding model (b) and computed switching pathway (c) to explain unconventional ferroelectricity in the device shown in (a). Reproduced with permission from ref 120. Copyright 2023 Wiley-VCH GmbH.

related by an interlayer translation. Vertical electric field dependent SHG measurements reveal the hysteretic behavior indicative of the transition between polarization states, shown in Figure 5d. The ferroelectric switching is observed in both even and odd layer numbers, but the SHG modulation depth is much higher in odd layers because their 1T′ phase, a possible intermediate state in the sliding, is centrosymmetric, disallowing SHG. The up and down polarization states of the T_d phase show identical Raman spectra, maintaining low and high frequency modes, which are shown in Figure 5e, and identical SHG polarization patterns, further indicating the switching is merely from interlayer sliding to a degenerate crystalline structure simply with opposite polarization. Electrical control of ferroelectric domains in WTe_2 was also demonstrated through PFM scanning before and after applying switching bias pulses.[100]

In addition to WTe_2, sliding ferroelectricity has been observed in BN bilayers, both in parallel stacking and with an interlayer twist that generates a moiré superlattice of polarization domains.[104,114,115] The polarization could be switched electrically via dual-gate devices or scanning a biased tip in KPFM measurements.[104,115] Sliding ferroelectricity has also been demonstrated in rhombohedral-stacked TMDs, including MoS_2, WS_2, $MoSe_2$, and WSe_2,[20] where the noncentrosymmetric stacking order was produced by stacking monolayers in parallel with the tear-and-stack method and the polarization state could be switched with an electric field. Control of the stacking order through interlayer sliding driven by carrier doping and electric field has also been demonstrated in few-layer graphene.[116]

Sliding ferroelectricity in other multilayer structures, and even across layers, has attracted recent attention due to the possibility of generating multiple stable stacking orders. Multilayer MoS_2 in dual-gate field-effect transistors shows multiple stable polarization states in trilayer and four-layer devices,[97] evidenced by nonmonotonic changes in the drain current, as opposed to monotonic stepwise changes indicative of in-plane domain boundary movement. The multiple polarization states are shown in Figure 6 a−c for different layer numbers, where the hollow triangles denote the anomalous intermediate polarization states.[97] Repeatability across several multilayer devices and the lack of the extra states in the bilayer device ruled out simple in-plane domain boundary movement. Through an exhaustive theoretical analysis of the three possible sliding pathways ((1) single layer sliding, (2) nonadjacent layers sliding in opposite directions, and (3) adjacent layers sliding in opposite directions), they find single layer sliding (path 1), where individual layers slide one at a time, to clearly be energetically favorable and enable stable intermediate polarization states. Figure 6d shows schematically the three sliding pathways for the trilayer during ramping of the vertical electric field, and Figure 6e shows the total energy profiles for the different pathways in different layer devices. The energy profiles for all three pathways are shown for the trilayer, showing the much lower barrier for path 1 and the stable intermediate state residing between energy barriers, suggesting thermodynamic stability and consistent with the observed multiple polarization states in multilayer devices.

Layer by layer sliding offers an exciting platform to access several stable states of a device. Additionally, control of domain walls and access to multiple polarization states has been demonstrated in multilayer MoS_2 and WSe_2 through a gate bias that modulates the carrier density and displacement field.[117] Another interesting possibility of sliding ferroelectricity in multilayer structures is across layer sliding when symmetry forbids direct sliding between adjacent layers. For instance, sliding between next-neighbor layers in graphene bilayer intercalated BN was suggested to explain recent observations of unconventional ferroelectricity,[118−120] where symmetry forbids sliding within the graphene bilayer. Figure 7a shows the observed ferroelectric switching in a device with the top and bottom graphene rotated by ~30°,[118] and Figure 7b,c shows the across-layer sliding model (b) and proposed switching pathway (c).[120]

2.3. Engineering Approaches To Control Sliding Orders

In vdW materials, the energy barriers for different types of transitions can vastly affect their controllability and applications. For example, lattice reconstruction within an intralayer during a phase transition often involves overcoming significant energy barriers. This can make it challenging to control these transitions for practical applications. On the other hand, the energy barrier for interlayer sliding transitions, which govern the stacking sequence of the layers, is typically much lower—on the order of approximately 1−10 meV/u.c.[34,35] This low energy requirement potentially allows for easier control over the stacking sequences, offering a viable route for tuning the material's electronic, optical, and mechanical properties.

2.3.1. Ultrafast and Light-Driven Stacking Order Transitions. Leveraging light-driven and ultrafast pumping techniques presents a compelling approach for manipulating

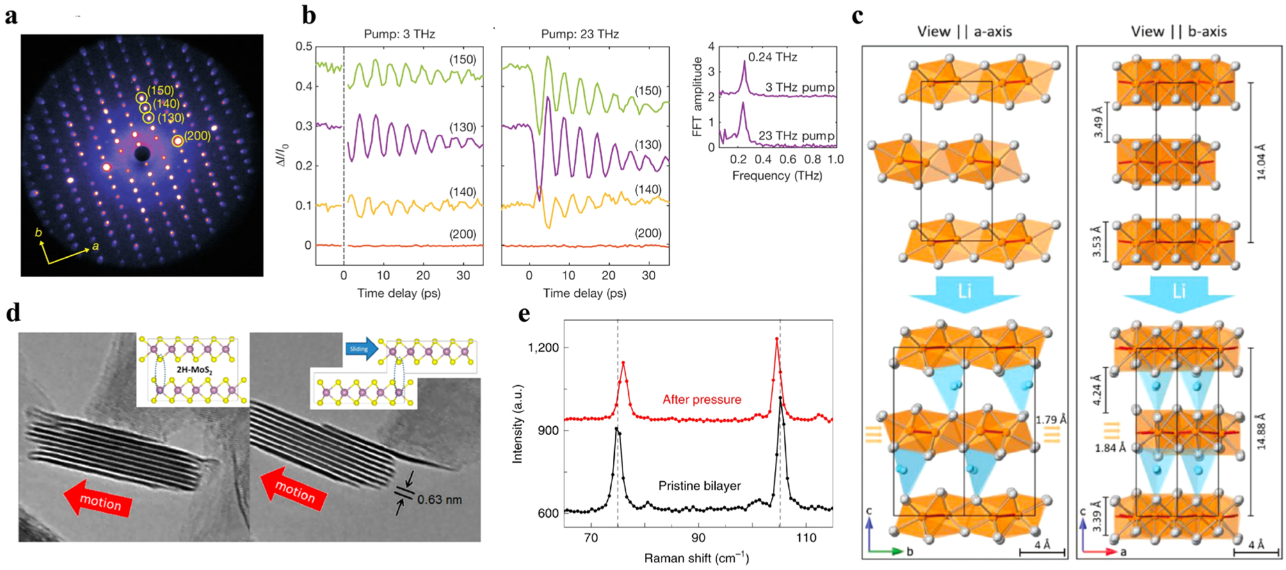

Figure 8. Dynamical control of stacking/sliding order by ultrafast, chemical, and mechanical methods. (a, b) Identified Bragg peaks from relativistic electron diffraction (a) and ultrafast modulation of Bragg peak intensities (b) through driving of the 0.24-THz shear phonon mode of WTe_2, showing the coherent terahertz driven stacking order modulation on ultrafast time scales through interlayer shear sliding. Reproduced with permission from ref 82. Copyright 2019 Springer Nature. (c) Interlayer sliding, lattice stretching and expansion through Li ion intercalation of WTe_2. Reproduced with permission from ref 125. Copyright 2021 Wiley-VCH GmbH. (d) Cross-sectional TEM snapshots of shear-strain-induced interlayer sliding of MoS_2. Reprinted with permission from ref 85. Copyright 2015 American Chemical Society. (e) Raman spectra of CrI_3 before and after application of hydrostatic pressure. The shift in Raman peaks indicates the pressure induced stacking order transition from rhombohedral to monoclinic in. Reproduced with permission from ref 132. Copyright 2019 Springer Nature.

the stacking order in van der Waals (vdW) materials, particularly given this noninvasive method offers critical information about switching speed, mechanism, and thermodynamics. Such control could also benefit diverse applications ranging from tunable electronic and photonic devices to adaptive sensors and spintronic applications. For example, the dynamic control of the sliding order of WTe_2 through ultrafast terahertz femtosecond pulse pump and electron diffraction probe has been demonstrated.[82] They suggest that the terahertz pump induces transient hole doping that weakens the interlaying coupling and triggers a shear phonon that drives the interlayer sliding, observed through the intensity modulation of Bragg peaks from relativistic electron diffraction measurements. The shear phonon drives the stacking order from the T_d phase toward the 1T′ phase and is centered on a new interlayer equilibrium position. Identified Bragg peaks for WTe_2 are shown in Figure 8a, and their ultrafast intensity modulation by terahertz pumping is shown in Figure 8b.[82] Driving of the T_d to 1T′ transition via hole doping directly was later demonstrated.[19] Similar ultrafast modulation of Bragg peaks under optical femtosecond pulse excitation has been demonstrated, where the same shear phonon mode was identified.[83] They concluded that there are two decoupled processes, including the shear phonon mode observed in ref 82 and a structural transition to a metastable state, also through interlayer sliding. The structural transition to the metastable state occurs over ∼5 ps. The decoupling is evidenced by samples of varying thicknesses having similar phase transition time constants (∼5 ps), as well as preservation of the phase transition in defective samples where shear phonons are suppressed. Similar light-driven ultrafast control of the sliding order through triggering of an interlayer shear phonon has been demonstrated in bulk T_d-$MoTe_2$ with near-infrared femtosecond pulses.[121] The structural transition between the T_d and 1T′ phase occurs on a subpicosecond time scale, identified by the intensity of a shear phonon mode and time-resolved SHG. Additionally, DFT calculations show the potential to control the stacking sequence of MoS_2, through interlayer translation, on ultrafast time scales with infrared pulses that coherently excite an interlayer shear mode.[122] Ultrafast pump−probe measurements can also elucidate interlayer charge transfer, which, as evidenced by the theoretical understanding of sliding ferroelectricity, is closely tied to the sliding order. For instance, ultrafast pump−probe measurements enabled clear observation of the dependence of interlayer charge transfer on interlayer sliding and stretching in MoS_2/WS_2 bilayer heterostructures,[82,123] where they selectively excited A-excitons in the bottom MoS_2 layer and probed A-exciton states in the upper WS_2 layer. Ultrafast control of the sliding order offers an exciting avenue to modulate stacking-dependent properties on ultrafast time scales, such as the topological properties of WTe_2.[82]

2.3.2. Chemically Driven Sliding Order Transitions.

In addition to electrical and ultrafast control methods that do not alter the underlying chemical composition, chemical means, such as intercalation, can offer a mechanism of long-lasting control of the stacking order. Intercalation of 2D materials, where atoms, ions or molecules are inserted between the layers of the material, effectively modifying the interactions between those layers and hence affect stacking orders.[124] For example, through X-ray diffraction and complementary DFT calculations, researchers identified a Li intercalation-induced sliding phase transition in WTe_2, from T_d to the lithiated T_d' phase.[125] Figure 8c shows a schematic of the structural changes induced by the Li ion intercalation.[125] Other reports identified the same lithiated T_d'-WTe_2 phase[126] and showed through Bader charge analysis[127] and DFT calculations that charge doping from the Li atoms to the Te atoms destabilizes the lattice and the

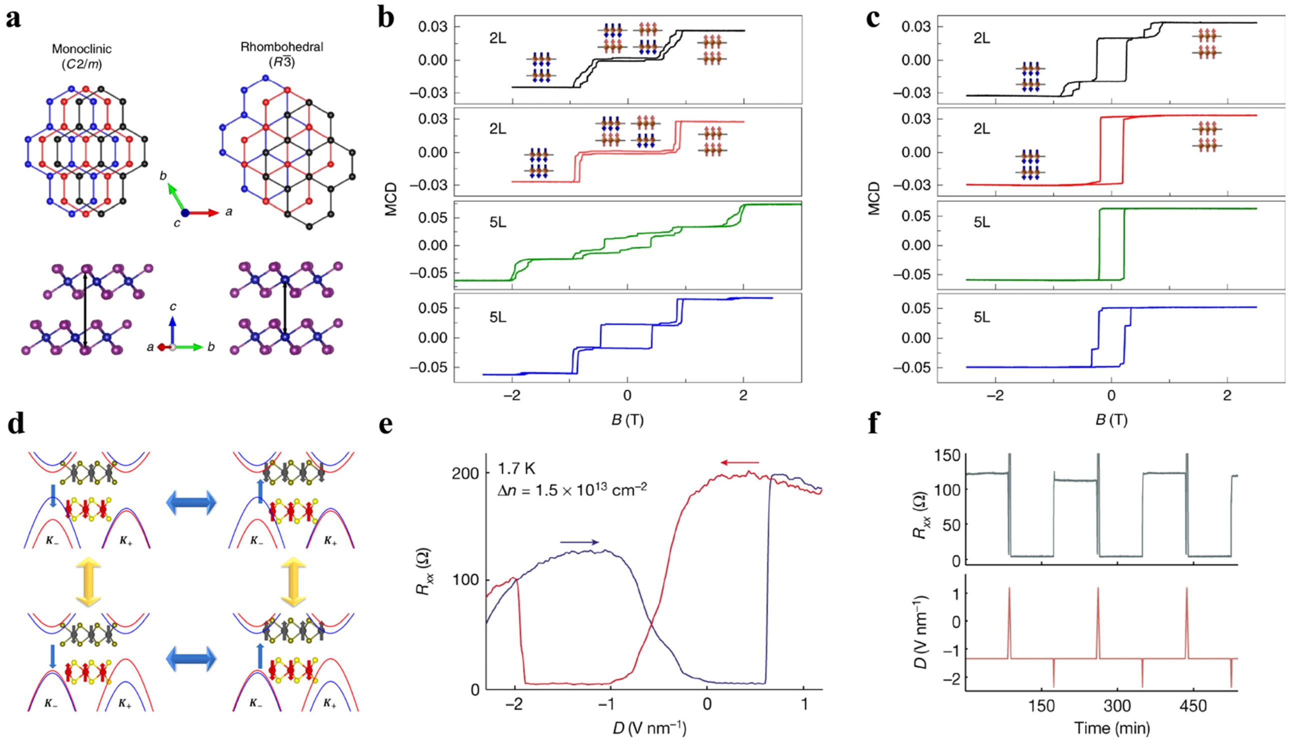

Figure 9. Coupling between the sliding order and other electronic orders. (a) Monoclinic and rhombohedral stacking orders of CrI_3, related by interlayer translation. (b,c) MCD measurements before (b) and after (c) applying hydrostatic pressure, indicating stacking order transition, as the rhombohedral (monoclinic) phase prefers ferromagnetic (antiferromagnetic) interlayer coupling. (a−c) Reproduced with permission from ref 131. Copyright 2019 Springer Nature. (d) Magnetoelectric coupling predicted in VS_2, where ferroelectric switching via interlayer sliding can change the spin configuration of the antiferromagnetic ground state. Reprinted with permission from ref 109. Copyright 2020 the American Physical Society. (e, f) Coupling of the sliding ferroelectricity and superconductivity in T_d-$MoTe_2$, where the superconductive state, indicated by drops in the four-probe resistance (R_{xx}), could be switched on or off by applying a continuous (e) or pulsed (f) electric field. Reproduced with permission from ref 147. Copyright 2023 Springer Nature.

pathway to the lithiated T_d' phase becomes more energetically favorable than to the lithiated T_d phase. The new lithiated T_d' phase features interlayer sliding, changing intralayer bond lengths, and lattice expansion, compared to the T_d phase. The anisotropic and large in-plane strain of the lithiated T_d' phase, tunable through the degree of (relatively low) Li intercalation, enables planar electrochemical actuation.[125]

2.3.3. Mechanically Driven Sliding Order Transition.

vdW materials are well-known for their exceptional mechanical strength yet are very flexible. Therefore, mechanical means can be another efficient approach to achieve dynamical control of the stacking orders. For instance, in a cross-sectional TEM study of interlayer sliding in MoS_2, MoS_2 flakes were electrostatically coupled to an oxidized tungsten probe, enabling their nanoscale manipulation and shear-stress-induced sliding.[85] An example is shown in Figure 8d, where the probe pulls the MoS_2 flake to the left and the top layer is held in place and slid off by the induced shear-strain. The zero normal load shear strength of MoS_2 could be determined by measuring the applied shear force with a nanoindenter force sensor. Mechanically driven translation and rotation between flakes can also be achieved by AFM tip manipulation, such as in MoS_2/graphite, MoS_2/h-BN and graphene/h-BN heterostructures where epitaxial domains were slid on the substrate by an AFM tip.[128−130] This technique probes the lateral force necessary for sliding, enabling identification of superlibridity in large-lattice-mismatch heterostructures.[128] Similarly, AFM tip manipulation has been employed to manipulate stacking domain walls in few-layer graphene, both in contact mode with a blunted tip,[86] and in tapping mode by imparting stress waves through tapping of tip that force domain walls to move toward the edge.[91] In addition to shear-stress-induced sliding and stacking domain manipulation with local probes, hydrostatic pressure-driven control of the stacking order has been demonstrated in CrI_3, where the stacking transition from rhombohedral to monoclinic, related through an interlayer translation, could be identified through Raman indicators and the corresponding magnetic ground state.[131,132] Figure 8e shows the shift of Raman peaks indicative of the stacking order transition, due to hydrostatic pressure that enhances the energetic favorability of the monoclinic phase.[132] The ability to dynamically control the stacking order, often through interlayer sliding, is a critical step to accessing the different stable states and physical properties of different stacking orders, enabling the tuning of properties and realization of practical devices. Electrical control mechanisms, ultrafast and light driven techniques, chemical platforms, and even direct mechanical control, offer demonstrated and exciting means of achieving dynamical control of the stacking orders and their associated properties.

2.4. Sliding Orders Coupled with Other Quantum Properties

The ability to manipulate stacking orders through interlayer sliding, as discussed in the previous section, opens new avenues for tuning other critical properties of 2D materials that are closely linked to stacking configurations. Specifically, for quantum phenomena like magnetism and superconductivity, which are highly dependent on interlayer coupling, stacking order transitions are anticipated to exert a substantial influence. This potent coupling between stacking orders and other material properties presents a promising pathway for the development of practical multiferroic materials.

2.4.1. Sliding Orders Coupled with Magnetism. An important avenue is control of magnetic ordering through the stacking order, such as for nonvolatile electric field control or mechanical/strain control of magnetism. For instance, reports[131,132] demonstrated mechanical control of the magnetic ground state of thin CrI_3 by means of hydrostatic pressure that induces a monoclinic-to-rhombohedral stacking-order transition, where the two are related by an interlayer translation. Figure 9a shows the two stacking orders and their relation via interlayer translation. The monoclinic phase prefers antiferromagnetic interlayer coupling, whereas the rhombohedral phase prefers ferromagnetic coupling, clearly seen by the change in hysteresis shape in magnetic circular dichroism (MCD) hysteresis magnetic field sweeps and in agreement with theoretical understandings of the interlayer coupling of the different stacking orders.[133−135] Figure 9b,c shows the hysteresis curves before and after application of hydrostatic pressure, clearly showing the change from antiferromagnetic to ferromagnetic interlayer coupling.[131] Artificially stacking CrI_3 monolayers stacked at 180° from each other has also been predicted to change the magnetic ground states of the stacking orders.[136] In addition to the extensive studies of CrI_3 and experimental demonstrations, several theoretical predictions have been made for the stacking order control of magnetism in other 2D materials. Coupling between sliding ferroelectricity and antiferromagnetism has been predicted in VS_2, where switching of the ferroelectric slide via interlayer sliding also switches the spin configuration of the in-plane interlayer antiferromagnetic state,[109] as shown schematically in Figure 9d. Tuning of the magnetic phase through interlayer sliding has also been predicted in $MnBi_2Te_4$, where ferroelectricity and antiferromagnetism where shown to coexist in the 2H-stacking (180° rotated bilayer) configuration.[110] Tuning of the magnetic phase through interlayer sliding and tmagnetoelectric coupling has also been theoretically explored in MnSe multilayers, where ref.[112] predicts switchable magnetic moments, and $MnTe_2/ZrS_2$ heterostructures, where ref.[137] predicts the switching of various topological spin textures. Along with practical device applications, such as nonvolatile electric field control of magnetism, control of the coupling between electric and magnetic orderings, generating new type of multiferroics is a promising route to explore exciting physics, such as strong magnon-phonon coupling for magnonic topology,[138−140] reconfigurable quantum simulatio,[141−143] and exotic orderings requiring magnetic or electric dipole—dipole interactions, including the dipolar Hubbard model.[109,144−146]

2.4.2. Sliding Orders Coupled with Superconductivity. In addition to the coupling between ferroelectric stacking order and magnetism, recent studies have explored the coupling of the ferroelectric stacking order and superconductivity, enabling another important 2D material property tunable by the stacking order. Such van der Waals heterostructure platform offers an exciting means of electrical control of 2D superconductivity and the potential to control electronic states in Josephson junction geometries.[147,148] For instance, the simultaneous existence of ferroelectric switching, attributed to interlayer sliding, and superconductivity was shown in bilayer T_d-$MoTe_2$.[147] The superconducting state, observed by sudden drops in the four-probe resistance (R_{xx}), was found to be closely tied to the internal electric field and could be turned on or off during ferroelectric switching if the threshold of the field-driven superconducting transition is close enough to be breached by the ferroelectric switch,[147] as can be seen in Figure 9e,f. Based on the observed need of both electron and hole pockets for superconductivity, the authors propose that an interband pairing interaction involving nearly nested electron and hole Fermi pockets could be responsible for the polarization-dependent superconductivity. Electrical control of superconductivity has also been demonstrated in magic-angle twisted bilayer graphene (tBLG) sandwiched between aligned BN layers,[148] where similar switching off and on of the superconducting state due to an external field is observed, showing great promise for control of electronic states in "magic-angle" tBLG based Josephson junction configurations.[149−152] Although a ferroelectric polarization of the magic-angle tBLG intercalated BN may be important for the observed bistability,[118−120,148] the origin of the gate hysteresis and the pairing mechanism coupling the superconductivity and ferroelectric switching remains unclear, requiring further investigations, and may likely be completely different from the mechanism proposed for bilayer T_d-$MoTe_2$. Ferroelectric switching has previously been observed in bilayer graphene sandwiched between BN layers, where the origin of the ferroelectricity is debated, possibly combining sliding ferroelectricity across layers and interlayer charge transfer driven by electron correlations.[118−120,148]

Overall, the sliding order has emerged as an exciting platform to realize different stacking configurations of layered 2D materials. Direct probes of the crystal structure, and sensitive measurements of stacking-dependent properties, allow for complete characterization of the sliding order and stacking configuration. Furthermore, dynamical control of the sliding order has now been demonstrated in many systems, enabling the tuning of exciting material properties, particularly sliding ferroelectricity. The tuning of important properties through the sliding order paves the way to understanding and harnessing the coupling of different electronic orders, such as ferroelectricity, magnetism, and superconductivity.

3. STACKING ORDER ENGINEERING ENABLED BY INTERLAYER TWIST

The discovery of superconductivity and correlated insulating states in magic-angle twisted bilayer graphene (tBLG) in 2018[21,22] led to a wide range of exploration of 2D moiré materials based on graphene, hexagonal boron nitride and various transition-metal dichalcogenides. This emergent research frontier, denoted as twistronics, suggests that a small-angle interlayer twist in vdW bilayer systems can form moiré superlattices with periodic stacking registry.[153,154] Such nanometer-scale periodic potentials can suppress electron hopping, induce flat bands with electron density of states anomalies and enable many strongly correlated phases, including 2D Mott insulator, Wigner crystal, and 1D Luttinger liquid.[155−158] Due to the attainable rich correlated phases, the twisted heterostructures are proposed to be simple yet powerful quantum simulators to interrogate the vast complex correlated Hamiltonian.[159] In this section, we will introduce the basics of moiré superlattices and the fabrication methods and then review the emergent research trends including large-

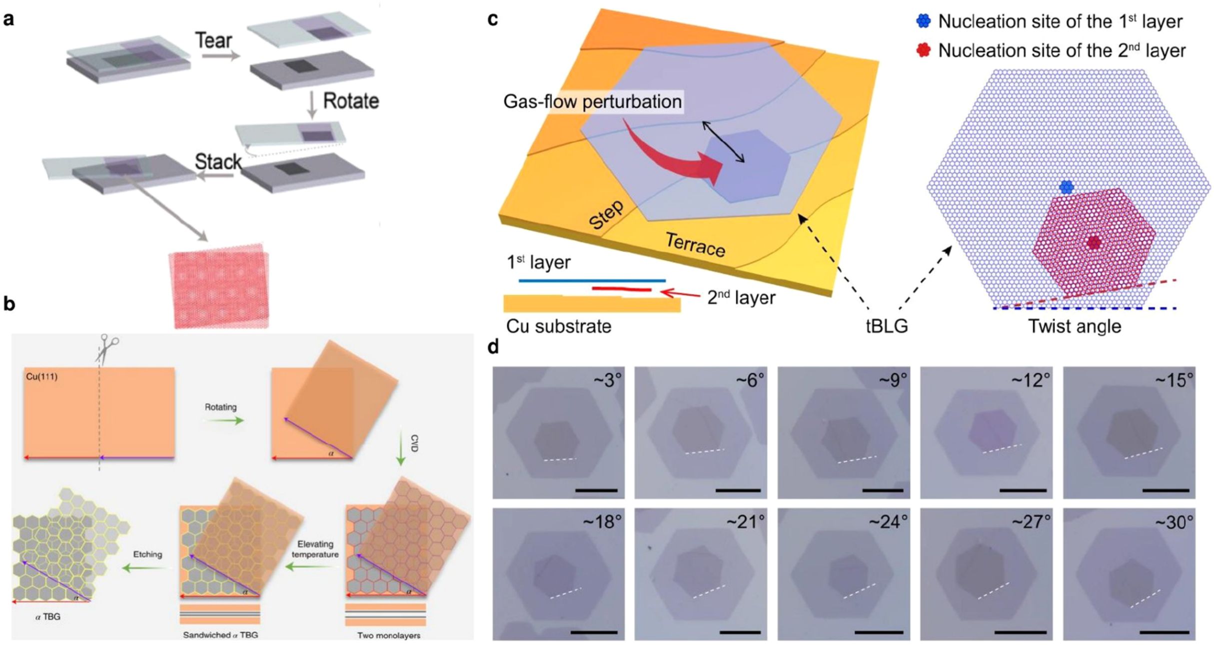

Figure 10. Fabrication of moiré superlattices. (a) Schematics of tear and stack method for twisted homobilayer fabrication. (b) Schematics of large-scale bilayer graphene growth with on-demand twist angles. A piece of single-crystal Cu foil was cut into two pieces with parallel edges (marked in red and violet). These two sections were then aligned with a rotation angle α between the marked edges. Following this, graphene was grown epitaxially between the two neighboring Cu(111) surfaces using the chemical vapor deposition (CVD) technique. Bilayer graphene with the same twist angle α was produced by raising the temperature of the copper and then isolated after removing the copper through etching. (b) Reproduced with permission from ref 162. Copyright 2022 Springer Nature. (c) Heterosite nucleation strategy for growing tBLG. It represents the schematics of heterosite nucleation growth of tBLG on a Cu substrate. By controllable gas-flow perturbation, the nucleation site of the second layer graphene (red) is different from that of the first layer (blue), allowing for different crystalline orientation growth determined by distinct surrounding environment. (d) Optical images of as-grown tBLGs with different twist angles. The scale bar is 10 μm. Reproduced with permission from ref 163. Copyright 2021 Springer Nature.

scale chemical synthesis, the new spin textures and charge orderings in bilayer twisted structures and correlated phenomena in multilayer moiré superlattices.

3.1. Moiré Geometry in Stacking Structures

A moiré superlattice arises when two slightly misaligned periodic lattices are overlaid, leading to the emergence of a new, larger periodic pattern which is distinctly different from the individual parent lattices. The corresponding interlayer coupling results in periodic moiré potentials across the twisted structures. The periodicity of moiré potentials a_M is determined by the twist angle θ, the lattice constant mismatch δ between the two layers and the average lattice constant a. In the limit of small θ and δ, a_M can be expressed as $a_M = a/\sqrt{\theta^2 + \delta^2}$. Accordingly, there are two types of twisted bilayer structures: a homobilayer built by the same monolayer compound with zero δ and a heterobilayer based on a different monolayer compound with finite δ. For both cases, in the limit $a_M \gg a$, the high- and low-energy physics set by the atomic scale and moiré length scale, respectively, are well separated. Therefore, electrons may be modeled as particles with an effective band mass (m) of the underlying monolayers, traversing within a smooth periodic moiré potential.[160] In this scenario, the electron−electron interaction U and the hopping term W can be estimated as $U \approx \frac{e^2}{4\pi\varepsilon a_M}$ and $W \approx \frac{\hbar^2 k^2}{2m_e^*} \approx \frac{\hbar^2 \pi^2}{2m_e^* {a_M}^2}$. Here ε is the effective dielectric constant, m_e^* is the electron effective mass, and a_M is the moiré period. Strong correlation with $U/W > 1$ can be achieved by proper selection of interlayer twist angle with the specific lattice constant α, the electron effective mass m_e^*, and dielectric constant ε.

3.2. Assembly of Moiré Materials

To enable on-demand strong electron correlation, the critical prerequisite is to make high-quality on-demand twisted structures. In the following, we will review the typical manual exfoliation and transfer approaches to fabricate moiré superlattices and highlight the emerging chemical synthesis methods.

3.2.1. Tear-and-Stack Method for Homobilayer Moiré Superlattice. In homobilayers, the precise control of twist angle in moiré superlattices is of great significance. To sidestep the hurdle of determining exact crystal orientation in exfoliated sheets, scientists usually work with a single exfoliated atomic layer using the tear and stack approach[49−51] (Figure 10a). For example, to make a twisted bilayer graphene, a single monolayer graphene on SiO_2/Si substrate is split into two separate flakes, one of which is picked up by a polymer handle with hBN membrane. Before using the same handle to pick up the remaining graphene, the substrate is rotated at a small angle controlled by a high-resolution goniometer stage. Finally, the hBN/graphene superlattice heterostructure will be transferred to the targeted device. This technique enables an accurate alignment of the twist angle up to 0.1°. While straightforward, the desired twist angle often differs from the targeted one due to various challenges like uneven stress, polymer flow issues, stage precision, and lattice adjustments upon assembly. Detailed discussion of fabrication reproducibility of a homobilayer moiré superlattice can be found in ref 161.

3.2.2. Polymer Assisted Dry Transfer Method for Heterobilayer Moiré Superlattice.

Moiré superlattices can also form by overlaying two atomic layers from different materials with a slight lattice mismatch. In crafting heterobilayer moiré superlattices, a typical polymer-assisted dry transfer method is used to stack two monolayers with known crystal orientations. One approach to determine the crystal orientations involves aligning the sharp edges of the two distinct materials, which can be visualized by microscopic optical imaging for certain types of 2D materials. This leverages the natural tendency of crystals to fracture along their crystallographic orientations. An alternative method involves preidentifying the crystal axis directions using noninvasive optical techniques, such as polarization-resolved second-harmonic generation (SHG), suitable for noncentrosymmetric materials. More details about this method are discussed in section 3.3.1.

3.2.3. Chemical Synthesis of Moiré Superlattice.

Despite the great success, the manual exfoliation and transfer method is time-consuming, low yield and typically at the micrometer scale. On the other hand, chemical vapor deposition (CVD) has proved to be a powerful technique to grow monolayer or few-layer 2D materials with large areas and good homogeneity. Direct growth of moiré superlattices is appealing to enable high-throughput research and large-scale applications. However, synthesis of twisted structures is challenging due to the metastable nature of twisted orders which results in relaxation back to energetically favorable nontwisted structures during the high-temperature synthesis process.[161,164−168] In the conventional CVD growth, the orientation of graphene during the growth is primarily influenced by the environmental conditions near the nucleation site, resulting in bilayer graphene originating from the same nucleation center typically displaying either identical orientations or a specific twist angle of 30° as their preferred configuration.[163] To enrich the twist angles of the bilayer graphene, recently, Sun et al.[163] reported a heterosite nucleation strategy in CVD growth by introducing a gas-flow perturbation between the nucleation of the first and second graphene layers, which can change the location of the initiation of the second layer's nucleation compared to the first layer, i.e., heterosite nucleation (Figure 10c), and thus the local environment change can result in the variety of the orientation of the new layer. In their strategy, a sudden increase of H2 and CH4 is introduced (Figure 10c) since they could supply more active hydrogen and carbon species, thus promoting the nucleation and growth of the second layer graphene. As shown in Figure 10d, the straight edges of the hexagonal tBLG have been utilized to determine the resulting θ of the tBLG from optical microscopy (OM). This unequivocally demonstrates the successful growth of tBLGs with a diverse range of twist angles. As the centers of hexagonal graphene domains conventionally serve as the primary nucleation sites for these layers, the distinct nonconcentric pattern observed in Figure 10d serves as compelling evidence confirming the heterosite nucleation behavior of the second graphene layer. Moreover, an enhanced fraction of tBLGs within bilayer graphene domains, featuring twist angles ranging from 0° to 30°, reached an impressive 88%, representing a significant improvement compared to previously reported figures.[166,167] The high crystalline quality of these as-grown tBLGs was further affirmed by the presence of well-defined moiré patterns in high-resolution (HR) transmission electron microscopy (TEM). However, this method lacks the on-demand control of twist angles in the synthetic twisted structures due to the randomness of the environment of the first and second nucleation sites and the resulting crystalline growth orientation. To realize the arbitrary twist angle control, Liu et al.[162] successfully developed a method to control the angle with high accuracy (<1.0°) in centimeter-scale TBG. The achievement of precise angle control is accomplished through a process wherein the twist angle is faithfully replicated from two prerotated single-crystal Cu(111) foils, forming a Cu/tTBG/Cu sandwich structure. Subsequently, TBG is isolated using a tailored equipotential surface etching process (see Figure 10b). To elucidate the procedure further, a single-crystal Cu(111) foil is divided into two segments with parallel edges. These two pieces are then assembled with a rotational angle α positioned between the marked edges. Subsequent to this, graphene is epitaxially grown between the two adjacent Cu(111) surfaces via the CVD method. Heating the Cu to an elevated temperature yields bilayer graphene with a twist angle α, which is eventually isolated following the removal of the Cu. The precision and consistency of these twist angles are unequivocally demonstrated through comprehensive characterization techniques, encompassing optical spectroscopy, electron microscopy, photoemission spectroscopy, and photocurrent spectroscopy. In addition to CVD, twist angles may be generated between layers grown sequentially by molecular beam epitaxy (MBE). Many studies have revealed moiré patterns in MBE grown stacks, originating from lattice mismatch and arbitrary rotation between layers.[169−174] For example, in a recent study, Khalil et al.[169] grew $WSe_2/MoSe_2$ heterobilayers on top of a graphene substrate by MBE and found coexistence of domains with arbitrary interlayer twist angles up to 4°, leading to a flat band observed by angle-resolved photoemission spectroscopy. As with CVD, control of the interlayer twist during MBE growth of stacked layers would greatly advance the scalability of moiré based heterostructures.[173]

3.3. Twist Angle and Moiré Pattern Characterization

One critical parameter in moiré superlattices is the twist angle. It determines the moiré potential periodicity and interlayer coupling strength, whose accuracy is critical to the resulting electron correlation phase diagram in moiré superlattices. Moreover, the fundamental understanding of the electronic phases also requires the accurate information on the twist angles for theoretical modeling. Thus, it is important to have methods to precisely characterize the twist angle and guide the fabrication of moiré superlattices. In section 2.1 we reviewed various methods to probe the stacking order. Here we focus on the twist angle and moiré pattern in twisted structures, reviewing several typical characterization methods.

3.3.1. Optical Spectroscopy to Identify Twist Angles.

Second harmonic generation (SHG) is a nonlinear optical process, sensitive to underlying crystal asymmetry.[72] When two layers of material are twisted against each other, the interference of light at the two layers changes the SHG signal. For example, Jin et al.[175] combined the polarization-dependent second harmonic generation (SHG) to determine the twist angle between WSe_2 and WS_2 flakes and use a dry-transfer method with a polyethylene terephthalate (PET) stamp to fabricate the WSe_2/WS_2 heterostructure. As shown in Figure f11

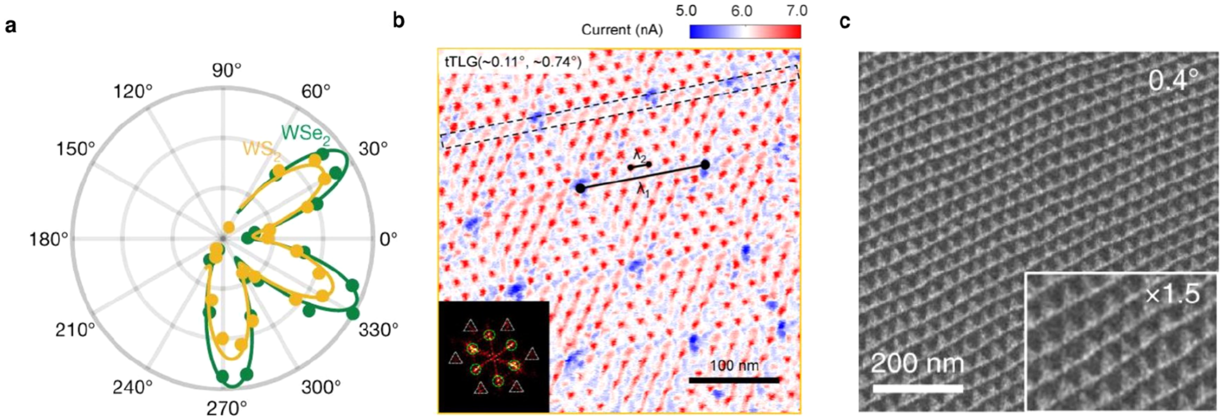

Figure 11. Twist angle and moiré pattern characterization. (a) Polarization-dependent SHG signal measured on the monolayer WSe_2 (green circles) and WS_2 (yellow circles) regions of their twisted heterobilayer and the corresponding fittings (green and yellow curves), suggesting the near-zero twist angle. Reproduced with permission from ref 175. Copyright 2019 Springer Nature. (b) Conductive AFM current map of twisted trilayer graphene double-moiré superlattices and its FFT image. Reproduced with permission from ref 177. Copyright 2022 American Chemical Society. (c) TEM dark-field images in twisted bilayer graphene showing the alternating contrast of AB/BA domains. Reproduced with permission from ref 154. Copyright 2019 Springer Nature.

11a, from the 6-fold SHG pattern, the crystal orientation of WSe_2 and WS_2 can be determined with an uncertainty of 0.3°. Additionally, as mentioned in section 2.1.1, low-frequency Raman spectroscopy may resolve folded acoustic phonon modes, known as moiré phonons, which have been shown to precisely determine the twist angle by comparing with calculated phonon dispersions.[64−66]

3.3.2. Conductive AFM To Map Stacking Domains and Twist Angles. Conductive atomic force microscopy (c-AFM) can be used to study the twist angle and moiré patterns created by stacking two-dimensional metallic materials.[176,177] In c-AFM, a conductive tip scans across the surface of the sample under investigation. The electrical current passing through the tip and the sample is measured, creating a map of local conductance or resistance. This method can provide nanoscale resolution, ideal for studying the periodicity and geometry of moiré patterns (Figure 11b). The twist angle between layers in a moiré superlattice can be inferred from observed moiré pattern periodicity.

3.3.3. TEM Imaging of Moiré Superlattices. Transmission electron microscopy (TEM) is an invaluable technique for investigating the twist angle in moiré superlattices and for mapping out domain reconstructions.[154] In TEM, an electron beam is transmitted through an ultrathin sample. The electrons' interactions with the sample generates an image revealing information about the atomic structure, crystallinity, and various other nanoscale features. High-resolution TEM (HRTEM) allows direct visualization of the atomic lattice and hence the superlattice periodicity. The moiré pattern observed in HRTEM images can be used to infer the twist angle. Furthermore, TEM can be used to map out domain reconstructions in the superlattice. This domain reconstruction is associated with metastability in the relaxation and reconstruction of the lattice structure, especially in heterostructures with very small twist angles (θ). For instance, a commensurate phase is seen in barely twisted bilayer graphene ($\theta \lesssim 0.5°$), where the lattice undergoes reconstruction to create a triangular network of alternating AB and BA stacking domains (Figure 11c).

3.4. Novel Physical Properties in Twisted Stacking Orderings

Since the first discovery of the magic-angle twisted bilayer graphene and underlying strong electron correlation, tremendous efforts have been dedicated to twisted homobilayer and heterobilayer systems based on graphene and hexagonal transition metal dichalcogenides MX_2 (M = Mo, W; X = S, Se). Several exciting many-body quantum phenomena have been discovered, including strong correlations and superconductivity in twisted bilayer graphene,[21,22] moiré excitons,[178,179] charge ordering and Wigner crystallization in transition-metal chalcogenide moiré structures.[156−158,180] These research examples have been nicely reviewed by refs 160 and 181−183. Beyond the aforementioned material platforms, the study of twistronics has recently been rapidly expanded to a broader range of 2D materials such as 2D magnets, topological 2D materials and multilayer systems. The novel interplay between spin and charge orderings in these new moiré superlattices has resulted in exotic topological and correlated phenomena including nonlinear spin textures, Luttinger liquid, fractional Chern insulators and fractional quantum Hall effect. In addition, there is an enthralling avenue of research underway that centers on exploring chemical processes influenced by the moiré physics. In this section, we will review these exciting advances dedicated to investigating new physics in new material systems as well as moiré-related chemical phenomena.

3.4.1. Noncollinear Spin Textures in Moiré Magnets. Noncollinear spin textures refers to magnetic configurations in which the orientations of individual magnetic moments do not lie uniformly along a singular axis. Noncollinear magnetism encompasses a range of unique magnetic phases, such as spiral magnetism, helical magnetism and skyrmions, which have technological potential for energy-efficient spintronic applications.[184−186] Magnetic competition, where opposing forces for different spin alignments coexist, has been identified as a key mechanism to achieve noncollinear spin textures. In light of this aspect, moiré magnetism is becoming a key tool for shaping and managing noncollinear spin textures in twisted two-dimensional magnetic crystals, where interlayer magnetic exchange competition can be controlled by local moiré atomic

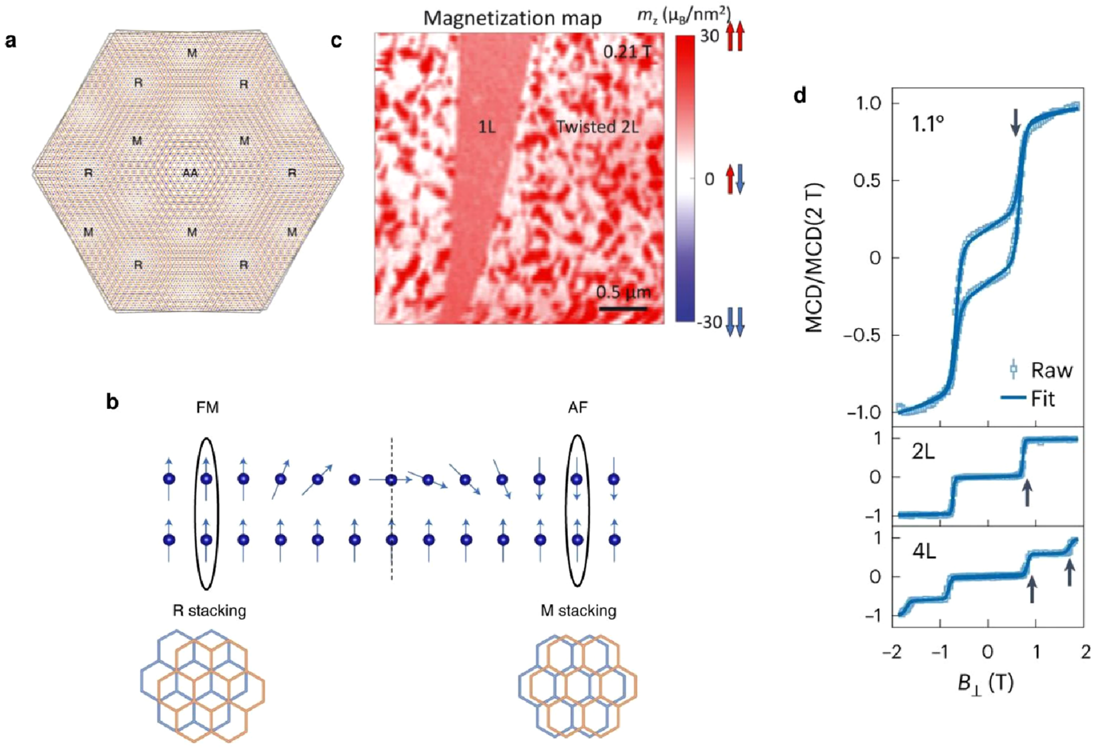

Figure 12. Moiré magnetism and noncollinear spin textures. (a) Schematics of a moiré superlattice structure of a small-twist-angle CrI_3 bilayer. R, M and AA represent rhombohedral, monoclinic and AA stacking, respectively. (b) Illustration of a magnetic domain wall with noncollinear spin textures formed between the R- and M-stacking regions. (a, b) Reproduced with permission from ref 194. Copyright 2022 Springer Nature. (c) Scanning NV magnetometry magnetization map of twisted bilayer CrI_3 at 4 K. Nanoscale antiferromagnetic (AF) and ferromagnetic (FM) domains are clearly resolved. Reproduced with permission from refs 193 and 195. Copyright 2023 Springer Nature and 2021 AAAS, respectively. (d) Out-of-plane magnetic field $B\perp$ dependent normalized MCD data at 10 K for 1.1° tDB, 2L and 4L CrI_3. Black arrows indicate the spin flip transitions.

registry. This vision was first theoretically investigated by several groups.[187−191] For instance, Hejazi et al.[188] presented a comprehensive theoretical framework using continuum field theory to study moiré patterns in two-dimensional vdW magnets.[187,188] Through this approach, they focused on twisted bilayers of Néel antiferromagnets on the honeycomb lattice and discovered a complex phase diagram with noncollinear spin textures that arise from spatial varied interlayer exchange interactions determined by underlying moiré potentials and local stacking registry. These seminal works spur a broad interest for experimental investigations in the emergent spin textures in twisted vdW magnets.[192−195] These studies focus on prototypical vdW magnet CrI_3 due to its stacking-dependent interlayer magnetism. Its magnetic ground state can transition from antiferromagnetic to ferromagnetic by altering the layer stacking from monoclinic to rhombohedral.[131,132] Accordingly, a twisted bilayer CrI_3 can showcase both monoclinic and rhombohedral stacking regions, suggesting the simultaneous presence of antiferromagnetic (AF) and ferromagnetic (FM) domains (Figure 12a). Besides, at intersections between ferromagnetic and antiferromagnetic domains, spins are expected to adopt noncollinear configurations, diverging from their typical parallel or antiparallel alignment (Figure 12b). Building upon this exciting rationale, Xie et al.[193] investigated engineering noncollinear spin textures in twisted double-bilayer (tDB) CrI_3.[195] Their research revealed optimal noncollinearity within specific twist angles. Minimal twist angles resulted in lattice alterations, favoring only monoclinic and rhombohedral stacking. In contrast, larger angles led to dominant ferromagnetic interactions, overshadowing intricate interlayer exchanges. Notably, at a near 1° twist, spins canted in one layer, producing noncollinear spin textures between ferromagnetic and antiferromagnetic domains. These textures could be adjusted with moderate magnetic fields. Using reflective magnetic circular dichroism (MCD), they studied the magnetic properties of twisted double-bilayer CrI_3 heterostructures as a function of magnetic field. While they detected common steep spin-flip patterns linked to the antiferromagnetism in thin CrI_3 layers, a distinct slowly changing magnetization with increasing applied magnetic field was observed in a near 1° twist angle CrI_3 bilayer−bilayer stacking (Figure 12d). This behavior was attributed to shifts in the noncollinear spin textures via intralayer and interlayer magnetic domain wall motion. Beyond the micrometer-scale magneto-optical probing methods, scanning single NV center spin magnetometry has been applied to interrogate the finer domain structures in twisted CrI_3.[195] With 50 nm spatial resolution, this technique used by Song et al.[195] has directly visualized the coexistence of ferromagnetic and antiferromagnetic domains (Figure 12c). However, to directly observe the noncollinear spin textures and predicted skyrmion behaviors, atomic-resolution methods such as spin-polarized scanning tunneling microscopy may be employed and a systematic phase parameter space study is needed. On the other hand, researchers are investigating the device potential of such emergent moiré magnetism. Cheng et al.[192] built a dual-gate device based on twisted bilayer−bilayer CrI_3 sandwiched by top and bottom h-BN flakes. They have observed the high electrical tunability of magnetic anisotropy and interlayer exchange in magnetic switching events. Note

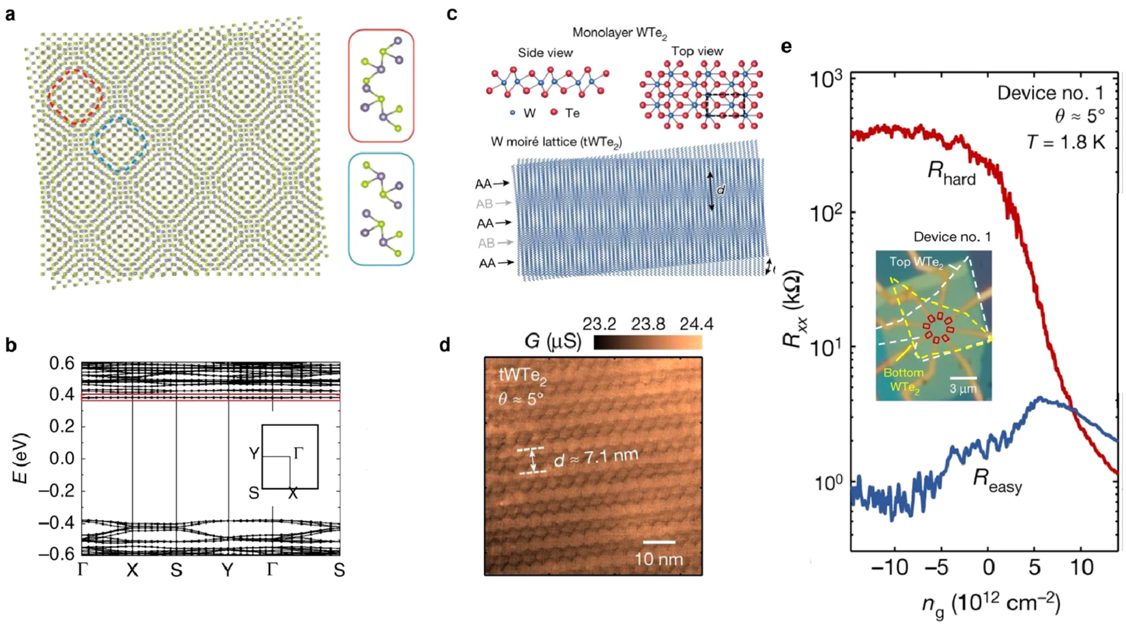

Figure 13. (a) Schematics of moiré pattern for two sheets of GeSe with rectangular unit cells stacked at a relative twist. (b) DFT band structure calculation of twisted bilayer GeSe showing emerging flat bands at the edge of conduction and valence bands. (a, b) Reproduced with permission from ref 176. Copyright 2020 Springer Nature. (c) (top) Crystal structure of monolayer WTe$_2$ with rectangular unit cell outlined by the dashed line. (bottom) Moiré superlattice by W atoms only, showing periodic 1D strips (AA and AB stripes). (d) c-AFM image of the tWTe$_2$ moiré structure showing periodic 1D strip patterns. (e) Doping dependent four-probe resistances measured for two orthogonal atomic plane directions at 1.8 K. The inset is an optical image of the corresponding tWTe$_2$ device. The dashed white (yellow) line outlines the top (bottom) monolayer WTe$_2$, and the red squares represent the contact regions. (c−e) Adapted with permission from ref 155. Copyright 2022 Springer Nature.

that CrI$_3$ may not be an ideal material platform for device applications because of their fast degradation in ambient condition, although recently developed atomic-layer deposition methods show effective protection over years.[196,197] Nevertheless, these works lay the foundation for future moiré magnetism device studies using other air-stable van der Waals magnets.

3.4.2. Luttinger Liquid Phase in Rectangular Moiré Semimetals.

The ability to engineer a certain moiré potential by the choice of the underlying lattice and the superlattice parameters can enable the study of intriguing phenomena that are challenging to realize experimentally but may be approached by a suitable moiré structure. A prime example is the Luttinger liquid (LL) model, which offers profound insights into 1D strongly correlated electronic systems.[198] Of particular interest is the expansion of this model to two dimensions, where coupled-wire models are predicted to host exotic quantum phenomena such as spin−charge separation, non-Fermi liquids, quantum Hall states, topological phases, and quantum spin liquids.[199−207] Due to the difficulty in engineering a system of tightly packed 1D wires, a genuine experimental realization has been elusive. Recently, Kennes et al.[176] predicted that 1D moiré potentials can be found in twisted bilayer germanium selenide with rectangular unit cells (Figure 13a),[176] distinct from the 2D moiré potentials observed in rhombohedral twisted bilayers. Such highly anisotropic superlattice modulation can result in a flat band along one certain dimension (Figure 13b).

Along this line, Wang et al.[155] demonstrated a 2D array of 1D Luttinger liquids in a moiré superlattice made by twisted bilayer WTe$_2$ with rectangular unit cells.[155] In the small angle twisted bilayer WTe$_2$ (tWTe$_2$) moiré lattice, the Te layer forms a triangular superlattice, while the W layer displays 1D stripe patterns (Figure 13c), highlighting the inherent anisotropy of the WTe$_2$ monolayer. In their study, such 1D stripes were visualized using conductive atomic force microscopy (Figure 13d), and corresponding twist angles can be estimated using the observed distance d between adjacent stripes as $d = a/(2\sin(\theta/2))$ for small θ values, with a being the rectangular unit cell length. Their study focuses on transport anisotropy analyses of two devices with respective angles of about 5° ($d \approx 7.2$ nm) and 6° ($d \approx 6.0$ nm). Four-probe resistance (R_{xx}, R_{hard} and R_{easy}) is measured against gate-induced doping in devices at 1.8 K for two orthogonal atomic plane directions. In Figure 13e, R_{hard} and R_{easy} show noticeable deviation when changing doping to the hole side. The resistance anisotropy ratio reaches an unusually high value near 1,000 in the hole-doped regime, which is far beyond the intrinsic resistivity anisotropy induced by the measurement geometry and the anisotropic crystal lattice. Further altering doping type or increasing temperature diminishes the anisotropy ratio to near one, implying the striking transport anisotropy is intrinsically tied to the formation of 1D Luttinger liquid ordering at the hole-doping regime. Besides the exceptionally large transport anisotropy and conductance power law analysis, the authors further conduct band structure modeling using a continuum model analysis method, which suggests that a set of distinctly anisotropic bands emerge only in the hole-doping regime. This study presents a novel gate-tunable platform using twisted WTe$_2$ stacks for future exploration of interconnected wire models with predicted exotic quantum phenomena like spin−charge separation, quantum Hall states and quantum spin liquids.[199−207]

3.4.3. Topological Phenomena in Moiré Superlattices.

Moiré superlattices of layered materials are emerging platforms for various types of topological effects and unravel rich interplay physics between topology and electron correlation,[207−219] resulting from their highly tunable flat

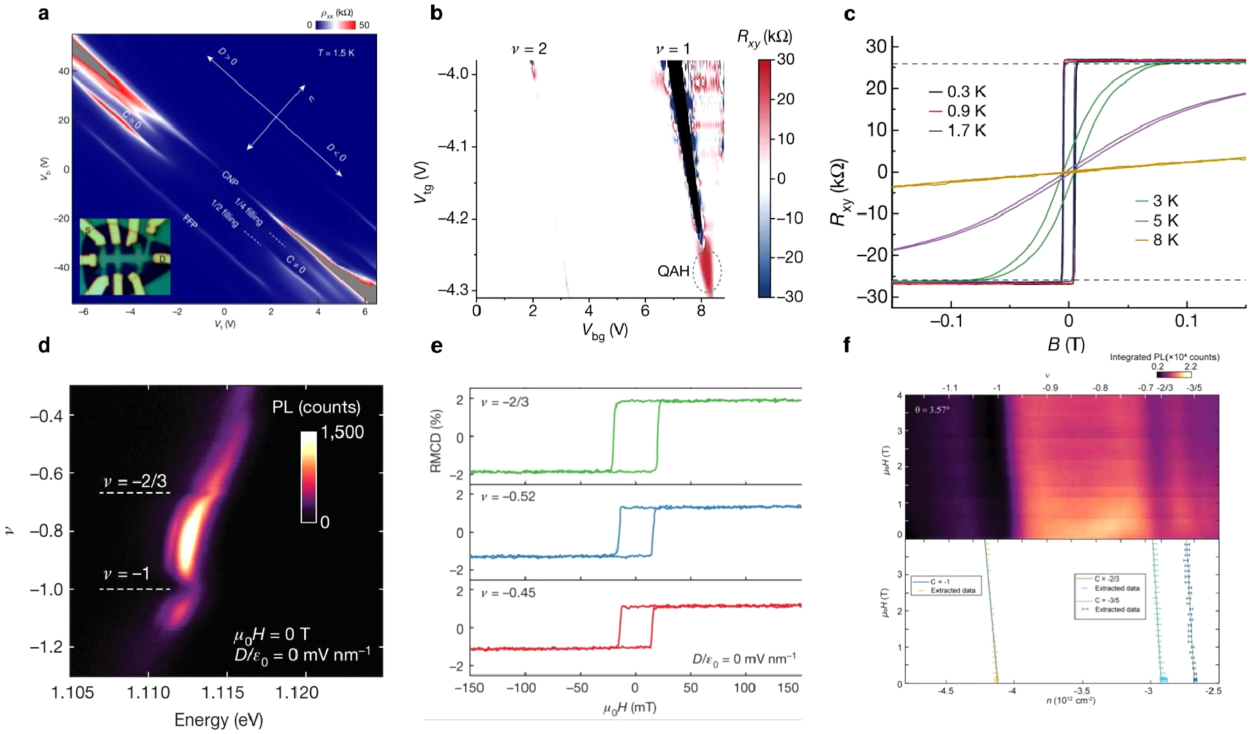

Figure 14. Topological states in moiré superlattices with strong electron correlation. (a) Longitudinal resistivity ρ_{xx} of an ABC-TLG/hBN moiré superlattice Hall bar device, as a function of top gate voltage V_t and bottom gate voltage V_b at T = 1.5 K. A correlated Chern insulator state (C = 2) is found at 1/4 filling of the hole minibands at large displacement field D. The inset shows the optical image of the device. Reproduced with permission from ref 208. Copyright 2020 Springer Nature. (b) Gate-dependent Hall resistance of AB-stacked $MoTe_2/WSe_2$ heterobilayer at 300 mK. The region of a QAH insulator state is outlined by the blue dashed circle. (c) B-field dependence of Hall resistance R_{xy} of the QAH insulator state at varying temperatures. Reproduced with permission from ref 210. Copyright 2021 Springer Nature. (d) Photoluminescence intensity plot as a function of hole doping and photon energy in twisted bilayer $MoTe_2$. The trion photoluminescence intensity drop at specific filling factors ν result from the formation of correlated insulating states. (e) Magnetic field dependent RMCD signal at selected filling factors of twisted bilayer $MoTe_2$, indicating the formation of correlated ferromagnetic states. (f) (top) Optical Landau fan diagram of twisted bilayer $MoTe_2$ by spectrally integrating PL intensity as a function of magnetic field and carrier density. (bottom) Wannier diagram with a C = −1 QAH state at v = −1 (black line), C = −2/3 fractional QAH (FQAH) state at v = −2/3, and C = −3/5 FQAH state at v = −3/5 (blue lines). The consistency between the experimental data and theoretical calculations suggests the observation of the integer and fractional QAH states. (d−f) Adapted with permission from ref 31. Copyright 2023 Springer Nature.

electronic bands, lattice geometry, and correlation effects. For instance, recently in samples of Bernal stacked-bilayer graphene/h-BN superlattices, the fractional Chern insulators have been seen in a very large magnetic field (30 T).[220] Except for a heterostructure, in a magic-angle twisted BLG, eight FCI states have been seen at low magnetic fields (5 T).[221] Pierce et al.[222] reported a series of incompressible states with unexpected Chern numbers, observable even at zero magnetic field, caused by a broken translation symmetry that doubles the moiré unit cell and divides each flavor band into two distinct bands in MATBG. In addition to the rich topological phenomena observed in MATBG, twisted monolayer−bilayer graphene (tMBG) has garnered interest due to its reduced crystal symmetry and the ability to modulate its bandwidth and topological properties through an external electric field. The anomalous Hall effect has been detected in correlated metallic states adjacent to most odd integer fillings of the flat conduction band. Furthermore, correlated Chern insulator states have been observed by applying an external magnetic field.[223] Moreover, Chen et al.[208] observed a correlated Chern insulator state and ferromagnetic state in dual-gate device geometry (Figure 14a). By manipulating the vertical displacement field, they demonstrate that the magneto-transport properties in a moiré superlattice formed by ABC-TLG/hBN exhibit contrasting behaviors for minibands characterized as trivial (C = 0) versus those with a topological nature (C ≠ 0). Notably, a correlated Chern insulator exhibiting a quantum anomalous Hall effect with C = 2 emerges when the topological hole miniband reaches approximately one-quarter filling. Such correlated Chern insulators break time-reversal symmetry spontaneously, leading to pronounced ferromagnetic hysteresis and an anomalous Hall resistance of approximately 8 kΩ even at zero external magnetic field.

The requirement of an external magnetic field may hinder the application of those topological phenomena into energy efficient nanoelectronics. A well-known example bypassing this limitation is the quantum anomalous Hall (QAH) state, which displays an integer quantum Hall effect without any magnetic field due to its inherent ferromagnetism. In 2D layered materials systems, the integer quantum anomalous Hall (QAH) state has been experimentally realized in both twisted graphene and twisted transition metal dichalcogenide (TMD) systems (Figure 14b,c).[208,210,224,225] Further integrating with strong interactions between electrons, fractional-QAH (FQAH) states without magnetic fields can arise.[226−228] These states have the potential to support fractional excitations, such as non-Abelian anyons, which are vital for topological quantum computing. Despite the great potential,

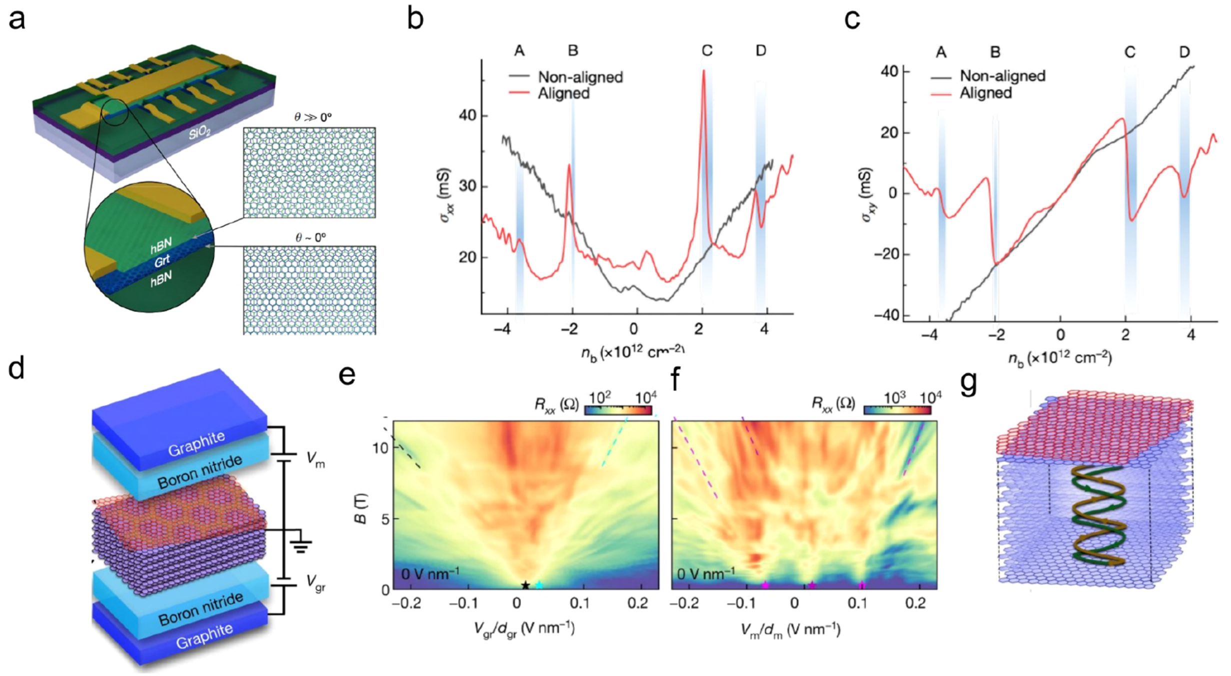

Figure 15. Mixing of moiré-surface and bulk states in twisted thin films. (a) Schematic of a graphite-BN heterostructure device with one of the interfaces aligned. (b) Graphite conductivities σ_{xx} and (c) σ_{xy} as a function of the bottom gate induced carrier density n_b, for aligned device and nonaligned device at T = 0.24 K. (a−c) Reproduced with permission from ref 250. Copyright 2023 Springer Nature. (d) Schematic of a moiré graphite thin film device including a top layer graphene on top of a thin graphite film (10 layers) with 0.84° twist angle. (e, f) Landau fan diagrams acquired by sweeping V_{gr} and V_m, respectively. Distinct from reference Bernal stacking graphite, the Landau fan diagrams in twisted graphene−graphite differ substantially depending on which gate is swept, suggesting the moiré surface state can significantly affect the bulk graphite magnetotransport. (g) Illustration of the hybridization of moiré (top red part) and bulk graphite states (blue part) at high magnetic field by the formation of a standing wave in the lowest Landau bands of graphite. (d−g) Adapted with permission from ref 238. Copyright 2023 Springer Nature.

experimental realization of the FQAH state remains a major challenge, as it requires a physical system with spontaneous symmetry breaking topology and electron correlation. Recent theoretical works propose that TMD moiré bilayers with a rhombohedral stack can support topological flat bands with contrasting Chern numbers across different spin/valley sectors.[229−233] Both integer and fractional QAH states are anticipated. Building upon these exciting inspirations, Cai et al.[31] and Zeng et al.[32] have experimentally demonstrated the predicted FQAH states at zero magnetic field in twisted $MoTe_2$ bilayers. In the former study, the authors first interrogated the photoluminescence (PL) intensity at T = 1.6 K as a function of doping density and photon energy in dual-gate twisted $MoTe_2$ devices with a twist angle of ∼3.7°. They found at filling factors ν = −1 and −2/3 in the doping regime, there is a nontrivial PL intensity drop from the trion (charged exciton) emission and the PL peak blue shift (Figure 14d). Under a magnetic field of about 1 T, a faint feature at ν = −3/5 can be seen. The noticed decrease in PL intensity is a signature of the emergence of correlated insulating states which reduces available hole particles for trion creation.[234] Through magnetic circular dichroism measurements, they further identified strong ferromagnetic states with these filling factors (Figure 14e). By using trion photoluminescence as a probe, the authors documented a Landau fan chart that displays linear alterations in carrier densities tied to the ν = −2/3 and −3/5 ferromagnetic states under a magnetic field (Figure 14f). These alterations align with the Streda formula progression for FQAH states with fractionally quantized Hall conductance values of $\sigma_{xy} = -2/3\ e^2/h$ and $-3/5\ e^2/h$. Furthermore, the ν = −1 state showcases a progression in line with a Chern number of −1, consistent with the anticipated QAH state. The topological states observed can be transitioned to topologically trivial states through electrical field control. The identified fractional quantum Hall (FQAH) states with filling fractions of −2/3 and −3/5 are anticipated to accommodate Abelian anyon excitations characterized by fractional statistics. The authors claim that there is potential to observe non-Abelian anyons in other fractional filling states with enhanced sample quality, which is foundational for achieving topological quantum computation. Moreover, these studies offer a unique platform to explore various proposed concepts in FQAH states with unparalleled control using electric fields, doping levels, temperatures, and magnetic fields.

3.4.4. Novel Physical Properties in Multilayer Twist Systems. So far, research on moiré superlattices is primarily focused on twisted bilayer structures. Recent exploration on the formation of moiré flat bands in few-layer or even thin bulk vdW materials has unleashed fundamentally new effects.[235−238] One example is the discovery of a moiré quasicrystal.[239] Quasicrystals are ordered yet aperiodic solid structures. A quasicrystalline pattern can continuously fill all available space, but it lacks translational symmetry. They are intriguing due to their ability to exhibit forbidden symmetries that are not found in standard periodic crystals. Advances in this field have led to many exciting theoretical predictions of new topological and superconducting phenomena.[240−246] However, deliberately creating quasicrystals is nontrivial, and now only a handful of examples have been demonstrated.[247,248] Thus, a versatile material system capable of on-demand engineering of

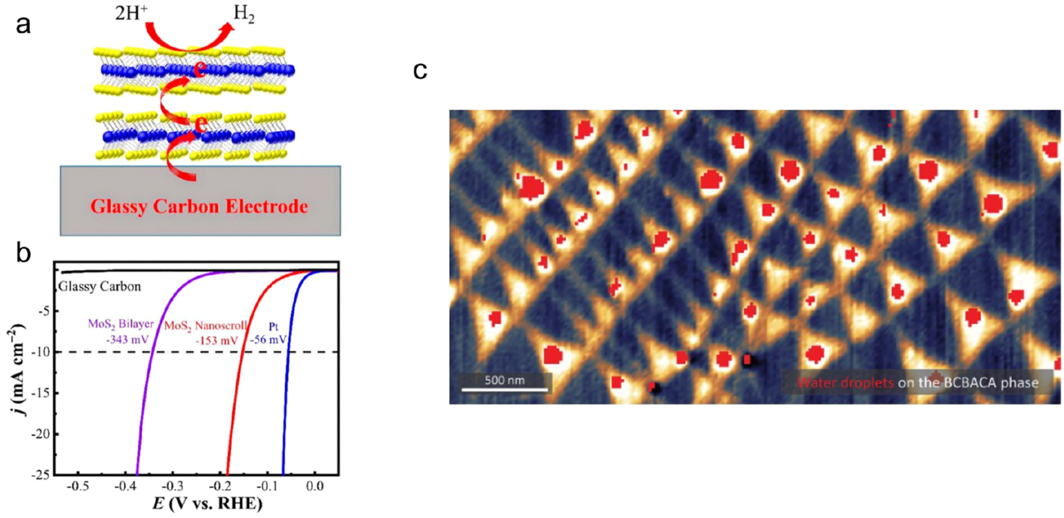

Figure 16. Moiré-assisted chemical processes. (a) Schematics of the electron transfer process in a MoS_2 moiré superlattice during hydrogen evolution reaction (HER) activities. (b) Polarization curves of the MoS_2 nanoscroll with moiré superlattice, MoS_2 bilayer, Pt, and bare glassy carbon electrodes. A lower overpotential (−153 mV) at −10 mA/cm^2 current density and a smaller Tafel slope than those in the pristine MoS_2 bilayer, suggesting a better HER performance enabled by the moiré superlattice structure. (a, b) Reproduced with permission from ref 254. Copyright 2019 American Chemical Society. (c) Near-field phase map of the twisted double trilayer graphene sample overlaid with precise positions of water droplets (red) revealed by a concurrently captured topographic map. The alignment between these water droplets and specific stacking domains indicates selective wetting governed by moiré patterns. Reproduced with permission from ref 255. Copyright 2023 American Chemical Society.

quasiperiodic patterns could expedite experimental realization of those novel theoretical concepts. Recently, Uri et al.[239] presented a novel, highly tunable quasicrystal made by twisted trilayer graphene with two distinct twist angles. The three incommensurate moiré lattices, defined by the pairs of layers i and j, form a moiré quasicrystal with the quasi-periodicity established at moiré lengths of several nanometers. To explore its electronic property, the authors measured its four-terminal resistance and found strong asymmetry in transport properties with respect to the electric displacement field D → −D, consistent with expected unequal twist angles. To verify the realization of a moiré quasicrystal, the authors further measured the longitudinal resistance as a function of the total doping density and electric displacement field D. They observed two resistive peaks at different total doping densities. An insulating state with large longitudinal resistance can occur when the moiré unit cell defined by any pair of two adjacent layers holds four electrons to fully occupy the electron bands. The observed two insulating states directly confirm the formation of a moiré quasicrystal from two incommensurate moiré unit cells. Along this line, they interrogated the correlation physics in this new system. They observed superconductivity ($T_c \approx 0.4$ K) adjacent to a flavor-symmetry-breaking phase transition, hinting at the significant role electronic interactions play in this region. Although the exact origin of the prominent presence of interaction phenomena is unclear, this study ushers in a new family of interacting quasicrystals with large tunability, which is not attainable by conventional metallic-alloy quasicrystals.[239,249,250]

Another triumph is the discovery of mixing of the moiré-surface and bulk states in graphite.[250] The findings challenge the common assumption that a moiré pattern, constrained to a singular two-dimensional interface, is unable to significantly alter the characteristics of a three-dimensional bulk crystal. In this report, the researchers investigate electronic states in thin graphite film sandwiched by hexagonal boron nitride with an aligned configuration (Figure 15a). The presence of moiré superlattice potential at the graphite/BN interface can surprisingly alter the electronic properties of the entire bulk graphite thin film. In this study, the authors constructed hBN/graphite/hBN heterostructures by positioning thin graphite films (∼5−10 nm in thickness) on an hBN substrate and encapsulating this configuration with an additional hBN crystal. They found that devices with a nonaligned interface show a nearly featureless carrier-density dependence of longitudinal $\sigma_{xx}(n)$ and transverse $\sigma_{xy}(n)$ conductivities in small B. While for the aligned graphite interface, $\sigma_{xy}(n)$ shows multiple zero crossings that are accompanied by peaks in $\sigma_{xx}(n)$ (Figure 15b,c). This suggests that a moiré superlattice at the interface of graphite markedly modifies its surface states, resulting in an entirely different transport observed between aligned and nonaligned devices. Combined with band structure calculations of Fermi-surface projections, the distinct behavior is explained by the recurrence of electrostatically induced surface states occupied by electron- or hole-like charge carriers, which dominates the bulk transport in the semimetallic graphite systems. More strikingly, the difference becomes more pronounced with a high magnetic field (>10 T) and cryogenic temperature down to 30 mK. In aligned structures with a moiré superlattice, they observed the development of Hofstadter's butterfly, the fractal quantum Hall effect, not just in the near-surface 2D states but across the entire graphite film by gating either the bottom (nonaligned) or top (aligned) moiré interface. The mixing of interfacial moiré bands and bulk electronic states is understood by two factors: the electronic system reducing from a 3D semimetal to 1D Landau bands in a strong magnetic field, and the subsequent formation of standing waves in these bands due to the finite thickness of graphite films which connect and mix the moiré interfaces and bulk electronic states (Figure 15g). This striking mixing of moiré-surface and bulk states is not alone; instead, it is expected to be universally present in semimetallic layered

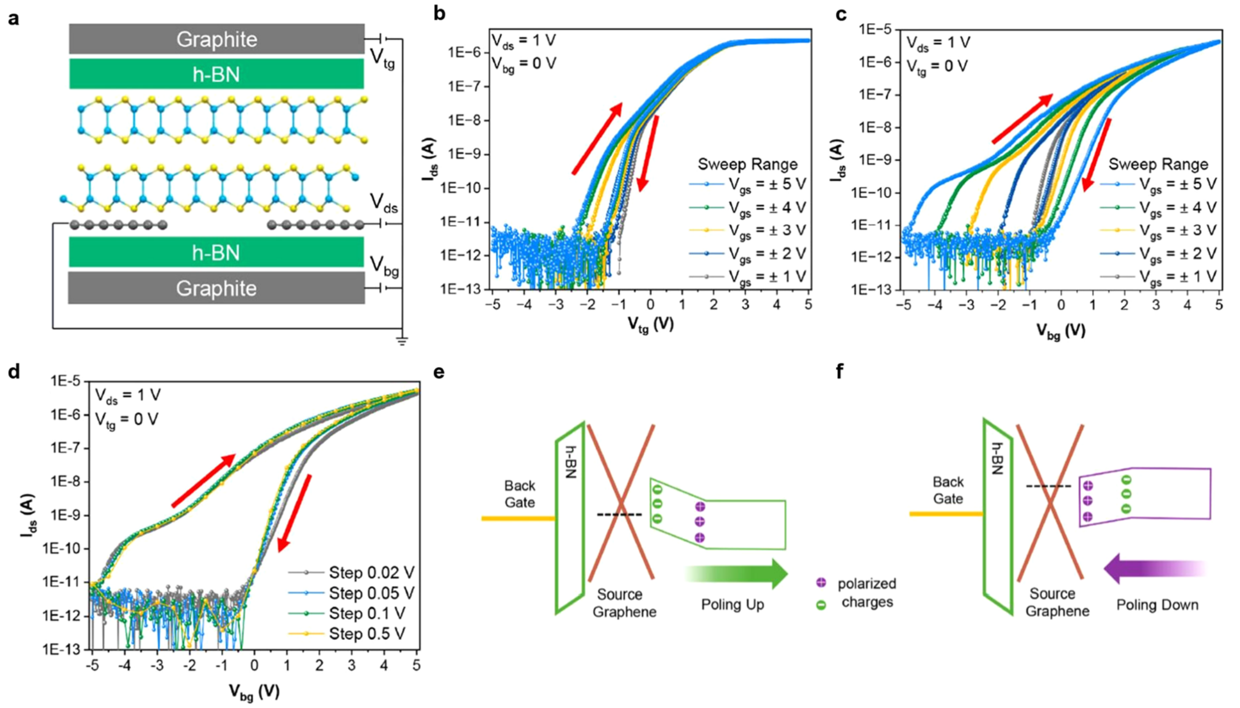

Figure 17. Transistors based on sliding ferroelectric γ-InSe. (a) Illustration of a device structure of a sliding ferroelectric channel transistor (SFeCT). (b, c) Transfer characteristics of the device modulated by the top gate and back gate, separately. (d) Schottky barrier change calculated according to (b) and (c). (e, f) Band diagram of SFeCT in two polarization states: (e) up and (f) down. (a−f) Adapted with permission from ref 257. Copyright 2023 American Chemical Society.

material systems. Similar phenomena have also been observed in another study on graphitic twist structures where the moiré potential is localized to one surface of the structure,[238] achieved by rotating a flake of monolayer graphene by a small twist angle atop a Bernal graphite thin film (Figure 15d−f). Taken together, these findings demonstrate that a single moiré interface on a graphitic thin film can significantly alter the properties of the entire film and pave the way to explore mixed dimensionality coupling physics of the interfacial moiré superlattice potential extended into various bulk 3D electronic systems with exotic quantum orderings including magnetism and superconductivity.

3.4.5. Surface Chemistry Influenced by Moiré Superlattices.

Exploring how unique moiré superlattices and the local stacking orders can affect the surface chemistry is an aspect that has been largely unexplored previously. Previous studies suggested that MoS_2 is a promising catalyst for hydrogen evolution reaction (HER) applications thanks to its low cost, earth abundance, and excellent stability.[251,252] To further improve the HER activities, interlayer potential barrier engineering is considered a critical factor because the HER process involves the hot electrons hopping from the conductive substrate to the active sites by overcoming the interlayer potential barriers.[253] Inspired by this hypothesis, Jiang et al.[254] have fabricated a MoS_2 moiré superlattice with a twist angle of about 7.3° and demonstrated enhanced HER efficiency. Pristine bilayer MoS_2 was prefabricated on 300 nm SiO_2/Si by a laser molecular beam epitaxy (LMBE) technique. Then the bilayer film was exposed to a water bath process to introduce tensile strain to form a twisted MoS_2 scroll with a moiré superlattice. The TEM results suggested that a moiré superlattice with a ∼ 7.3° twist angle was successfully created. With this twisting angle, they observed an enhancement in hydrogen evolution reaction (HER) activities using an electrochemical microcell technique, which exhibits a current density of -10 mA/cm^2 at an overpotential of -153 mV and a Tafel slope of 73 mV/dec (Figure 16a,b). The enhancement is attributed to a nontrivial reduction in interlayer potential barriers, which allows for the easy transfer of electrons from a conductive substrate to the active sites within the MoS_2 superlattice. This conclusion is further supported by first-principles calculations and ultralow frequency Raman spectra. The study provides a novel pathway to overcome limitations for further enhancing HER performance and unveils intriguing opportunities for the application of moiré superlattices in fields such as catalysis and energy storage and the development of two-dimensional functional devices.

Besides, Hsieh et al.[255] investigated the domain-dependent surface adhesion in twisted vdW heterostructures. To gain a microscopic insight, the authors applied a combination of mid-infrared near-field optical microscopy and atomic force microscopy. The study found that metallic nanoparticles (Field's metal) selectively adhere to rhombohedral stacking domains of the twisted double bilayer and double trilayer graphene, while avoiding Bernal stacking domains (Figure 16c). This domain-dependent adhesion is found to be robust across different conditions and with different materials, such as water droplets. Furthermore, the authors demonstrated that the manipulation of nanoparticles at particular stacking domains, by pushing with the AFM tip in contact mode, can alter the domain size, rearranging the moiré superlattice near the nanoparticle on the micron scale. These results shed light on a new direction for manipulating the surface chemistry and structuring of moiré systems through domain-dependent surface interactions, offering a unique approach to manipulate the surface chemistry of moiré systems.

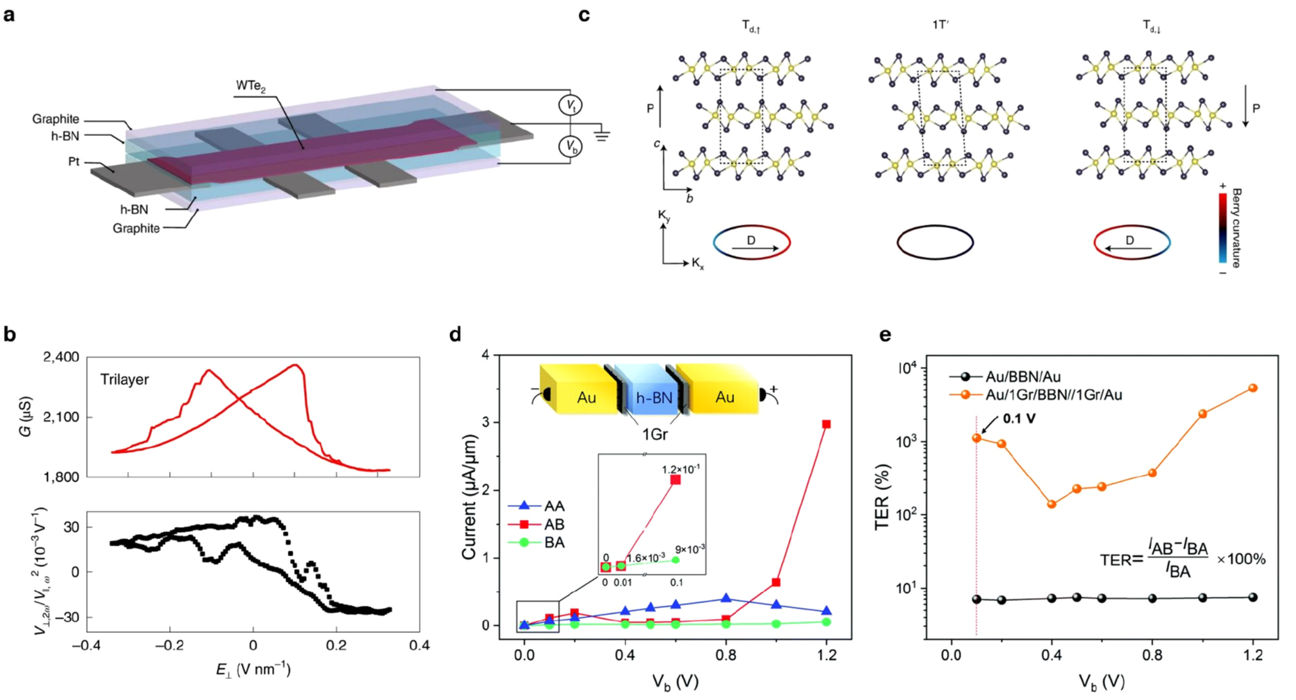

Figure 18. Memory devices based on stacking vdW materials. (a) Schematic of dual-gate h-BN-capped WTe$_2$ device. (b) Electrical conductance G with butterfly shape switching (upper plot) and nonlinear Hall signal (lower plot) in trilayer WTe$_2$. The observed nonlinear Hall signal sign is switching, which is due to the flipping of the Berry curvature dipole. (c) Side view of the unit cell along the b−c plane illustrating potential stacking sequences in WTe$_2$, including monoclinic 1T′ and polar orthorhombic T$_d$ variants ($T_{d\uparrow}$ or $T_{d\downarrow}$). Depictions of Berry curvature distribution in momentum space are also provided. Spontaneous polarization (P), Berry curvature dipole (D). Yellow spheres: W atoms. Black spheres: Te atoms. (a−c) Adapted with permission from ref 19. Copyright 2020 Springer Nature. (d) I−V outputs of the bilayer h-BN ferroelectric tunnel junctions with monolayer graphene intercalation (Au/1Gr/BBN/1Gr/Au). (e) Calculated tunneling electroresistance of the bilayer h-BN sliding ferroelectric tunnel junction with and without monolayer graphene intercalation. (d, e) Reprinted with permission from ref 262. Copyright 2022 The Royal Society of Chemistry.

4. STACKING ORDER ENGINEERING FOR DEVICE APPLICATIONS

In this section, we provide a concise overview of pivotal advancements in device development that leverage the unique attributes of stacking orders in vdW materials. Our primary aim is to highlight the distinct advantages that these stacking orders offer in the realm of device innovation. One notable benefit is the relatively low energy barrier associated with transitioning between different stacking orders, which has the potential to significantly reduce energy costs in phase transition-based devices. Additionally, the ability to manipulate twisting angles in these stacking arrangements grants an extra degree of freedom for tailoring electrical, optical, and mechanical properties. This includes the tuning of electronic band structures, thereby creating new opportunities for device optimization. Furthermore, certain stacking configurations are intentionally designed so that each layer serves a distinct purpose, resulting in multifunctional devices. In light of these advantages, we will review device developments that exploit stacking orders for a range of applications, spanning electrical, optical, and chemical domains.

4.1. Electrical Applications

The electrical modifications induced by stacking transitions hold particular promise for the creation of nonvolatile memory and electronic transistor devices. For instance, stacking orders that feature ferroelectric dipoles—such as in twisted or 3R-stacked boron nitride bilayers—have potential applications as ferroelectric dielectric materials. These could be integral to the development of ferroelectric memories and ferroelectric tunnel junctions. Furthermore, transitions in stacking orders can result in alterations to topological electronic properties. This opens new avenues for the invention of advanced quantum electronic devices.

4.1.1. Transistors. The out-of-plane polarization can be switched by interlayer translation, distinct from the ion displacement in traditional ferroelectrics. The intriguing switching mechanism makes sliding ferroelectricity promising for both fundamental research and device application. Benefiting from the weak interlayer dipole coupling, cumulative polarization states can be achieved in sliding ferroelectricity, which have been confirmed by the electrical transport measurement and Kelvin probe force microscopy.[256]

Ferroelectric materials are commonly used as dielectric materials for ferroelectric transistor development. Even though the 3R BN possesses a large bulk polarization of 7.6 μC/cm^2, most of the other sliding ferroelectricity's polarization is below the level of μC/cm^2, which limits their direct usage as dielectric materials.[36] However, Bian et al.[257] introduced a novel strategy to ferroelectric transistors by employing sliding ferroelectric materials γ-InSe as a channel material and achieved a high-performance transistor with a significantly large on/off ratio (10^6) and a wide memory window (4.5 V).[257] In their design, a γ-InSe flake was selected as a conducting channel, and a γ-InSe based dual-gate sliding ferroelectric channel transistor (SFeCT) was fabricated as shown in Figure 17a, where monolayer graphene was used as the source-drain electrodes due to its large tunability of its Fermi level.[258] The transfer characteristics of the device modulated by the top gate and back gate are illustrated in Figure 17b,c, respectively, where the drain−source voltage (V_{ds}) is fixed as 1 V. When the device is tuned by the top gate or back gate separately, a significantly larger memory window up to 4.5 V was observed with sweeping back gate, and there is a clear increase as the sweeping range of back-gate voltage increases, which was not observed in the application of the top gate. It indicates that the sliding ferroelectricity controlled by the back gate modulates the Schottky barrier between graphene and γ-InSe (see in Figure 17d−f). For example, when a positive back-gate voltage is applied, the dipole direction in γ-InSe is switched upward and induces hole doping into graphene and decreases the Fermi level in graphene due to the electrostatic effect. As a result, the Schottky barrier gets modified, even withdrawing the back gate. This process essentially achieves a memory state switching through controlling Schottky barrier with electrically tuning sliding ferroelectric polarization.[257]

4.1.2. Memory Devices.

Stacking order transition leads not only to the ferroelectric polarization switching but also changes of electronic properties such as topological properties, superconductivity, and electron correlation.[16,22,259,260] It opens a new approach toward unconventional memory devices, such as Berry curvature memory.[19] Wang et al.[261] theoretically predicted the ferroelectric nonlinear anomalous Hall effect in time-reversal invariant few-layer WTe_2 where the nonlinear anomalous Hall current changes its direction in odd-layer WTe_2 (except for the 1T′ monolayer) but stays the same in even-layer WTe_2. This even−odd oscillation is due to the different behaviors of Berry curvature dipole and shift dipole, which reverse or remain unchanged depending on the ferroelectric transformation in even- and odd-layer WTe_2.[261] An experiment by Xiao et al.[19] demonstrates that Berry curvature dipole reversal happens together with the transition between different sliding ferroelectricity orders in T_d few-layer WTe_2. Based on a dual-gate device geometry, odd layers of WTe_2 are sandwiched between two dielectric material h-BN membranes, as shown in Figure 18a. By applying an electric field to flip the polarization direction of the WTe_2 and induce sliding transition between $T_{d\uparrow}$ and $T_{d\downarrow}$ orders, the nonlinear anomalous Hall voltage switches the sign due to the reversal of Berry curvature dipole, as shown in Figure 18b,c.

Another possible group of memory devices based on sliding ferroelectric materials are ferroelectric tunnel junctions (FTJs), in which sliding ferroelectric flakes serve as a new tunneling barrier. Ferroelectric tunnel junctions (FTJs) are a type of electronic device that combines ferroelectric and tunneling phenomena. These junctions consist of two metal electrodes with a thin ferroelectric insulator layer sandwiched in between, and its spontaneous polarization can be switched by applying an electric field. This switching can lead to a change in the tunneling current in the device, which is known as the tunneling electroresistance effect.[263] The introduction of a sliding degree of freedom into the FTJs allows the development of efficient memory devices with ultralow energy cost considering the energy barrier of sliding ferroelectric switching is at the level of 1−10 meV/u.c.[34,35] For example, vdW sliding ferroelectric tunnel junctions (FTJs) have been modeled by Yang et al.[262] through first principles. The moiré pattern in bilayer hexagonal boron nitride (BBN) induces ferroelectric polarization, which can be switched by an external electric field. However, they found that the tunneling electroresistance is close to zero, indicating no ferroelectricity in BBN based SFTJs. The contradiction is caused by the fact that the metal (Au, Pt)/BBN contact electric field is very large, about 1 V/nm, and it quenches the ferroelectricity in the staggered BBN; hence, the staggered BBN loses its spontaneous polarization and its ability to switch polarization by sliding. To address this issue, graphene is utilized as an electrode material due to its low work function, approximately 4.5 eV, in contrast to metallic electrodes like Au (5.1 eV) and Pt (5.65 eV). As a result, the Gr/BBN contact electric field is around 0.3 V/nm, preventing the suppression of ferroelectricity in the staggered BBN. The Au/1Gr/BBN/1Gr/Au SFTJ can achieve a giant TER up to 10,000% (Figure 18d,e).[262]

4.2. Optical Applications

The unique stacking capabilities of vdW materials contribute to the extended lifetime of excitons by spatially separating electrons and holes, thereby reducing wave function overlaps between them. This spatial charge separation gives rise to permanent electric dipole moments or polarization dipoles in ferroelectric stacking orders. As a result, it becomes possible to design optical and excitonic devices that are controllable via external electric fields, such as photovoltaic quantum emitters and excitonic lasers. Additionally, the stacking flexibility allows for the creation of tunable heterostructure quantum wells featuring ultraclean interfaces. Moreover, the substantial exciton binding energies—on the order of 10−100 meV—in these stacked heterostructures effectively stabilize excitons, paving the way for room-temperature optical devices.

4.2.1. Photovoltaic Device.

Sliding ferroelectricity works as a new platform to develop a controllable photovoltaic effect (PVE) as spontaneous polarization and PVE are concomitant physical properties. For example, Luo et al.[264] studied the photogalvanic effect (PGE) in a narrow-band gap ferroelectric bilayer ZrI_2. They found that peak photoresponse in the bilayer β-ZrI_2 (ferroelectric) is about 5 times greater than in the bilayer s-ZrI_2 (paraelectric). The intrinsic ferroelectric field of the material enhances the separation efficiency of photogenerated carriers and decreases the recombination rate of electron−hole pairs, which results in improved efficiency of photoelectric conversion and a larger photoresponse.[264]

Besides the prerequisite polarization for charge separation, sliding ferroelectricity in ultrathin layered materials also reveals high photovoltaic efficiency thanks to its unique atomic thickness, enhanced quasiparticle interactions and ultrafast interlayer carrier dynamics. For instance, Yang et al.[265] created a photovoltaic device leveraging its homogeneous polarization based on 3R-MoS_2, which showed an external quantum efficiency of up to 16% at room temperature, a major improvement over the highest efficiency observed in bulk photovoltaic devices.[265] This record-high conversion efficiency is a result of the combination of three factors: (a) enhanced depolarization field effect (DEP) in the atomically thin rhombohedral MoS_2, (b) exciton-enhanced light−matter interaction, and (c) ultrafast interlayer relaxation. The depolarization field effect (DEP) manifests as an electric field created by the bond charge at the surface or interface where polarization concludes. When the thin film is positioned between two electrodes, the DEP becomes nonzero if the induced charges in the electrodes cannot entirely offset the polarization charges. This discrepancy leads to the movement of photocarriers and, subsequently, the generation of a photovoltaic current. The reduced screening in electrodes and thinner film thickness will help to enhance the DEP effect.

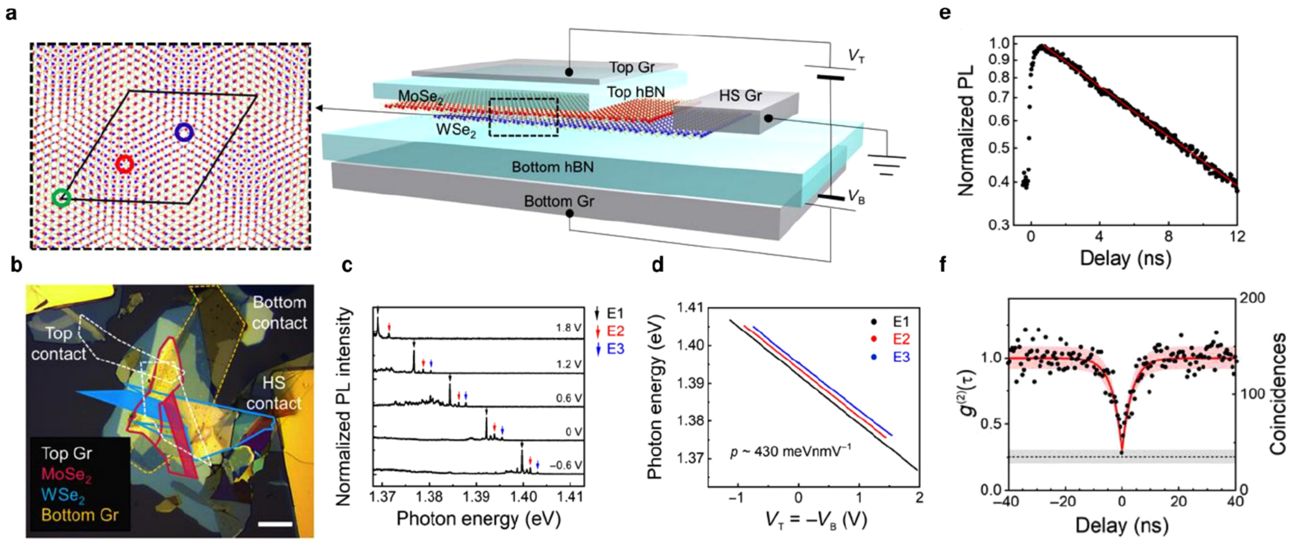

Figure 19. $MoSe_2/WSe_2$ moiré heterobilayer and quantum nature. (a, b) Schematic and optical image of the device, separately. (c) Photoluminescence (PL) spectra of excitons (IXs) at various gate voltages. The PL spectra display distinct peaks labeled as E1, E2, and E3 corresponding to different excitonic states. (d) Photon energy versus gate voltage plot for peaks E1, E2, and E3. The electrical dipole moments are fitted to be ~420 meV nm V^{-1}. (e) Time-resolved normalized PL intensity of the single emitter under 80-MHz pulsed excitation at 1.63 eV with an average excitation power of 4 μW. Lifetime is fitted to be 12.1 ± 0.3 ns by a single exponential decay fitting. (f) Second-order photon correlation statistics were conducted using 2.3 μW continuous-wave excitation at 760 nm, demonstrating clear antibunching with a $g^{(2)}(0)$ value of 0.28 ± 0.03 obtained from the fitted experimental data represented by the red solid line. (a−f) Adapted with permission from ref 268. Copyright 2020 AAAS.

By using graphene to be the electrode and few-layer rhombohedral MoS_2, they could get almost 95% of the DEP. Driven by the strong DEP, which creates a built-in potential difference between the graphene and the MoS_2, the photoexcited carriers in MoS_2 transfer to the graphene electrodes within a few picoseconds. This ultrafast interlayer relaxation can help increase the charge transfer efficiency and reduce energy loss. In the last factor, the excitons are bound pairs of electrons and holes that can couple with photons to form exciton−polaritons, which are part light and part matter. The exciton−polaritons can interact more strongly with other particles, leading to various effects. In the case of 3R-MoS_2, the exciton−polaritons can increase the charge transfer rate and directionality between the MoS_2 and the graphene, resulting in a higher photovoltaic current. Similar work has been done by Wu et al.[266] The heterostructure composed of bilayer and four-layer 3R-MoS_2 exhibited a spontaneous photovoltaic effect, where photoexcited carriers in MoS_2 transferred asymmetrically to the graphene under a largely unscreened depolarization field. The findings reveal that devices consisting of just two atomic layers of MoS_2 exhibit a photovoltaic effect with an external quantum efficiency of 10% at low temperatures, along with a picosecond-fast photocurrent response, translating to an intrinsic device bandwidth at approximately the 100-GHz level.

Finally, some sliding ferroelectrics exhibit a switchable out-of-plane polarization and an unswitchable in-plane polarization. The out-of-plane polarization induces a bulk photovoltaic effect (BPVE) along the *z*-direction, which can be reversed by flipping the ferroelectric order. On the other hand, the in-plane polarization induces a BPVE in the *xy* plane, which remains robust even when the ferroelectric order is flipped. As a result, these materials possess both switchable and unswitchable BPVE properties, offering opportunities for designing photoelectric devices with either switchable or stable characteristics.[98]

4.2.2. Quantum Emitter. The bounded electron−hole pairs (excitons) trapped in periodic moiré potentials are highly localized. Such quantum confinement results in a finite electronic density of states attainable at each moiré potential site, which can act similar to artificial atoms for quantum emission. Moreover, the properties of moiré excitons, such as emission wavelength and spin optical selection rules, can be electrically tuned, providing a unique platform for high-performance single-photon emitter arrays and entangled photon sources.[267] Yu et al.[267] reported that vdW heterobilayers based on MoX_2/WX_2 heterobilayers (M = Mo, W; X = Se, S) exhibit moiré patterns, which create superlattice potentials. Within these potentials, interlayer excitons demonstrate a distinctive spin-dependent complex hopping behavior, resulting in a remarkable spin−orbit splitting in the exciton bands. Moreover, by applying a perpendicular electric field or adjusting the moiré periodicity through strain tuning, the hopping behavior can be deactivated, effectively transforming the superlattices into precise arrays of nanodots, which act as uniform quantum emitters.[267] Baek et al.[268] built $MoSe_2/WSe_2$ moiré heterobilayer samples as shown in Figure 19a,b. By changing the top and bottom gates, the relation between moiré interlayer excitons (IXs) and external electric field revealed a tuning range of approximately 40 meV (as shown in Figure 19c,d), which is significantly larger than that observed in multilayer WSe_2 quantum dots.[269,270] Photon antibunching, a phenomenon observed in quantum optics, where photons exhibit nonclassical behavior, has been characterized by measuring the power-dependent PL and second-order correlation function $g^{(2)}$ (Figure 19e,f). The fitted $g^{(2)}(0)$ value is 0.28 ± 0.03, which is well below the threshold of 0.5 as unequivocal evidence for the quantum nature of the light emitted by the moiré-trapped IXs.[268] Furthermore, Zheng et al.[271] recently showed experimental proof of the enhanced localization of moiré excitons in the twisted $WSe_2/WS_2/WSe_2$ heterotrilayer. Multiple excitons splitting has been observed,

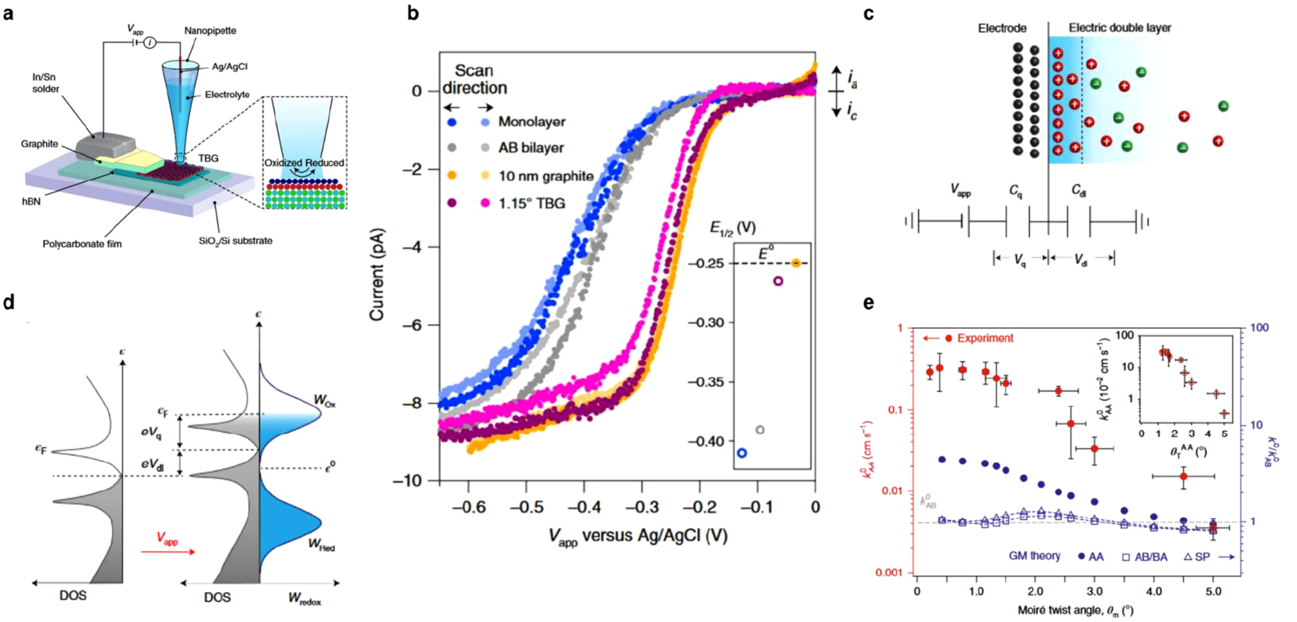

Figure 20. Schematic of the tBLG device and their electrochemical results. (a) Schematic of the SECCM setup, which is used to do the local voltammetric measurement. (b) Steady-state voltammograms of 2 mM $Ru(NH_3)_6^{3+}$ in a 0.1 M KCl solution. The insert is the half-wave potential. (c) Illustration of the interface of electrodes−electrolyte. (d) Energy diagram of interfacial charge transfer. (e) Experimental local k^0 versus θ_m compared to theoretically predicted (GM) values of k^0 at AA, AB/BA and SP stacking regions. (a−e) Adapted with permission from ref 285. Copyright 2022 Springer Nature.

which has a line width four times narrower than the moiré excitonic behavior of the twisted WSe_2/WS_2 heterobilayer.[271]

4.2.3. Interlayer Exciton Laser. The existence of room-temperature moiré excitons has been reported in MoS_2/WSe_2 heterobilayers by Lin et al.,[272] and they found that moiré potential leads to wide emission tunability and suppressed nonradiative recombination in IXs; by integrating moiré superlattices with silicon topological photonic crystal nanocavities (Q-factor, >104), they can achieve ultralow-threshold lasing with emission wavelength extended to the optical fiber communication (OFC) O-band (1260−1360 nm), high side-mode suppression ratio (SMSR), and the highest spectral coherence.[272]

Beyond the layered solid-state quantum materials, researchers have translated the moiré superlattice concept and exotic properties into photonic structures. Recently, Mao et al.[273] introduced a novel mechanism for achieving laser light confinement through what they refer to as "magic-angle lasers". This innovative approach involves the creation of localized states within periodically twisted photonic graphene-like superlattices. In their study, they fabricated two sets of triangular lattices of nanoholes within the same semiconductor membrane with a specific twist angle. Each lattice defines a photonic graphene lattice, contributing to the construction of a magic-angle flat band, while the membrane incorporates InGaAsP multiquantum wells (MQWs) as a gain material, emitting light at a telecommunication wavelength. Their investigation revealed that interlayer coupling results in a flat photonic band characterized by nondispersive features and robust field localization. In contrast to existing reports relying on a single photonic lattice, their magic-angle laser nanocavities exhibit three noteworthy distinctions: (a) These magic-angle laser nanocavities achieve confinement through mode coupling between two twisted layers of a photonic graphene lattice, eliminating the need for a full bandgap. (b) They can achieve a high quality factor (over 400,000) because there is an in-plane dominant momentum concentrated along the edges of the first Brillouin zone of the single photonic graphene lattice beneath the light cone in the strongly confined modes. (c) They can form flat bands with a significantly narrow bandwidth, enabling compact and reconfigurable nanolaser arrays.[273]

4.3. Surface Chemical Applications

Stacking engineering of atomically thin layers can enable enhancing catalytic activity and tuning chemical reactivity, by leveraging their substantial band structure modification capability. For example, monolayer 1H MoS_2 is a direct band gap semiconductor (E_g = 1.8 eV), while bilayer 2H or 3R stacking MoS_2 has an intrinsically indirect band gap (E_g is around 1.53 eV),[274] and the value may vary depending on the twist angle between the layers. For example, one study found that the indirect band gap value of 2H BL-MoS_2 increased to 1.7 eV when the twist angle was close to 60°,[275] and for 3R, the indirect band gap value decreased to 1.4 eV when the twist angle was close to 0°.[276] Besides, stacking engineering with different material species can form heterostructures with distinct bandgaps and electron affinity. Bilayer MoS_2 stacking with WSe_2 changes the band structure and leads to a 0.8 eV direct band gap and electron affinity energy as 3.9 eV while this value is 4.1 eV for pure bilayer MoS_2.[276−279] The bandgap and electron affinity engineering has been predicted to be useful for photocatalytic water splitting. For instance, by tailoring the band gap of a photocatalyst like TiO_2 through doping, which results in the distortion of the TiO_2 crystal lattice and decrease in the band gap. This enables the absorption of visible light and enhances photocatalytic activity.[280] By adjusting and properly engineering the electron affinity, researchers can control the migration and recombination of photogenerated electron−hole pairs, affecting the reaction rate at the catalytic sites and optimizing charge separation and transfer processes, thereby leading to increased reaction rates.[281]

More recently, moiré superlattices[282,283] give another freedom of the engineering of electron band structure, particularly creating electronic density states anomaly. Bilayer graphene has been shown to have a moiré flat miniband if the layers are stacked at specific twist angles, often referred to as the magic angles.[284] Given many chemical reaction processes such as catalytic reactions rely on the attainable surface active electron density, such flat band emergence with giant density of states, in principle, can significantly promote a wide range of chemical processes. Indeed, exploration of how the moiré flat band impacts electrochemical activity has attracted much attention recently. Yu et al.[285] reported that heterogeneous charge transfer kinetics of twisted bilayer graphene electrodes show strong twist-angle dependence, with the most pronounced improvement seen near the magic angle (~1.1°). To interrogate this chemical process, scanning electrochemical cell microscopy (SECCM) has been used to measure electrochemical activity of twisted bilayer graphene samples with an interlayer twist angle θ_m that is controlled in the range of 0.22−5.1° (Figure 20a). The SECCM involves a nanopipette filled with electrolyte solution that forms a nanoscale electrochemical cell with the tBLG surface. By analyzing the current that flows between the tip and the surface, SECCM can map the electrochemical activity with high spatial resolution.[286] The half-wave potential ($E_{1/2}$), which refers to the potential (or voltage) at which half of the maximum current is observed during a redox process, has been measured in the different thicknesses of graphene (Figure 20b). The anodic shift that takes place as the graphene thickness increases aligns with previous studies, while in 1.15° tBLG, even though consisting of just two graphene layers, it is similar to graphite and shows almost electrochemically reversible behavior in the thin electrode's basal plane, indicating enhanced reaction kinetics in 1.15° tBLG. This means the flat bands of tBLG, where the electrons have very low kinetic energy and high density of states, have the potential to modulate the electron transfer processes between tBLG and the solution-phase redox couple. To examine this, an external electric field (V_{app}) has been applied, which can be understood through two changes: V_q as the chemical potential and V_{dl} as the electric double layer (Figure 20c). When applying V_{app} throughout the solid−electrolyte interface, ϵ_F undergoes a shift of eV_q compared to the band edge, while eV_{dl} shifts the entire band compared to the energy of the redox molecule (Figure 20d). Since the energy levels of the states that can give or receive electrons depend on how much V_{dl} and V_q influence them, and the outer-sphere electron transfer rate constant k_{red} (for an electroreduction reaction) relies on the density of states (DOS) near ϵ_F, which can be tuned by the twist angle θ_m, this ultimately indicates that k_{red} depends on θ_m. The experiment and theoretical model have been built to examine dependence. The intrinsic electron transfer rate k^0 as outlined in the Butler−Volmer (BV) formulation is $k_{red}^{BV} = k^0\, e^{-\alpha F/RT(V_{app}-E^0)}$.[287] A potential-dependent prefactor $A(V_{app})$ has been introduced to the BV equations to accommodate the potential for variations in the DOS with V_{app}. As shown in Figure 20e, the kinetics can be influenced by the interlayer moiré twist angle, and particularly there is an enhancement between θ_m = 0.8° and θ_m = 2°. This is attributed to the increased DOS caused by the flattened bands, the energy of which is matched with the formal potential of redox couples ($Ru(NH_3)_6^{3+/2+}$). Moreover, an anomalous enhancement of k^0 at low twist angles is observed, which is also influenced by the topological defect regions. Topological defect regions are regions where the moiré pattern is disrupted by lattice mismatch or twist angle deviation. Since the main increase in DOS is localized at AA regions while much lower DOS is found at AB/BA or SP stacking regions, the predominant factor influencing the observed k^0 variation is the changing fraction of AA stacking areas when $\theta_m < 1.5°$. On the other hand, due to the pinning effect of the positive local rotations around the AA stacking sites, which are nearly unaffected by the global twist angle for $\theta_m < 1.5°$, k_{AA}^0 remains constant at about 0.2 cm s^{-1}. As θ_m increases, the effects from both the flat bands and the lattice relaxation process lessen, leading to a convergence in the rate constants k_{AA}^0 and k_{AB}^0 when θ_m is 4° or greater (Figure 20e).[285]

To conclude, the tunable nature of moiré-derived flat bands in van der Waals architectures can offer a distinctive material platform to manipulate and probe interfacial charge transfer and chemical transformations. During the atomic reconstruction of the moiré superlattice, the atoms rearrange themselves to minimize their energy and strain. This process changes the local geometry and electronic structure, which then affects its electrochemical properties. Furthermore, the localization in topological defect regions due to the moiré-derived flat bands can be tuned by the precise control of the interlayer twist angle, which can be used to control the transfer rate for the external-sphere electron transfer reaction.[288] All the exciting results show that flat-band engineering with moiré architectures is expected to become a powerful strategy for tuning the chemical reactivity of various 2D surfaces.

5. SUMMARY AND PROSPECT

In conclusion, we have reviewed the exciting progress on the new phase physics and device applications enabled by stacking engineering of layered materials. By tuning the interlayer sliding and twisting in various vdW stacking compounds, one can substantially tailor the electronic, optical and chemical properties. Looking forward, many research opportunities are anticipated for this important yet nascent field in the aspects of (1) repeatable and large-scale stacking material synthesis and processing, (2) precise and high throughput theoretical modeling, (3) broadened material choice for slidetronics and twistronics, (4) ultrafast dynamics and domain kinetics in stacking engineered materials and devices, and (5) new chemical functionality enabled by stacking engineering.

5.1. Repeatable and Large-Scale Stacking Material Synthesis and Processing

In section 3.2.3, we have reviewed the pioneering study for chip-scale synthesis of on-demand stacking structures, yet with limited demonstration only for twisted bilayer graphene with certain substrate Cu foil assistance. The lack of methods for the large-scale synthesis and assembly for a wide range of 2D heterostructures with deterministic stacking orders impedes the industrialization of devices based on these structures. Addressing this challenge requires a multipronged approach that encompasses several key areas. First, the development of scalable synthesis techniques for producing high-quality 2D heterostructures is crucial. Current approaches, such as chemical vapor deposition (CVD) and molecular beam epitaxy (MBE), have shown promise for synthesizing individual 2D materials at the wafer scale.[289−292] However, these methods need to be optimized and adapted for the synthesis of high-quality heterostructures with well-defined stacking orders including thermodynamically metastable twisted structures. As the energy difference between various stacking orders can be as low as 1−10 meV/u.c.,[34,35] a great challenge arises in the synthesis method that requires extremely accurate control over parameters. Alternatively, it urges the development of large-scale transfer techniques, leveraging the dry transfer method or the use of polymers as support layers, to enable the controlled assembly of heterostructures with deterministic stacking orders.

5.2. Precise and High Throughput Theoretical Modeling

The diverse attainable material compounds in layered materials enable hundreds of possible sliding configurations and twisting homo- and heterostructures. So far, only a very small portion of them have been explored experimentally. High throughput computational methods are urgently needed to survey and screen potential stacking orders and guide experimentalists to realize desired properties. For example, current observed sliding ferroelectrics enabled by polar stacking are with small spontaneous polarizations on the order of $0.1{-}1\frac{\mu\mathrm{C}}{\mathrm{cm}^2}$.[36] The high throughput computational material screening may facilitate the realization of sliding ferroelectrics with much larger polarization, which is more favorable for ferroelectric memory and transistor applications. On the other hand, precise theoretical modeling of moiré superlattices for their equilibrium quantum properties and collective excitations are challenging. The complexity comes from the very large moiré large unit cell to compute, strong electron correlations, and lattice reconstructions. Recently, large-scale first-principles GW plus Bethe−Salpeter calculations have been developed to study moiré excitons in WS_2/WSe_2 heterobilayers.[293] With improved accuracy compared to the typical continuum model, the study reveals a rich set of moiré excitons that could not be computationally accessed before. We expect more efforts along this line can overcome the underlying computational challenges for stacking phase engineering and lead to many new and exciting experimental discoveries.

5.3. Broadened Material Choices for Slidetronics and Twistronics

The current research on stacking orders predominantly targets graphene, h-BN, and common TMDs. However, broadening the investigation of stacking orders to encompass other 2D vdW materials, such as phosphorus, MXenes, and transition metal monochalcogenides known for their remarkable optoelectronic and magnetic properties, will pave the way for novel device innovations and a deeper understanding of interlayer coupling physics. Beyond conventional 2D materials, Janus 2D TMDs have recently emerged as promising candidates for optoelectronic applications. Their monolayers inherently break horizontal inversion symmetry, enabling an out-of-plane dipole and large nonlinear optical response[294−298] (e.g., SHG and shift photocurrent). Moreover, incorporating Janus 2D TMD monolayers into heterostructures with other conventional TMDs, such as MoS_2 and $MoSe_2$, may bolster the nonlinear optical response through enhanced interlayer coupling.[294] These unconventional 2D materials introduce new stacking orders that impact their interlayer coupling and resulting nonlinear optical properties,[294,298] yielding a promising candidate for slidetronic and twistronic based optoelectronic devices.

5.4. Domain Kinetics and Ultrafast Dynamics in Stacking Engineered Materials and Devices

By exploring the electronic structure alongside structural evolution, we can gain a deeper understanding of the relationship between stacking order and material properties, paving the way for innovative device applications and new insights into the fundamental physics of interlayer coupling. While the kinetics of stacking order transitions have been primarily explored theoretically,[34,112,120] experimental validation is essential. Although several optical experiments, such as SHG and Raman spectroscopy, have identified symmetry changes during stacking transitions, in situ structural investigations employing techniques like TEM, X-ray diffraction, or ultrafast electron diffraction are crucial. Specifically, these studies can elucidate the potential pathways for sliding transitions, offering valuable feedback for the theoretical development of the thermodynamics of stacking transitions. Additionally, incorporating multicontrol parameters into these in situ structural studies, such as electrical, optical, and mechanical fields, will enrich our understanding of thermodynamics under external perturbation and may result in the discovery of nonequilibrium stacking states. In tandem with structural evolution, probing electronic structure is essential to further illuminate the structure−property relationship in stacking transitions. Techniques like angle-resolved photoemission spectroscopy or scanning tunneling microscopy can reveal changes in band or topology during the subtle relative shifts that occur during phase transitions.

5.5. New Chemical Functionality Enabled by Stacking Engineering

In sections 3.4.5 and 4.3, we have highlighted recent explorations into the surface chemistry of moiré materials. The interlayer electron transfer behavior at the interface can be strongly modified by emergent flat bands, moiré domains and modified interlayer potentials. We expect that the manipulation strategies using moiré patterns will evolve into a universal approach for adjusting the chemical reactivity of diverse 2D material species beyond graphene and MoS_2. Moreover, the successful demonstration of large-scale moiré architectures with repeatable twist angles would be appealing for industrial chemical conversion applications.

On the other hand, the stacking engineering of layered materials can unleash the tremendous opportunities to create previously inaccessible structures for desired chemical functional properties.[5,299,300] For example, the energy storage capabilities of Ti_3C_2 MXene are often hindered by structural collapse due to layer stacking, resulting in reduced capacitance. By mimicking the superlattice effect of magic angle graphene, Wu et al.[299] have created a more stable, hexagonal few-layered Ti_3C_2 free-standing film through microscopical regulation of rotation mismatch. This not only mitigates structural issues but also greatly enhances Ti_3C_2's capacitance as a supercapacitor electrode under long charge−discharge cycles.

Overall, the engineering of interlayer sliding and twisting is one of the most important research frontiers in 2D quantum materials. The works reviewed highlight the critical role of stacking ordering engineering to discover new quantum orderings, enable efficient surface chemistry and develop high-performance electronic and optoelectronic functional devices. We hope the above prospects of stacking ordering engineering will encourage a wide range of researchers with different research backgrounds to further advance this exciting research field.

AUTHOR INFORMATION

Corresponding Author

Jun Xiao – *Department of Materials Science and Engineering, University of Wisconsin—Madison, Madison, Wisconsin 53706, United States; Department of Physics, University of Wisconsin—Madison, Madison, Wisconsin 53706, United States;* orcid.org/0000-0003-4248-8190;
Email: jun.xiao@wisc.edu

Authors

Carter Fox – *Department of Materials Science and Engineering, University of Wisconsin—Madison, Madison, Wisconsin 53706, United States; Department of Physics, University of Wisconsin—Madison, Madison, Wisconsin 53706, United States*
Yulu Mao – *Department of Electrical and Computer Engineering, University of Wisconsin—Madison, Madison, Wisconsin 53706, United States*
Xiang Zhang – *Faculty of Science, University of Hong Kong, Hong Kong, China; Faculty of Engineering, University of Hong Kong, Hong Kong, China*
Ying Wang – *Department of Materials Science and Engineering, University of Wisconsin—Madison, Madison, Wisconsin 53706, United States; Department of Physics and Department of Electrical and Computer Engineering, University of Wisconsin—Madison, Madison, Wisconsin 53706, United States;* orcid.org/0000-0002-5307-8384

Complete contact information is available at:
https://pubs.acs.org/10.1021/acs.chemrev.3c00618

Author Contributions

#C.F. and Y.M. contributed equally. CRediT: **Carter Fox** writing-original draft, writing-review & editing; **Yulu Mao** writing-original draft, writing-review & editing; **Xiang Zhang** conceptualization, writing-review & editing; **Ying Wang** conceptualization, funding acquisition, project administration, supervision, writing-review & editing; **Jun Xiao** conceptualization, funding acquisition, project administration, supervision, writing-original draft, writing-review & editing.

Notes

The authors declare no competing financial interest.

Biographies

Carter Fox is a Ph.D. candidate at the University of Wisconsin—Madison. His research is focused on precise stacking engineering of 2D materials, experimental studies of the coupling between their different orderings, and exploration of their potential electronics applications.

Yulu Mao is a Ph.D. candidate at the University of Wisconsin—Madison. Her research is primarily focused on the exploration of 2D materials and their properties using nanomechanical resonators, with a specific emphasis on their potential applications.

Xiang Zhang is the President and Vice-Chancellor of the University of Hong Kong (HKU). Prior to joining HKU, he was the inaugural Ernest S. Kuh Endowed Chair Professor at the University of California, Berkeley, and the Director of the U.S. National Science Foundation Nanoscale Science and Engineering Center (SINAM). He received his Ph.D. from U.C. Berkeley (1996). He was an assistant professor at Pennsylvania State University (1996–1999) and associate professor and full professor at UCLA (1999–2004) prior to joining Berkeley's faculty in 2004. His research focuses on materials physics, metamaterials and nanophotonics. He has published over 390 journal papers.

Ying Wang received her Ph.D. degree from the University of California at Berkeley in 2018. Since 2020, she is an assistant Professor at the Electrical and Computer Engineering Department at the UW—Madison. Her research interests are in low-dimensional quantum device development for energy and information technologies.

Jun Xiao is an assistant professor in the Department of Materials Science and Engineering at the University of Wisconsin—Madison since August 2021. Prior to joining UW—Madison, he worked as a postdoctoral scholar at Stanford University and SLAC National Accelerator Laboratory. He earned his Ph.D. in Applied Science and Technology from U.C. Berkeley (2018). His research experience and interests focus on structure–property relationships and optical to THz light–matter interactions in 2D quantum materials.

ACKNOWLEDGMENTS

C.F. and J.X. acknowledge support by the U.S. National Science Foundation under Grant No. DMR-2237761. Y.M. and Y.W. acknowledge support by the U.S. Department of Energy, Office of Basic Energy Sciences, under Award No. DE-SC0024176. X.Z. is sponsored by Hong Kong Research Grants Council under Grant No. N_HKU750/22.

LIST OF ABBREVIATIONS

ALD	atomic layer deposition
TMD	transition metal dichalcogenide
CVD	chemical vapor deposition
MBE	molecular beam epitaxy
LMBE	laser MBE
PVD	physical vapor deposition
CVT	chemical vapor transport
IR	infrared
SHG	second harmonic generation
TEM	transmission electron microscopy
HAADF-STEM	high-angle annular dark-field scanning TEM
HRTEM	high-resolution TEM
PFM	piezo force microscopy
AFM	atomic force microscopy
FM	ferromagnetic
AF	antiferromagnetic
KPFM	Kelvin probe force microscopy
c-AFM	conductive atomic force microscopy
DFT	density functional theory
NEB	nudged-elastic-band
KPFM	Kelvin probe force microscopy
MATBG	magic-angle twisted bilayer graphene
tMBG	twisted monolayer–bilayer graphene
u.c.	unit cell
BN	boron nitride
hBN or h-BN	hexagonal boron nitride
BBN	bilayer hexagonal boron nitride
SFeCT	sliding ferroelectric channel transistor
V_{ds}	drain–source voltage
FTJs	ferroelectric tunnel junctions
SDF	sliding degree of freedom
PVE	photovoltaic effect
DEP	depolarization field

BPVE	bulk photovoltaic effect
IXs	interlayer excitons
PL	photoluminescence
OFC	optical fiber communication
SMSR	side-mode suppression ratio
MQWs	multiquantum wells
SECCM	scanning electrochemical cell microscopy
TBG,	t-BLG or tBLG twisted bilayer graphene
DOS	density of states
BV	Butler−Volmer
vdW	van der Waals
OM	optical microscopy
FFT	fast Fourier transform
tDB	twisted double bilayer
$tWTe_2$	twisted bilayer WTe_2
MCD	magnetic circular dichroism
TLG	trilayer graphene
QAH	quantum anomalous Hall
FQAH	fractional-QAH
HER	hydrogen evolution reaction

Symbols

λ	wavelength in free space
n	refractive index
$E_{1/2}$	half-wave potential
k^0	intrinsic electron transfer rate
k^0_{AB}	intrinsic electron transfer rate in AB stacking regions
k^0_{AA}	intrinsic electron transfer rate in AA stacking regions
F	Fermi level energy
θ_m	twist angles
k_{red}	outer-sphere electron transfer rate constant
k^{BV}_{red}	rate constant for the reduction reaction derived from the BV model
α	transfer coefficient
R	molar gas constant
F	Faraday constant
a_M	moiré periodicity
δ	lattice constant mismatch
a	lattice constant
U	electron−electron interaction term
W	hopping term
ε	effective dielectric constant
m_e^*	electron effective mass
$\hbar$	reduced Planck's constant
h	Planck's constant
e	elementary charge

REFERENCES

(1) Jones, N. How to Stop Data Centres from Gobbling up the World's Electricity. *Nature* **2018**, *561*, 163−166.

(2) Salahuddin, S.; Ni, K.; Datta, S. The Era of Hyper-Scaling in Electronics. *Nat. Electron.* **2018**, *1*, 442−450.

(3) Pham, P. V.; Bodepudi, S. C.; Shehzad, K.; Liu, Y.; Xu, Y.; Yu, B.; Duan, X. 2D Heterostructures for Ubiquitous Electronics and Optoelectronics: Principles, Opportunities, and Challenges. *Chem. Rev.* **2022**, *122*, 6514−6613.

(4) Xiao, J.; Zhao, M.; Wang, Y.; Zhang, X. Excitons in Atomically Thin 2D Semiconductors and Their Applications. *Nanophotonics.* **2017**, *6*, 1309−1328.

(5) Wu, Y.; Wang, J.; Li, Y.; Zhou, J.; Wang, B. Y.; Yang, A.; Wang, L. W.; Hwang, H. Y.; Cui, Y. Observation of an Intermediate State during Lithium Intercalation of Twisted Bilayer MoS2. *Nat. Commun.* **2022**, *13*, 3008.

(6) Liu, X.; Hersam, M. C. 2D Materials for Quantum Information Science. *Nat. Rev. Mater. 1* **2019**, *4*, 669−684.

(7) Li, W.; Qian, X.; Li, J. Phase Transitions in 2D Materials. *Nat. Rev. Mater.* **2021**, *6*, 829−846.

(8) Miao, F.; Liang, S. J.; Cheng, B. Straintronics with van Der Waals Materials. *npj Quantum Mater.* **2021**, *6*, 59.

(9) Kim, J. Y.; Ju, X.; Ang, K. W.; Chi, D. Van Der Waals Layer Transfer of 2D Materials for Monolithic 3D Electronic System Integration: Review and Outlook. *ACS Nano* **2023**, *17*, 1831−1844.

(10) Schranghamer, T. F.; Sharma, M.; Singh, R.; Das, S. Review and Comparison of Layer Transfer Methods for Two-Dimensional Materials for Emerging Applications. *Chem. Soc. Rev.* **2021**, *50*, 11032−11054.

(11) Zhang, L.; Dong, J.; Ding, F. Strategies, Status, and Challenges in Wafer Scale Single Crystalline Two-Dimensional Materials Synthesis. *Chem. Rev.* **2021**, *121*, 6321−6372.

(12) Cai, Z.; Liu, B.; Zou, X.; Cheng, H. M. Chemical Vapor Deposition Growth and Applications of Two-Dimensional Materials and Their Heterostructures. *Chem. Rev.* **2018**, *118*, 6091−6133.

(13) Watson, A. J.; Lu, W.; Guimarães, M. H. D.; Stöhr, M. Transfer of Large-Scale Two-Dimensional Semiconductors: Challenges and Developments. *2D Mater.* **2021**, *8*, 032001.

(14) Li, P.; Wen, Y.; He, X.; Zhang, Q.; Xia, C.; Yu, Z. M.; Yang, S. A.; Zhu, Z.; Alshareef, H. N.; Zhang, X. X. Evidence for Topological Type-II Weyl Semimetal WTe2. *Nat. Commun.* **2017**, *8*, 2150.

(15) Armitage, N. P.; Mele, E. J.; Vishwanath, A. Weyl and Dirac Semimetals in Three-Dimensional Solids. *Rev. Mod. Phys.* **2018**, *90*, 015001.

(16) Ju, L.; Shi, Z.; Nair, N.; Lv, Y.; Jin, C.; Velasco, J.; Ojeda-Aristizabal, C.; Bechtel, H. A.; Martin, M. C.; Zettl, A.; Analytis, J.; Wang, F. Topological Valley Transport at Bilayer Graphene Domain Walls. *Nature* **2015**, *520*, 650−655.

(17) Suzuki, R.; Sakano, M.; Zhang, Y. J.; Akashi, R.; Morikawa, D.; Harasawa, A.; Yaji, K.; Kuroda, K.; Miyamoto, K.; Okuda, T.; et al. Valley-Dependent Spin Polarization in Bulk MoS2 with Broken Inversion Symmetry. *Nat. Nanotechnol.* **2014**, *9*, 611−617.

(18) Fei, Z.; Zhao, W.; Palomaki, T. A.; Sun, B.; Miller, M. K.; Zhao, Z.; Yan, J.; Xu, X.; Cobden, D. H. Ferroelectric Switching of a Two-Dimensional Metal. *Nature* **2018**, *560*, 336−339.

(19) Xiao, J.; Wang, Y.; Wang, H.; Pemmaraju, C. D.; Wang, S.; Muscher, P.; Sie, E. J.; Nyby, C. M.; Devereaux, T. P.; Qian, X.; et al. Berry Curvature Memory through Electrically Driven Stacking Transitions. *Nat. Phys.* **2020**, *16*, 1028−1034.

(20) Wang, X.; Yasuda, K.; Zhang, Y.; Liu, S.; Watanabe, K.; Taniguchi, T.; Hone, J.; Fu, L.; Jarillo-Herrero, P. Interfacial Ferroelectricity in Rhombohedral-Stacked Bilayer Transition Metal Dichalcogenides. *Nat. Nanotechnol.* **2022**, *17*, 367−371.

(21) Cao, Y.; Fatemi, V.; Fang, S.; Watanabe, K.; Taniguchi, T.; Kaxiras, E.; Jarillo-Herrero, P. Unconventional Superconductivity in Magic-Angle Graphene Superlattices. *Nature* **2018**, *556*, 43−50.

(22) Cao, Y.; Fatemi, V.; Demir, A.; Fang, S.; Tomarken, S. L.; Luo, J. Y.; Sanchez-Yamagishi, J. D.; Watanabe, K.; Taniguchi, T.; Kaxiras, E.; et al. Correlated Insulator Behaviour at Half-Filling in Magic-Angle Graphene Superlattices. *Nature* **2018**, *556*, 80−84.

(23) Wang, Y.; Xiao, J.; Zhu, H.; Li, Y.; Alsaid, Y.; Fong, K. Y.; Zhou, Y.; Wang, S.; Shi, W.; Wang, Y.; et al. Structural Phase Transition in Monolayer MoTe2 Driven by Electrostatic Doping. *Nature* **2017**, *550*, 487−491.

(24) Li, Y.; Duerloo, K. A. N.; Wauson, K.; Reed, E. J. Structural Semiconductor-to-Semimetal Phase Transition in Two-Dimensional Materials Induced by Electrostatic Gating. *Nat. Commun.* **2016**, *7*, 10671.

(25) Xiao, J.; Zhu, H.; Wang, Y.; Feng, W.; Hu, Y.; Dasgupta, A.; Han, Y.; Wang, Y.; Muller, D. A.; Martin, L. W.; et al. Intrinsic Two-Dimensional Ferroelectricity with Dipole Locking. *Phys. Rev. Lett.* **2018**, *120*, 227601.

(26) Chang, K.; Liu, J.; Lin, H.; Wang, N.; Zhao, K.; Zhang, A.; Jin, F.; Zhong, Y.; Hu, X.; Duan, W.; et al. Discovery of Robust In-Plane Ferroelectricity in Atomic-Thick SnTe. *Science* **2016**, *353*, 274−278.

(27) Tsen, A. W.; Hovden, R.; Wang, D.; Kim, Y. D.; Spoth, K. A.; Liu, Y.; Lu, W.; Sun, Y.; Hone, J. C.; Kourkoutis, L. F.; Kim, P.; et al.

Structure and Control of Charge Density Waves in Two-Dimensional 1T-TaS2. *Proc. Natl. Acad. Sci. U. S. A.* **2015**, *112*, 15054−15059.

(28) Wang, X.; Song, Z.; Wen, W.; Liu, H.; Wu, J.; Dang, C.; Hossain, M.; Iqbal, M. A.; Xie, L. Potential 2D Materials with Phase Transitions: Structure, Synthesis, and Device Applications. *Adv. Mater.* **2019**, *31*, 1804682.

(29) Yin, X.; Tang, C. S.; Zheng, Y.; Gao, J.; Wu, J.; Zhang, H.; Chhowalla, M.; Chen, W.; Wee, A. T. S. Recent Developments in 2D Transition Metal Dichalcogenides: Phase Transition and Applications of the (Quasi-)Metallic Phases. *Chem. Soc. Rev.* **2021**, *50*, 10087−10115.

(30) Cui, C.; Xue, F.; Hu, W. J.; Li, L. J. Two-Dimensional Materials with Piezoelectric and Ferroelectric Functionalities. *npj 2D Mater. Appl.* **2018**, *2*, 18.

(31) Cai, J.; Anderson, E.; Wang, C.; Zhang, X.; Liu, X.; Holtzmann, W.; Zhang, Y.; Fan, F.; Taniguchi, T.; Watanabe, K.; et al. Signatures of Fractional Quantum Anomalous Hall States in Twisted MoTe2. *Nature* **2023**, *622*, 63−68.

(32) Zeng, Y.; Xia, Z.; Kang, K.; Zhu, J.; Knüppel, P.; Vaswani, C.; Watanabe, K.; Taniguchi, T.; Mak, K. F.; Shan, J. Thermodynamic Evidence of Fractional Chern Insulator in Moiré MoTe2. *Nature* **2023**, *622*, 69−73.

(33) Reddy, A. P.; Alsallom, F.; Zhang, Y.; Devakul, T.; Fu, L. Fractional Quantum Anomalous Hall States in Twisted Bilayer MoTe2 and WSe2. *Phys. Rev. B* **2023**, *108*, 085117.

(34) Yang, Q.; Wu, M.; Li, J. Origin of Two-Dimensional Vertical Ferroelectricity in WTe 2 Bilayer and Multilayer. *J. Phys. Chem. Lett.* **2018**, *9*, 7160−7164.

(35) Li, L.; Wu, M. Binary Compound Bilayer and Multilayer with Vertical Polarizations: Two-Dimensional Ferroelectrics, Multiferroics, and Nanogenerators. *ACS Nano* **2017**, *11*, 6382−6388.

(36) Wu, M.; Li, J. Sliding Ferroelectricity in 2D van Der Waals Materials: Related Physics and Future Opportunities. *Proc. Natl. Acad. Sci. U. S. A.* **2021**, *118*, 50.

(37) Yang, D.; Hu, X.; Zhuang, M.; Ding, Y.; Zhou, S.; Li, A.; Yu, Y.; Li, H.; Luo, Z.; Gan, L.; et al. Inversion Symmetry Broken 2D 3R-MoTe2. *Adv. Funct. Mater.* **2018**, *28*, 1800785.

(38) You, J.; Hossain, M. D.; Luo, Z. Synthesis of 2D Transition Metal Dichalcogenides by Chemical Vapor Deposition with Controlled Layer Number and Morphology. *Nano. Convergence.* **2018**, *5*, 26.

(39) Choi, W.; Choudhary, N.; Han, G. H.; Park, J.; Akinwande, D.; Lee, Y. H. Recent Development of Two-Dimensional Transition Metal Dichalcogenides and Their Applications. *Mater. Today* **2017**, *20*, 116−130.

(40) Mattinen, M.; Leskelä, M.; Ritala, M. Atomic Layer Deposition of 2D Metal Dichalcogenides for Electronics, Catalysis, Energy Storage, and Beyond. *Adv. Mater. Interfaces.* **2021**, *8*, 2001677.

(41) Zhang, Y.; Chang, T. R.; Zhou, B.; Cui, Y. T.; Yan, H.; Liu, Z.; Schmitt, F.; Lee, J.; Moore, R.; Chen, Y.; et al. Direct Observation of the Transition from Indirect to Direct Bandgap in Atomically Thin Epitaxial MoSe2. *Nat. Nanotechnol.* **2014**, *9*, 111−115.

(42) Muratore, C.; Hu, J. J.; Wang, B.; Haque, M. A.; Bultman, J. E.; Jespersen, M. L.; Shamberger, P. J.; McConney, M. E.; Naguy, R. D.; Voevodin, A. A. Continuous Ultra-Thin MoS2 Films Grown by Low-Temperature Physical Vapor Deposition. *Appl. Phys. Lett.* **2014**, *104*, 261604.

(43) Le, T. H.; Oh, Y.; Kim, H.; Yoon, H. Exfoliation of 2D Materials for Energy and Environmental Applications. *Chem. Eur. J.* **2020**, *26*, 6360−6401.

(44) Ubaldini, A.; Jacimovic, J.; Ubrig, N.; Giannini, E. Chloride-Driven Chemical Vapor Transport Method for Crystal Growth of Transition Metal Dichalcogenides. *Cryst. Growth Des.* **2013**, *13*, 4453−4459.

(45) Zhang, X.; Lou, F.; Li, C.; Zhang, X.; Jia, N.; Yu, T.; He, J.; Zhang, B.; Xia, H.; Wang, S.; et al. Flux Method Growth of Bulk MoS2 Single Crystals and Their Application as a Saturable Absorber. *CrystEngComm* **2015**, *17*, 4026−4032.

(46) Edelberg, D.; Rhodes, D.; Kerelsky, A.; Kim, B.; Wang, J.; Zangiabadi, A.; Kim, C.; Abhinandan, A.; Ardelean, J.; Scully, M.; et al. Approaching the Intrinsic Limit in Transition Metal Diselenides via Point Defect Control. *Nano Lett.* **2019**, *19*, 4371−4379.

(47) Shi, J.; Yu, P.; Liu, F.; He, P.; Wang, R.; Qin, L.; Zhou, J.; Li, X.; Zhou, J.; Sui, X.; et al. 3R MoS2 with Broken Inversion Symmetry: A Promising Ultrathin Nonlinear Optical Device. *Adv. Mater.* **2017**, *29*, 1701486.

(48) Mao, N.; Luo, Y.; Chiu, M. H.; Shi, C.; Ji, X.; Pieshkov, T. S.; Lin, Y.; Tang, H. L.; Akey, A. J.; Gardener, J. A.; et al. Giant Nonlinear Optical Response via Coherent Stacking of In-Plane Ferroelectric Layers. *Adv. Mater.* **2023**, *35*, 2210894.

(49) Cao, Y.; Luo, J. Y.; Fatemi, V.; Fang, S.; Sanchez-Yamagishi, J. D.; Watanabe, K.; Taniguchi, T.; Kaxiras, E.; Jarillo-Herrero, P. Superlattice-Induced Insulating States and Valley-Protected Orbits in Twisted Bilayer Graphene. *Phys. Rev. Lett.* **2016**, *117*, 116804.

(50) Kim, K.; DaSilva, A.; Huang, S.; Fallahazad, B.; Larentis, S.; Taniguchi, T.; Watanabe, K.; LeRoy, B. J.; MacDonald, A. H.; Tutuc, E. Tunable Moiré Bands and Strong Correlations in Small-Twist-Angle Bilayer Graphene. *Proc. Natl. Acad. Sci. U. S. A.* **2017**, *114*, 3364−3369.

(51) Kim, K.; Yankowitz, M.; Fallahazad, B.; Kang, S.; Movva, H. C. P.; Huang, S.; Larentis, S.; Corbet, C. M.; Taniguchi, T.; Watanabe, K.; Banerjee, S. K.; Leroy, B. J.; Tutuc, E. Van Der Waals Heterostructures with High Accuracy Rotational Alignment. *Nano Lett.* **2016**, *16*, 1989−1995.

(52) Liang, F.; Xu, H.; Wu, X.; Wang, C.; Luo, C.; Zhang, J. Raman Spectroscopy Characterization of Two-Dimensional Materials. *Chin. Phys. B* **2018**, *27*, 037802.

(53) Zhang, X.; Qiao, X. F.; Shi, W.; Wu, J. B.; Jiang, D. S.; Tan, P. H. Phonon and Raman Scattering of Two-Dimensional Transition Metal Dichalcogenides from Monolayer, Multilayer to Bulk Material. *Chem. Soc. Rev.* **2015**, *44*, 2757−2785.

(54) Zhang, X.; Han, W. P.; Qiao, X. F.; Tan, Q. H.; Wang, Y. F.; Zhang, J.; Tan, P. H. Raman Characterization of AB-and ABC-Stacked Few-Layer Graphene by Interlayer Shear Modes. *Carbon* **2016**, *99*, 118−122.

(55) Liang, L.; Zhang, J.; Sumpter, B. G.; Tan, Q. H.; Tan, P. H.; Meunier, V. Low-Frequency Shear and Layer-Breathing Modes in Raman Scattering of Two-Dimensional Materials. *ACS Nano* **2017**, *11*, 11777−11802.

(56) Lui, C. H.; Ye, Z.; Keiser, C.; Barros, E. B.; He, R. Stacking-Dependent Shear Modes in Trilayer Graphene. *Appl. Phys. Lett.* **2015**, *106*, 041904.

(57) Sam, R. T.; Umakoshi, T.; Verma, P. Probing Stacking Configurations in a Few Layered MoS2 by Low Frequency Raman Spectroscopy. *Sci. Rep.* **2020**, *10*, 21227.

(58) Van Baren, J.; Ye, G.; Yan, J. A.; Ye, Z.; Rezaie, P.; Yu, P.; Liu, Z.; He, R.; Lui, C. H. Stacking-Dependent Interlayer Phonons in 3R and 2H MoS2. *2d Mater.* **2019**, *6*, 025022.

(59) Cheong, H.; Cheon, Y.; Lim, S. Y.; Kim, K. Structural Phase Transition and Interlayer Coupling in Few-Layer 1t' and Td Mote2. *ACS Nano* **2021**, *15*, 2962−2970.

(60) Cheong, H.; Cheon, Y.; Lim, S. Y.; Kim, K. Structural Phase Transition and Interlayer Coupling in Few-Layer 1t' and Td Mote2. *ACS Nano* **2021**, *15*, 2962−2970.

(61) Plechinger, G.; Heydrich, S.; Eroms, J.; Weiss, D.; Schüller, C.; Korn, T. Raman Spectroscopy of the Interlayer Shear Mode in Few-Layer MoS 2 Flakes. *Appl. Phys. Lett.* **2012**, *101*, 101906.

(62) Zhao, Y.; Luo, X.; Li, H.; Zhang, J.; Araujo, P. T.; Gan, C. K.; Wu, J.; Zhang, H.; Quek, S. Y.; Dresselhaus, M. S.; et al. Interlayer Breathing and Shear Modes in Few-Trilayer MoS2 and WSe2. *Nano Lett.* **2013**, *13*, 1007−1015.

(63) Lorchat, E.; Froehlicher, G.; Berciaud, S. Splitting of Interlayer Shear Modes and Photon Energy Dependent Anisotropic Raman Response in N-Layer ReSe2 and ReS2. *ACS Nano* **2016**, *10*, 2752−2760.

(64) Parzefall, P.; Holler, J.; Scheuck, M.; Beer, A.; Lin, K. Q.; Peng, B.; Monserrat, B.; Nagler, P.; Kempf, M.; Korn, T.; et al. Moiré

Phonons in Twisted MoSe2-WSe2 Heterobilayers and Their Correlation with Interlayer Excitons. *2d Mater.* **2021**, *8*, 035030.

(65) Lin, M. L.; Tan, Q. H.; Wu, J. B.; Chen, X. S.; Wang, J. H.; Pan, Y. H.; Zhang, X.; Cong, X.; Zhang, J.; Ji, W.; et al. Moiré Phonons in Twisted Bilayer MoS2. *ACS Nano* **2018**, *12*, 8770−8780.

(66) Lin, K. Q.; Holler, J.; Bauer, J. M.; Parzefall, P.; Scheuck, M.; Peng, B.; Korn, T.; Bange, S.; Lupton, J. M.; Schüller, C. Large-Scale Mapping of Moiré Superlattices by Hyperspectral Raman Imaging. *Adv. Mater.* **2021**, *33*, 2008333.

(67) Lui, C. H.; Li, Z.; Chen, Z.; Klimov, P. V.; Brus, L. E.; Heinz, T. F. Imaging Stacking Order in Few-Layer Graphene. *Nano Lett.* **2011**, *11*, 164−169.

(68) Cong, C.; Yu, T.; Sato, K.; Shang, J.; Saito, R.; Dresselhaus, G. F.; Dresselhaus, M. S. Raman Characterization of ABA- and ABC-Stacked Trilayer Graphene. *ACS Nano* **2011**, *5*, 8760−8768.

(69) Shinde, S. M.; Dhakal, K. P.; Chen, X.; Yun, W. S.; Lee, J.; Kim, H.; Ahn, J. H. Stacking-Controllable Interlayer Coupling and Symmetric Configuration of Multilayered Mos2. *NPG Asia Mater.* **2018**, *10*, e468.

(70) Xia, M.; Li, B.; Yin, K.; Capellini, G.; Niu, G.; Gong, Y.; Zhou, W.; Ajayan, P. M.; Xie, Y. H. Spectroscopic Signatures of AA' and AB Stacking of Chemical Vapor Deposited Bilayer MoS2. *ACS Nano* **2015**, *9*, 12246−12254.

(71) Shen, Y. R. Surface Properties Probed by Second-Harmonic and Sum-Frequency Generation. *Nature* **1989**, *337*, 519−525.

(72) Wang, Y.; Xiao, J.; Yang, S.; Wang, Y.; Zhang, X. Second Harmonic Generation Spectroscopy on Two-Dimensional Materials [Invited]. *Opt. Mater. Express* **2019**, *9*, 1136−1149.

(73) Li, Y.; Rao, Y.; Mak, K. F.; You, Y.; Wang, S.; Dean, C. R.; Heinz, T. F. Probing Symmetry Properties of Few-Layer MoS2 and h-BN by Optical Second-Harmonic Generation. *Nano Lett.* **2013**, *13*, 3329−3333.

(74) Shan, Y.; Li, Y.; Huang, D.; Tong, Q.; Yao, W.; Liu, W.-T.; Wu, S. Stacking Symmetry Governed Second Harmonic Generation in Graphene Trilayers. *Sci. Adv.* **2018**, *4*, No. eaat0074.

(75) Sun, Z.; Yi, Y.; Song, T.; Clark, G.; Huang, B.; Shan, Y.; Wu, S.; Huang, D.; Gao, C.; Chen, Z.; et al. Giant Nonreciprocal Second-Harmonic Generation from Antiferromagnetic Bilayer CrI3. *Nature* **2019**, *572*, 497−501.

(76) Lee, K.; Dismukes, A. H.; Telford, E. J.; Wiscons, R. A.; Wang, J.; Xu, X.; Nuckolls, C.; Dean, C. R.; Roy, X.; Zhu, X. Magnetic Order and Symmetry in the 2D Semiconductor CrSBr. *Nano Lett.* **2021**, *21*, 3511−3517.

(77) Cha, S.; Lee, G.; Lee, S.; Ryu, S. H.; Sohn, Y.; An, G.; Kang, C.; Kim, M.; Kim, K.; Soon, A.; et al. Order-Disorder Phase Transition Driven by Interlayer Sliding in Lead Iodides. *Nat. Commun.* **2023**, *14*, 1981.

(78) Hovden, R.; Liu, P.; Schnitzer, N.; Tsen, A. W.; Liu, Y.; Lu, W.; Sun, Y.; Kourkoutis, L. F. Thickness and Stacking Sequence Determination of Exfoliated Dichalcogenides (1T-TaS 2, 2H-MoS 2) Using Scanning Transmission Electron Microscopy. *Microsc. Microanal.* **2018**, *24*, 387−395.

(79) Nalin Mehta, A.; Gauquelin, N.; Nord, M.; Orekhov, A.; Bender, H.; Cerbu, D.; Verbeeck, J.; Vandervorst, W. Unravelling Stacking Order in Epitaxial Bilayer MX2using 4D-STEM with Unsupervised Learning. *Nanotechnology* **2020**, *31*, 445702.

(80) Hart, J. L.; Bhatt, L.; Zhu, Y.; Han, M. G.; Bianco, E.; Li, S.; Hynek, D. J.; Schneeloch, J. A.; Tao, Y.; Louca, D.; et al. Emergent Layer Stacking Arrangements in C-Axis Confined MoTe2. *Nat. Commun.* **2023**, *14*, 4803.

(81) Sung, S. H.; Schnitzer, N.; Brown, L.; Park, J.; Hovden, R. Stacking, Strain, and Twist in 2D Materials Quantified by 3D Electron Diffraction. *Phys. Rev. Mater.* **2019**, *3*, 064003.

(82) Sie, E. J.; Nyby, C. M.; Pemmaraju, C. D.; Park, S. J.; Shen, X.; Yang, J.; Hoffmann, M. C.; Ofori-Okai, B. K.; Li, R.; Reid, A. H.; et al. An Ultrafast Symmetry Switch in a Weyl Semimetal. *Nature* **2019**, *565*, 61−66.

(83) Ji, S.; Grånäs, O.; Weissenrieder, J. Manipulation of Stacking Order in Td-WTe2 by Ultrafast Optical Excitation. *ACS Nano* **2021**, *15*, 8826−8835.

(84) Sui, F.; Jin, M.; Zhang, Y.; Qi, R.; Wu, Y. N.; Huang, R.; Yue, F.; Chu, J. Sliding Ferroelectricity in van Der Waals Layered γ-InSe Semiconductor. *Nat. Commun.* **2023**, *14*, 36.

(85) Oviedo, J. P.; Kc, S.; Lu, N.; Wang, J.; Cho, K.; Wallace, R. M.; Kim, M. J. In Situ TEM Characterization of Shear-Stress-Induced Interlayer Sliding in the Cross Section View of Molybdenum Disulfide. *ACS Nano* **2015**, *9*, 1543−1551.

(86) Jiang, L.; Wang, S.; Shi, Z.; Jin, C.; Utama, M. I. B.; Zhao, S.; Shen, Y. R.; Gao, H. J.; Zhang, G.; Wang, F. Manipulation of Domain-Wall Solitons in Bi- and Trilayer Graphene. *Nat. Nanotechnol.* **2018**, *13*, 204−208.

(87) Kim, D. S.; Kwon, H.; Nikitin, A. Y.; Ahn, S.; Martín-Moreno, L.; García-Vidal, F. J.; Ryu, S.; Min, H.; Kim, Z. H. Stacking Structures of Few-Layer Graphene Revealed by Phase-Sensitive Infrared Nanoscopy. *ACS Nano* **2015**, *9*, 6765−6773.

(88) Luan, Y.; Qian, J.; Kim, M.; Ho, K. M.; Shi, Y.; Li, Y.; Wang, C. Z.; Tringides, M. C.; Fei, Z. Imaging Stacking-Dependent Surface Plasmon Polaritons in Trilayer Graphene. *Phys. Rev. Appl.* **2022**, *18*, 024052.

(89) Shen, P.; Zhou, X.; Chen, J.; Deng, A.; Lyu, B.; Zhang, Z.; Lou, S.; Ma, S.; Wei, B.; Shi, Z. Quick Identification of ABC Trilayer Graphene at Nanoscale Resolution via a Near-Field Optical Route. *Mater. Futures* **2023**, *2*, 015301.

(90) Jeong, G.; Choi, B.; Kim, D. S.; Ahn, S.; Park, B.; Kang, J. H.; Min, H.; Hong, B. H.; Kim, Z. H. Mapping of Bernal and Non-Bernal Stacking Domains in Bilayer Graphene Using Infrared Nanoscopy. *Nanoscale* **2017**, *9*, 4191−4195.

(91) Wu, H.; Yu, X.; Zhu, M.; Zhu, Z.; Zhang, J.; Zhang, S.; Qin, S.; Wang, G.; Peng, G.; Dai, J.; Novoselov, K. S. Direct Visualization and Manipulation of Stacking Orders in Few-Layer Graphene by Dynamic Atomic Force Microscopy. *J. Phys. Chem. Lett.* **2021**, *12*, 7328−7334.

(92) Wu, H.; Yu, X.; Zhu, M.; Zhu, Z.; Zhang, J.; Zhang, S.; Qin, S.; Wang, G.; Peng, G.; Dai, J.; et al. Direct Visualization and Manipulation of Stacking Orders in Few-Layer Graphene by Dynamic Atomic Force Microscopy. *J. Phys. Chem. Lett.* **2021**, *12*, 7328−7334.

(93) Tagantsev, A. K.; Vaideeswaran, K.; Vakhrushev, S. B.; Filimonov, A. V.; Burkovsky, R. G.; Shaganov, A.; Andronikova, D.; Rudskoy, A. I.; Baron, A. Q. R.; Uchiyama, H.; et al. The Origin of Antiferroelectricity in PbZrO3. *Nat. Commun.* **2013**, *4*, 2229.

(94) Zheng, C.; Yu, L.; Zhu, L.; Collins, J. L.; Kim, D.; Lou, Y.; Xu, C.; Li, M.; Wei, Z.; Zhang, Y.; Edmonds, M. T.; Li, S.; Seidel, J.; Zhu, Y.; Liu, J. Z.; Tang, W.-X.; Fuhrer, M. S. Room Temperature In-Plane Ferroelectricity in van Der Waals In 2Se3. *Sci. Adv.* **2018**, *4*, No. eaar7720.

(95) Ding, W.; Zhu, J.; Wang, Z.; Gao, Y.; Xiao, D.; Gu, Y.; Zhang, Z.; Zhu, W. Prediction of Intrinsic Two-Dimensional Ferroelectrics in In 2 Se 3 and Other III 2 -VI 3 van Der Waals Materials. *Nat. Commun.* **2017**, *8*, 14956.

(96) Wang, C.; You, L.; Cobden, D.; Wang, J. Towards Two-Dimensional van Der Waals Ferroelectrics. *Nat. Mater.* **2023**, *22*, 542−552.

(97) Meng, P.; Wu, Y.; Bian, R.; Pan, E.; Dong, B.; Zhao, X.; Chen, J.; Wu, L.; Sun, Y.; Fu, Q.; et al. Sliding Induced Multiple Polarization States in Two-Dimensional Ferroelectrics. *Nat. Commun.* **2022**, *13*, 7696.

(98) Xiao, R.-C.; Gao, Y.; Jiang, H.; Gan, W.; Zhang, C.; Li, H. Non-Synchronous Bulk Photovoltaic Effect in Two-Dimensional Interlayer-Sliding Ferroelectrics. *NPJ. Comput. Mater.* **2022**, *8*, 138.

(99) Gruverman, A.; Alexe, M.; Meier, D. Piezoresponse Force Microscopy and Nanoferroic Phenomena. *Nat. Commun.* **2019**, *10*, 1661.

(100) Sharma, P.; Xiang, F.-X.; Shao, D.-F.; Zhang, D.; Tsymbal, E. Y.; Hamilton, A. R.; Seidel, J. A Room-Temperature Ferroelectric Semimetal. *Sci. Adv.* **2019**, *5*, No. eaax5080.

(101) Brennan, C. J.; Ghosh, R.; Koul, K.; Banerjee, S. K.; Lu, N.; Yu, E. T. Out-of-Plane Electromechanical Response of Monolayer

Molybdenum Disulfide Measured by Piezoresponse Force Microscopy. *Nano Lett.* **2017**, *17*, 5464−5471.

(102) Yarajena, S. S.; Biswas, R.; Raghunathan, V.; Naik, A. K. Quantitative Probe for In-Plane Piezoelectric Coupling in 2D Materials. *Sci. Rep.* **2021**, *11* (1), No. 7066.

(103) Melitz, W.; Shen, J.; Kummel, A. C.; Lee, S. Kelvin Probe Force Microscopy and Its Application. *Surface Science Reports* **2011**, *66*, 1−27.

(104) Vizner Stern, M.; Waschitz, Y.; Cao, W.; Nevo, I.; Watanabe, K.; Taniguchi, T.; Sela, E.; Urbakh, M.; Hod, O.; Ben Shalom, M. Interfacial Ferroelectricity by van Der Waals Sliding. *Science* **2021**, *372*, 1462−1464.

(105) Henkelman, G.; Uberuaga, B. P.; Jónsson, H. Climbing Image Nudged Elastic Band Method for Finding Saddle Points and Minimum Energy Paths. *J. Chem. Phys.* **2000**, *113*, 9901−9904.

(106) Zhong, T.; Cheng, L.; Ren, Y.; Wu, M. Theoretical Studies of Sliding Ferroelectricity, Magnetoelectric Couplings, and Piezo-Multiferroicity in Two-Dimensional Magnetic Materials. *Chem. Phys. Lett.* **2023**, *818*, 140430.

(107) Liu, M.; Ji, H.; Fu, Z.; Wang, Y.; Sun, J. T.; Gao, H. J. Orbital Distortion and Electric Field Control of Sliding Ferroelectricity in a Boron Nitride Bilayer. *J. Phys.: Condens. Matter* **2023**, *35*, 235001.

(108) Shi, S.; Hao, K. R.; Ma, X. Y.; Yan, Q. B.; Su, G. Controllable Spin Splitting in 2D Ferroelectric Few-Layer γ-GeSe. *J. Phys.: Condens. Matter* **2023**, *35*, 385501.

(109) Liu, X.; Pyatakov, A. P.; Ren, W. Magnetoelectric Coupling in Multiferroic Bilayer VS2. *Phys. Rev. Lett.* **2020**, *125*, 247601.

(110) Ren, Y.; Ke, S.; Lou, W. K.; Chang, K. Quantum Phase Transitions Driven by Sliding in Bilayer MnBi2Te4. *Phys. Rev. B* **2022**, *106*, 235302.

(111) Wang, Z.; Gui, Z.; Huang, L. Sliding Ferroelectricity in Bilayer Honeycomb Structures: A First-Principles Study. *Phys. Rev. B* **2023**, *107*, 035426.

(112) Liu, K.; Ma, X.; Xu, S.; Li, Y.; Zhao, M. Tunable Sliding Ferroelectricity and Magnetoelectric Coupling in Two-Dimensional Multiferroic MnSe Materials. *NPJ. Comput. Mater.* **2023**, *9*, 16.

(113) Xiao, J.; Wang, Y.; Wang, H.; Pemmaraju, C. D.; Wang, S.; Muscher, P.; Sie, E. J.; Nyby, C. M.; Devereaux, T. P.; Qian, X.; et al. Berry Curvature Memory through Electrically Driven Stacking Transitions. *Nat. Phys.* **2020**, *16*, 1028−1034.

(114) Yasuda, K.; Wang, X.; Watanabe, K.; Taniguchi, T.; Jarillo-Herrero, P. Stacking-Engineered Ferroelectricity in Bilayer Boron Nitride. *Science* **2021**, *372*, 1458−1462.

(115) Woods, C. R.; Ares, P.; Nevison-Andrews, H.; Holwill, M. J.; Fabregas, R.; Guinea, F.; Geim, A. K.; Novoselov, K. S.; Walet, N. R.; Fumagalli, L. Charge-Polarized Interfacial Superlattices in Marginally Twisted Hexagonal Boron Nitride. *Nat. Commun.* **2021**, *12*, 347.

(116) Li, H.; Utama, M. I. B.; Wang, S.; Zhao, W.; Zhao, S.; Xiao, X.; Jiang, Y.; Jiang, L.; Taniguchi, T.; Watanabe, K.; et al. Global Control of Stacking-Order Phase Transition by Doping and Electric Field in Few-Layer Graphene. *Nano Lett.* **2020**, *20*, 3106−3112.

(117) Deb, S.; Cao, W.; Raab, N.; Watanabe, K.; Taniguchi, T.; Goldstein, M.; Kronik, L.; Urbakh, M.; Hod, O.; Ben Shalom, M. Cumulative Polarization in Conductive Interfacial Ferroelectrics. *Nature* **2022**, *612*, 465−469.

(118) Zheng, Z.; Ma, Q.; Bi, Z.; de la Barrera, S.; Liu, M. H.; Mao, N.; Zhang, Y.; Kiper, N.; Watanabe, K.; Taniguchi, T.; et al. Unconventional Ferroelectricity in Moiré Heterostructures. *Nature* **2020**, *588*, 71−76.

(119) Niu, R.; Li, Z.; Han, X.; Qu, Z.; Ding, D.; Wang, Z.; Liu, Q.; Liu, T.; Han, C.; Watanabe, K.; et al. Giant Ferroelectric Polarization in a Bilayer Graphene Heterostructure. *Nat. Commun.* **2022**, *13*, 6241.

(120) Yang, L.; Wu, M. Across-Layer Sliding Ferroelectricity in 2D Heterolayers. *Adv. Funct. Mater.* **2023**, *33*, 2301105.

(121) Zhang, M. Y.; Wang, Z. X.; Li, Y. N.; Shi, L. Y.; Wu, D.; Lin, T.; Zhang, S. J.; Liu, Y. Q.; Liu, Q. M.; Wang, J.; et al. Light-Induced Subpicosecond Lattice Symmetry Switch in MoTe2. *Phys. Rev. X.* **2019**, *9*, 021036.

(122) Park, J.; Yeu, I. W.; Han, G.; Hwang, C. S.; Choi, J. H. Ferroelectric Switching in Bilayer 3R MoS2 via Interlayer Shear Mode Driven by Nonlinear Phononics. *Sci. Rep.* **2019**, *9*, 14919.

(123) Ji, Z.; Hong, H.; Zhang, J.; Zhang, Q.; Huang, W.; Cao, T.; Qiao, R.; Liu, C.; Liang, J.; Jin, C.; et al. Robust Stacking-Independent Ultrafast Charge Transfer in MoS2/WS2 Bilayers. *ACS Nano* **2017**, *11*, 12020−12026.

(124) Rajapakse, M.; Karki, B.; Abu, U. O.; Pishgar, S.; Musa, M. R. K.; Riyadh, S. M. S.; Yu, M.; Sumanasekera, G.; Jasinski, J. B. Intercalation as a Versatile Tool for Fabrication, Property Tuning, and Phase Transitions in 2D Materials. *npj 2D Mater. Appl.* **2021**, *5*, 30.

(125) Muscher, P. K.; Rehn, D. A.; Sood, A.; Lim, K.; Luo, D.; Shen, X.; Zajac, M.; Lu, F.; Mehta, A.; Li, Y.; et al. Highly Efficient Uniaxial In-Plane Stretching of a 2D Material via Ion Insertion. *Adv. Mater.* **2021**, *33*, 2101875.

(126) Wang, M.; Kumar, A.; Dong, H.; Woods, J. M.; Pondick, J. V.; Xu, S.; Hynek, D. J.; Guo, P.; Qiu, D. Y.; Cha, J. J. A Gapped Phase in Semimetallic Td-WTe2 Induced by Lithium Intercalation. *Adv. Mater.* **2022**, *34*, 2200861.

(127) Tang, W.; Sanville, E.; Henkelman, G. A Grid-Based Bader Analysis Algorithm without Lattice Bias. *J. Phys.: Condens. Matter* **2009**, *21*, 084204.

(128) Liao, M.; Nicolini, P.; Du, L.; Yuan, J.; Wang, S.; Yu, H.; Tang, J.; Cheng, P.; Watanabe, K.; Taniguchi, T.; et al. UItra-Low Friction and Edge-Pinning Effect in Large-Lattice-Mismatch van Der Waals Heterostructures. *Nat. Mater.* **2022**, *21*, 47−53.

(129) Yu, H.; Yang, Z.; Du, L.; Zhang, J.; Shi, J.; Chen, W.; Chen, P.; Liao, M.; Zhao, J.; Meng, J.; et al. Precisely Aligned Monolayer MoS2 Epitaxially Grown on H-BN Basal Plane. *Small* **2017**, *13*, 1603005.

(130) Wang, D.; Chen, G.; Li, C.; Cheng, M.; Yang, W.; Wu, S.; Xie, G.; Zhang, J.; Zhao, J.; Lu, X.; et al. Thermally Induced Graphene Rotation on Hexagonal Boron Nitride. *Phys. Rev. Lett.* **2016**, *116*, 126101.

(131) Li, T.; Jiang, S.; Sivadas, N.; Wang, Z.; Xu, Y.; Weber, D.; Goldberger, J. E.; Watanabe, K.; Taniguchi, T.; Fennie, C. J.; et al. Pressure-Controlled Interlayer Magnetism in Atomically Thin CrI3. *Nat. Mater.* **2019**, *18*, 1303−1308.

(132) Song, T.; Fei, Z.; Yankowitz, M.; Lin, Z.; Jiang, Q.; Hwangbo, K.; Zhang, Q.; Sun, B.; Taniguchi, T.; Watanabe, K. Switching 2D Magnetic States via Pressure Tuning of Layer Stacking. *Nat. Mater.* **2019**, *18*, 1298−1302.

(133) Sivadas, N.; Okamoto, S.; Xu, X.; Fennie, C. J.; Xiao, D. Stacking-Dependent Magnetism in Bilayer CrI 3. *Nano Lett.* **2018**, *18*, 7658−7664.

(134) Jiang, P.; Wang, C.; Chen, D.; Zhong, Z.; Yuan, Z.; Lu, Z. Y.; Ji, W. Stacking Tunable Interlayer Magnetism in Bilayer CrI3. *Phys. Rev. B* **2019**, *99*, 144401.

(135) Jang, S. W.; Jeong, M. Y.; Yoon, H.; Ryee, S.; Han, M. J. Microscopic Understanding of Magnetic Interactions in Bilayer CrI3. *Phys. Rev. Mater.* **2019**, *3*, No. 031001(R).

(136) Kong, X.; Yoon, H.; Han, M. J.; Liang, L. Switching Interlayer Magnetic Order in Bilayer CrI3by Stacking Reversal. *Nanoscale* **2021**, *13*, 16172−16181.

(137) He, Z.; Dou, K.; Du, W.; Dai, Y.; Huang, B.; Ma, Y. Multiple Topological Magnetism in van Der Waals Heterostructure of MnTe2/ZrS2. *Nano Lett.* **2023**, *23*, 312−318.

(138) Takahashi, R.; Nagaosa, N. Berry Curvature in Magnon-Phonon Hybrid Systems. *Phys. Rev. Lett.* **2016**, *117*, 217205.

(139) Go, G.; Kim, S. K.; Lee, K. J. Topological Magnon-Phonon Hybrid Excitations in Two-Dimensional Ferromagnets with Tunable Chern Numbers. *Phys. Rev. Lett.* **2019**, *123*, 237207.

(140) Zhang, S.; Go, G.; Lee, K. J.; Kim, S. K. SU(3) Topology of Magnon-Phonon Hybridization in 2D Antiferromagnets. *Phys. Rev. Lett.* **2020**, *124*, 147204.

(141) Hakelberg, F.; Kiefer, P.; Wittemer, M.; Warring, U.; Schaetz, T. Interference in a Prototype of a Two-Dimensional Ion Trap Array Quantum Simulator. *Phys. Rev. Lett.* **2019**, *123*, 100504.

(142) Zhang, J.; Pagano, G.; Hess, P. W.; Kyprianidis, A.; Becker, P.; Kaplan, H.; Gorshkov, A. V.; Gong, Z. X.; Monroe, C. Observation of

a Many-Body Dynamical Phase Transition with a 53-Qubit Quantum Simulator. *Nature* **2017**, *551*, 601−604.

(143) Altman, E.; Brown, K. R.; Carleo, G.; Carr, L. D.; Demler, E.; Chin, C.; Demarco, B.; Economou, S. E.; Eriksson, M. A.; Fu, K. M. C.; et al. Quantum Simulators: Architectures and Opportunities. *PRX Quantum* **2021**, *2*, 017003.

(144) Yan, B.; Moses, S. A.; Gadway, B.; Covey, J. P.; Hazzard, K. R. A.; Rey, A. M.; Jin, D. S.; Ye, J. Observation of Dipolar Spin-Exchange Interactions with Lattice-Confined Polar Molecules. *Nature* **2013**, *501*, 521−525.

(145) Hazzard, K. R. A.; Gadway, B.; Foss-Feig, M.; Yan, B.; Moses, S. A.; Covey, J. P.; Yao, N. Y.; Lukin, M. D.; Ye, J.; Jin, D. S.; et al. Many-Body Dynamics of Dipolar Molecules in an Optical Lattice. *Phys. Rev. Lett.* **2014**, *113*, 195302.

(146) Baier, S.; Mark, M. J.; Petter, D.; Aikawa, K.; Chomaz, L.; Cai, Z.; Baranov, M.; Zoller, P.; Ferlaino, F. Extended Bose-Hubbard Models with Ultracold Magnetic Atoms. *Science* **2016**, *352*, 201−205.

(147) Jindal, A.; Saha, A.; Li, Z.; Taniguchi, T.; Watanabe, K.; Hone, J. C.; Birol, T.; Fernandes, R. M.; Dean, C. R.; Pasupathy, A. N.; et al. Coupled Ferroelectricity and Superconductivity in Bilayer Td-MoTe2. *Nature* **2023**, *613*, 48−52.

(148) Klein, D. R.; Xia, L. Q.; MacNeill, D.; Watanabe, K.; Taniguchi, T.; Jarillo-Herrero, P. Electrical Switching of a Bistable Moiré Superconductor. *Nat. Nanotechnol.* **2023**, *18*, 331−335.

(149) Rodan-Legrain, D.; Cao, Y.; Park, J. M.; de la Barrera, S. C.; Randeria, M. T.; Watanabe, K.; Taniguchi, T.; Jarillo-Herrero, P. Highly Tunable Junctions and Non-Local Josephson Effect in Magic-Angle Graphene Tunnelling Devices. *Nat. Nanotechnol.* **2021**, *16*, 769−775.

(150) de Vries, F. K.; Portolés, E.; Zheng, G.; Taniguchi, T.; Watanabe, K.; Ihn, T.; Ensslin, K.; Rickhaus, P. Gate-Defined Josephson Junctions in Magic-Angle Twisted Bilayer Graphene. *Nat. Nanotechnol.* **2021**, *16*, 760−763.

(151) Díez-Mérida, J.; Díez-Carlón, A.; Yang, S. Y.; Xie, Y. M.; Gao, X. J.; Senior, J.; Watanabe, K.; Taniguchi, T.; Lu, X.; Higginbotham, A. P.; et al. Symmetry-Broken Josephson Junctions and Superconducting Diodes in Magic-Angle Twisted Bilayer Graphene. *Nat. Commun.* **2023**, *14*, 2396.

(152) Portolés, E.; Iwakiri, S.; Zheng, G.; Rickhaus, P.; Taniguchi, T.; Watanabe, K.; Ihn, T.; Ensslin, K.; de Vries, F. K. A Tunable Monolithic SQUID in Twisted Bilayer Graphene. *Nat. Nanotechnol.* **2022**, *17*, 1159−1164.

(153) Enaldiev, V. V.; Ferreira, F.; Magorrian, S. J.; Fal'ko, V. I. Piezoelectric Networks and Ferroelectric Domains in Twistronic Superlattices in WS2/MoS2 and WSe2/MoSe2 Bilayers. *2D Mater.* **2021**, *8*, 025030.

(154) Yoo, H.; Engelke, R.; Carr, S.; Fang, S.; Zhang, K.; Cazeaux, P.; Sung, S. H.; Hovden, R.; Tsen, A. W.; Taniguchi, T.; et al. Atomic and Electronic Reconstruction at the van Der Waals Interface in Twisted Bilayer Graphene. *Nat. Mater.* **2019**, *18*, 448−453.

(155) Wang, P.; Yu, G.; Kwan, Y. H.; Jia, Y.; Lei, S.; Klemenz, S.; Cevallos, F. A.; Singha, R.; Devakul, T.; Watanabe, K.; et al. One-Dimensional Luttinger Liquids in a Two-Dimensional Moiré Lattice. *Nature* **2022**, *605*, 57−62.

(156) Regan, E. C.; Wang, D.; Jin, C.; Bakti Utama, M. I.; Gao, B.; Wei, X.; Zhao, S.; Zhao, W.; Zhang, Z.; Yumigeta, K.; et al. Mott and Generalized Wigner Crystal States in WSe2/WS2Moiré Superlattices. *Nature* **2020**, *579*, 359−363.

(157) Zhou, Y.; Sung, J.; Brutschea, E.; Esterlis, I.; Wang, Y.; Scuri, G.; Gelly, R. J.; Heo, H.; Taniguchi, T.; Watanabe, K.; et al. Bilayer Wigner Crystals in a Transition Metal Dichalcogenide Heterostructure. *Nature* **2021**, *595*, 48−52.

(158) Li, H.; Li, S.; Regan, E. C.; Wang, D.; Zhao, W.; Kahn, S.; Yumigeta, K.; Blei, M.; Taniguchi, T.; Watanabe, K.; et al. Imaging Two-Dimensional Generalized Wigner Crystals. *Nature* **2021**, *597*, 650−654.

(159) Kennes, D. M.; Claassen, M.; Xian, L.; Georges, A.; Millis, A. J.; Hone, J.; Dean, C. R.; Basov, D. N.; Pasupathy, A. N.; Rubio, A. Moiré Heterostructures as a Condensed-Matter Quantum Simulator. *Nat. Phys.* **2021**, *17*, 155−163.

(160) Mak, K. F.; Shan, J. Semiconductor Moiré Materials. *Nat. Nanotechnol.* **2022**, *17*, 686−695.

(161) Lau, C. N.; Bockrath, M. W.; Mak, K. F.; Zhang, F. Reproducibility in the Fabrication and Physics of Moiré Materials. *Nature.* **2022**, *602*, 41−50.

(162) Liu, C.; Li, Z.; Qiao, R.; Wang, Q.; Zhang, Z.; Liu, F.; Zhou, Z.; Shang, N.; Fang, H.; Wang, M.; et al. Designed Growth of Large Bilayer Graphene with Arbitrary Twist Angles. *Nat. Mater.* **2022**, *21*, 1263−1268.

(163) Sun, L.; Wang, Z.; Wang, Y.; Zhao, L.; Li, Y.; Chen, B.; Huang, S.; Zhang, S.; Wang, W.; Pei, D.; et al. Hetero-Site Nucleation for Growing Twisted Bilayer Graphene with a Wide Range of Twist Angles. *Nat. Commun.* **2021**, *12*, 2391.

(164) Deng, B.; Wang, B.; Li, N.; Li, R.; Wang, Y.; Tang, J.; Fu, Q.; Tian, Z.; Gao, P.; Xue, J.; Peng, H. Interlayer Decoupling in 30° Twisted Bilayer Graphene Quasicrystal. *ACS Nano* **2020**, *14*, 1656−1664.

(165) Yan, Z.; Liu, Y.; Ju, L.; Peng, Z.; Lin, J.; Wang, G.; Zhou, H.; Xiang, C.; Samuel, E. L. G.; Kittrell, C.; et al. Large Hexagonal Bi- and Trilayer Graphene Single Crystals with Varied Interlayer Rotations. *Angewandte Chemie - International Edition* **2014**, *53*, 1565−1569.

(166) Lu, C. C.; Lin, Y. C.; Liu, Z.; Yeh, C. H.; Suenaga, K.; Chiu, P. W. Twisting Bilayer Graphene Superlattices. *ACS Nano* **2013**, *7*, 2587−2594.

(167) Liu, L.; Zhou, H.; Cheng, R.; Yu, W. J.; Liu, Y.; Chen, Y.; Shaw, J.; Zhong, X.; Huang, Y.; Duan, X. High-Yield Chemical Vapor Deposition Growth of High-Quality Large-Area AB-Stacked Bilayer Graphene. *ACS Nano* **2012**, *6*, 8241−8249.

(168) Brown, L.; Hovden, R.; Huang, P.; Wojcik, M.; Muller, D. A.; Park, J. Twinning and Twisting of Tri- and Bilayer Graphene. *Nano Lett.* **2012**, *12*, 1609−1615.

(169) Khalil, L.; Pierucci, D.; Velez-Fort, E.; Avila, J.; Vergnaud, C.; Dudin, P.; Oehler, F.; Chaste, J.; Jamet, M.; Lhuillier, E.; et al. Hybridization and Localized Flat Band in the WSe2/MoSe2 Heterobilayer. *Nanotechnology* **2023**, *34*, 045702.

(170) Pham, T. T.; Vancsó, P.; Szendrő, M.; Palotás, K.; Castelino, R.; Bouatou, M.; Chacon, C.; Henrard, L.; Lagoute, J.; Sporken, R. Higher-Indexed Moiré Patterns and Surface States of MoTe2/Graphene Heterostructure Grown by Molecular Beam Epitaxy. *NPJ. 2D Mater. Appl.* **2022**, *6*, 48.

(171) Lu, H.; Liu, W.; Wang, H.; Liu, X.; Zhang, Y.; Yang, D.; Pi, X. Molecular Beam Epitaxy Growth and Scanning Tunneling Microscopy Study of 2D Layered Materials on Epitaxial Graphene/Silicon Carbide. *Nanotechnology* **2023**, *34*, 132001.

(172) Castelino, R.; Pham, T. T.; Felten, A.; Sporken, R. Substrate Temperature Dependence of the Crystalline Quality for the Synthesis of Pure-Phase MoTe2 on Graphene/6H-SiC(0001) by Molecular Beam Epitaxy. *Nanotechnology* **2020**, *31*, 115702.

(173) Choi, Y. H.; Lim, D. H.; Jeong, J. H.; Park, D.; Jeong, K. S.; Kim, M.; Song, A.; Chung, H. S.; Chung, K. B.; Yi, Y.; et al. Characterization of Rotational Stacking Layers in Large-Area MoSe2 Film Grown by Molecular Beam Epitaxy and Interaction with Photon. *ACS Appl. Mater. Interfaces* **2017**, *9*, 30786−30796.

(174) Fu, D.; Zhao, X.; Zhang, Y. Y.; Li, L.; Xu, H.; Jang, A. R.; Yoon, S. I.; Song, P.; Poh, S. M.; Ren, T.; et al. Molecular Beam Epitaxy of Highly Crystalline Monolayer Molybdenum Disulfide on Hexagonal Boron Nitride. *J. Am. Chem. Soc.* **2017**, *139*, 9392−9400.

(175) Jin, C.; Regan, E. C.; Yan, A.; Iqbal Bakti Utama, M.; Wang, D.; Zhao, S.; Qin, Y.; Yang, S.; Zheng, Z.; Shi, S.; et al. Observation of Moiré Excitons in WSe2/WS2 Heterostructure Superlattices. *Nature* **2019**, *567*, 76−80.

(176) Kennes, D. M.; Xian, L.; Claassen, M.; Rubio, A. One-Dimensional Flat Bands in Twisted Bilayer Germanium Selenide. *Nat. Commun.* **2020**, *11*, 1124.

(177) Li, Y.; Xue, M.; Fan, H.; Gao, C. F.; Shi, Y.; Liu, Y.; Watanabe, K.; Tanguchi, T.; Zhao, Y.; Wu, F.; et al. Symmetry Breaking and

Anomalous Conductivity in a Double-Moire Superlattice. *Nano Lett.* **2022**, *22*, 6215−6222.

(178) Alexeev, E. M.; Ruiz-Tijerina, D. A.; Danovich, M.; Hamer, M. J.; Terry, D. J.; Nayak, P. K.; Ahn, S.; Pak, S.; Lee, J.; Sohn, J. I.; et al. Resonantly Hybridized Excitons in Moiré Superlattices in van Der Waals Heterostructures. *Nature* **2019**, *567*, 81−86.

(179) Liu, E.; Barré, E.; van Baren, J.; Wilson, M.; Taniguchi, T.; Watanabe, K.; Cui, Y. T.; Gabor, N. M.; Heinz, T. F.; Chang, Y. C.; et al. Signatures of Moiré Trions in WSe2/MoSe2 Heterobilayers. *Nature* **2021**, *594*, 46−50.

(180) Xu, Y.; Liu, S.; Rhodes, D. A.; Watanabe, K.; Taniguchi, T.; Hone, J.; Elser, V.; Mak, K. F.; Shan, J. Correlated Insulating States at Fractional Fillings of Moiré Superlattices. *Nature* **2020**, *587*, 214−218.

(181) Balents, L.; Dean, C. R.; Efetov, D. K.; Young, A. F. Superconductivity and Strong Correlations in Moiré Flat Bands. *Nat. Phys.* **2020**, *16*, 725−733.

(182) Huang, D.; Choi, J.; Shih, C. K.; Li, X. Excitons in Semiconductor Moiré Superlattices. *Nat. Nanotechnol.* **2022**, *17*, 227−238.

(183) Wilson, N. P.; Yao, W.; Shan, J.; Xu, X. Excitons and Emergent Quantum Phenomena in Stacked 2D Semiconductors. *Nature.* **2021**, *599*, 383−392.

(184) Nagaosa, N.; Tokura, Y. Topological Properties and Dynamics of Magnetic Skyrmions. *Nat. Nanotechnol.* **2013**, *8*, 899−911.

(185) Fert, A.; Reyren, N.; Cros, V. Magnetic Skyrmions: Advances in Physics and Potential Applications. *Nat. Rev. Mater.* **2017**, *2*, 17031.

(186) Trier, F.; Noël, P.; Kim, J. V.; Attané, J. P.; Vila, L.; Bibes, M. Oxide Spin-Orbitronics: Spin-Charge Interconversion and Topological Spin Textures. *Nat. Rev. Mater.* **2022**, *7*, 258−274.

(187) Hejazi, K.; Luo, Z. X.; Balents, L. Heterobilayer Moiré Magnets: Moiré Skyrmions and Commensurate-Incommensurate Transitions. *Phys. Rev. B* **2021**, *104*, L100406.

(188) Hejazi, K.; Luo, Z.-X.; Balents, L. Noncollinear Phases in Moiré Magnets. *Proc. Natl. Acad. Sci. U.S.A.* **2020**, *117*, 10721−10726.

(189) Akram, M.; Erten, O. Skyrmions in Twisted van Der Waals Magnets. *Phys. Rev. B* **2021**, *103*, L140406.

(190) Akram, M.; Labollita, H.; Dey, D.; Kapeghian, J.; Erten, O.; Botana, A. S. Moiré Skyrmions and Chiral Magnetic Phases in Twisted CrX3(X = I, Br, and Cl) Bilayers. *Nano Lett.* **2021**, *21*, 6633−6639.

(191) Tong, Q.; Liu, F.; Xiao, J.; Yao, W. Skyrmions in the Moiré of van Der Waals 2D Magnets. *Nano Lett.* **2018**, *18*, 7194−7199.

(192) Cheng, G.; Rahman, M. M.; Allcca, A. L.; Rustagi, A.; Liu, X.; Liu, L.; Fu, L.; Zhu, Y.; Mao, Z.; Watanabe, K.; et al. Electrically Tunable Moiré Magnetism in Twisted Double Bilayers of Chromium Triiodide. *Nature Electronics* **2023**, *6*, 434−442.

(193) Xie, H.; Luo, X.; Ye, Z.; Sun, Z.; Ye, G.; Sung, S. H.; Ge, H.; Yan, S.; Fu, Y.; Tian, S.; et al. Evidence of Non-Collinear Spin Texture in Magnetic Moiré Superlattices. *Nat. Phys.* **2023**, *19*, 1150−1155.

(194) Xu, Y.; Ray, A.; Shao, Y. T.; Jiang, S.; Lee, K.; Weber, D.; Goldberger, J. E.; Watanabe, K.; Taniguchi, T.; Muller, D. A.; et al. Coexisting Ferromagnetic-Antiferromagnetic State in Twisted Bilayer CrI3. *Nat. Nanotechnol.* **2022**, *17*, 143−147.

(195) Song, T.; Sun, Q.-C.; Anderson, E.; Wang, C.; Qian, J.; Taniguchi, T.; Watanabe, K.; McGuire, M. A.; Stöhr, R.; Xiao, D.; et al. Direct Visualization of Magnetic Domains and Moiré Magnetism in Twisted 2D Magnets. *Science (1979)* **2021**, *374*, 1140−1144.

(196) Galbiati, M.; Zatko, V.; Godel, F.; Hirschauer, P.; Vecchiola, A.; Bouzehouane, K.; Collin, S.; Servet, B.; Cantarero, A.; Petroff, F.; et al. Very Long Term Stabilization of a 2D Magnet down to the Monolayer for Device Integration. *ACS Appl. Electron. Mater.* **2020**, *2*, 3508−3514.

(197) Gish, J. T.; Lebedev, D.; Stanev, T. K.; Jiang, S.; Georgopoulos, L.; Song, T. W.; Lim, G.; Garvey, E. S.; Valdman, L.; Balogun, O.; et al. Ambient-Stable Two-Dimensional CrI3via Organic-Inorganic Encapsulation. *ACS Nano* **2021**, *15*, 10659−10667.

(198) Haldane, F. D. M. "Luttinger Liquid Theory" of One-Dimensional Quantum Fluids. I. Properties of the Luttinger model and Their Extension to the General 1D Interacting Spinless Fermi Gas. *J. Phys. C. Solid State Phys.* **1981**, *14*, 2585−2609.

(199) Emery, V. J.; Fradkin, E.; Kivelson, S. A.; Lubensky, T. C. Quantum Theory of the Smectic Metal State in Stripe Phases. *Phys. Rev. Lett.* **2000**, *85*, 2160−2163.

(200) Vishwanath, A.; Carpentier, D. Two-Dimensional Anisotropic Non-Fermi-Liquid Phase of Coupled Luttinger Liquids. *Phys. Rev. Lett.* **2001**, *86*, 676−679.

(201) Mukhopadhyay, R.; Kane, C. L.; Lubensky, T. C. Sliding Luttinger Liquid Phases. *Phys. Rev. B* **2001**, *64*, 045120.

(202) Kane, C. L.; Mukhopadhyay, R.; Lubensky, T. C. Fractional Quantum Hall Effect in an Array of Quantum Wires. *Phys. Rev. Lett.* **2002**, *88*, 036401.

(203) Teo, J. C. Y.; Kane, C. L. From Luttinger Liquid to Non-Abelian Quantum Hall States. *Phys. Rev. B* **2014**, *89* (8), No. 085101.

(204) Tam, P. M.; Kane, C. L. Nondiagonal Anisotropic Quantum Hall States. *Phys. Rev. B* **2021**, *103*, 035142.

(205) Iadecola, T.; Neupert, T.; Chamon, C.; Mudry, C. Wire Constructions of Abelian Topological Phases in Three or More Dimensions. *Phys. Rev. B* **2016**, *93*, 195136.

(206) Meng, T.; Neupert, T.; Greiter, M.; Thomale, R. Coupled-Wire Construction of Chiral Spin Liquids. *Phys. Rev. B* **2015**, *91*, No. 241106(R).

(207) Patel, A. A.; Chowdhury, D. Two-Dimensional Spin Liquids with Z2 Topological Order in an Array of Quantum Wires. *Phys. Rev. B* **2016**, *94*, 195130.

(208) Chen, G.; Sharpe, A. L.; Fox, E. J.; Zhang, Y. H.; Wang, S.; Jiang, L.; Lyu, B.; Li, H.; Watanabe, K.; Taniguchi, T.; et al. Tunable Correlated Chern Insulator and Ferromagnetism in a Moiré Superlattice. *Nature* **2020**, *579*, 56−61.

(209) Liu, X.; Chiu, C. L.; Lee, J. Y.; Farahi, G.; Watanabe, K.; Taniguchi, T.; Vishwanath, A.; Yazdani, A. Spectroscopy of a Tunable Moiré System with a Correlated and Topological Flat Band. *Nat. Commun.* **2021**, *12*, 2732.

(210) Li, T.; Jiang, S.; Shen, B.; Zhang, Y.; Li, L.; Tao, Z.; Devakul, T.; Watanabe, K.; Taniguchi, T.; Fu, L.; et al. Quantum Anomalous Hall Effect from Intertwined Moiré Bands. *Nature* **2021**, *600*, 641−646.

(211) Chakraborty, A.; Das, K.; Sinha, S.; Adak, P. C.; Deshmukh, M. M.; Agarwal, A. Nonlinear Anomalous Hall Effects Probe Topological Phase-Transitions in Twisted Double Bilayer Graphene. *2d Mater.* **2022**, *9*, 045020.

(212) Andrews, B.; Soluyanov, A. Fractional Quantum Hall States for Moiré Superstructures in the Hofstadter Regime. *Phys. Rev. B* **2020**, *101*, 235312.

(213) Chittari, B. L.; Chen, G.; Zhang, Y.; Wang, F.; Jung, J. Gate-Tunable Topological Flat Bands in Trilayer Graphene Boron-Nitride Moiré Superlattices. *Phys. Rev. Lett.* **2019**, *122*, 016401.

(214) Zhang, Y.; Devakul, T.; Fu, L. Spin-Textured Chern Bands in AB-Stacked Transition Metal Dichalcogenide Bilayers. *Proc. Natl. Acad. Sci. U. S. A.* **2021**, *118*, No. e2112673118.

(215) Gou, J.; Kong, L.; He, X.; Huang, Y. L.; Sun, J.; Meng, S.; Wu, K.; Chen, L.; Wee, A. T. S. The Effect of Moiré Superstructures on Topological Edge States in Twisted Bismuthene Homojunctions. *Sci. Adv.* **2020**, *6*, No. eaba2773.

(216) Haavisto, M.; Lado, J. L.; Otero Fumega, A. Topological Multiferroic Order in Twisted Transition Metal Dichalcogenide Bilayers. *SciPost Physics* **2022**, *13*, 052.

(217) Lian, B.; Liu, Z.; Zhang, Y.; Wang, J. Flat Chern Band from Twisted Bilayer MnBi2Te4. *Phys. Rev. Lett.* **2020**, *124*, 126402.

(218) Kim, S.; Schwenk, J.; Walkup, D.; Zeng, Y.; Ghahari, F.; Le, S. T.; Slot, M. R.; Berwanger, J.; Blankenship, S. R.; Watanabe, K.; et al. Edge Channels of Broken-Symmetry Quantum Hall States in Graphene Visualized by Atomic Force Microscopy. *Nat. Commun.* **2021**, *12*, 2852.

(219) Polshyn, H.; Zhang, Y.; Kumar, M. A.; Soejima, T.; Ledwith, P.; Watanabe, K.; Taniguchi, T.; Vishwanath, A.; Zaletel, M. P.; Young, A. F. Topological Charge Density Waves at Half-Integer Filling of a Moiré Superlattice. *Nat. Phys.* **2022**, *18*, 42−47.

(220) Spanton, E. M.; Zibrov, A. A.; Zhou, H.; Taniguchi, T.; Watanabe, K.; Zaletel, M. P.; Young, A. F. Observation of Fractional Chern Insulators in a van Der Waals Heterostructure. *Science* **2018**, *360*, 62−66.

(221) Xie, Y.; Pierce, A. T.; Park, J. M.; Parker, D. E.; Khalaf, E.; Ledwith, P.; Cao, Y.; Lee, S. H.; Chen, S.; Forrester, P. R.; et al. Fractional Chern Insulators in Magic-Angle Twisted Bilayer Graphene. *Nature* **2021**, *600*, 439−443.

(222) Pierce, A. T.; Xie, Y.; Park, J. M.; Khalaf, E.; Lee, S. H.; Cao, Y.; Parker, D. E.; Forrester, P. R.; Chen, S.; Watanabe, K.; et al. Unconventional Sequence of Correlated Chern Insulators in Magic-Angle Twisted Bilayer Graphene. *Nat. Phys.* **2021**, *17*, 1210−1215.

(223) He, M.; Zhang, Y. H.; Li, Y.; Fei, Z.; Watanabe, K.; Taniguchi, T.; Xu, X.; Yankowitz, M. Competing Correlated States and Abundant Orbital Magnetism in Twisted Monolayer-Bilayer Graphene. *Nat. Commun.* **2021**, *12*, 4727.

(224) Sharpe, A. L.; Fox, E. J.; Barnard, A. W.; Finney, J.; Watanabe, K.; Taniguchi, T.; Kastner, M. A.; Goldhaber-Gordon, D. Emergent Ferromagnetism near Three-Quarters Filling in Twisted Bilayer Graphene. *Science* **2019**, *365*, 605−608.

(225) Serlin, M.; Tschirhart, C. L.; Polshyn, H.; Zhang, Y.; Zhu, J.; Watanabe, K.; Taniguchi, T.; Balents, L.; Young, A. F. Intrinsic Quantized Anomalous Hall Effect in a Moiré Heterostructure. *Science* **2020**, *367*, 900−903.

(226) Regnault, N.; Bernevig, B. A. Fractional Chern Insulator. *Phys. Rev. X.* **2011**, *1*, 021014.

(227) Neupert, T.; Santos, L.; Chamon, C.; Mudry, C. Fractional Quantum Hall States at Zero Magnetic Field. *Phys. Rev. Lett.* **2011**, *106*, 236804.

(228) Sheng, D. N.; Gu, Z. C.; Sun, K.; Sheng, L. Fractional Quantum Hall Effect in the Absence of Landau Levels. *Nat. Commun.* **2011**, *2*, 389.

(229) Li, H.; Kumar, U.; Sun, K.; Lin, S. Z. Spontaneous Fractional Chern Insulators in Transition Metal Dichalcogenide Moiré Superlattices. *Phys. Rev. Res.* **2021**, *3*, L032070.

(230) Wu, F.; Lovorn, T.; Tutuc, E.; Martin, I.; Macdonald, A. H. Topological Insulators in Twisted Transition Metal Dichalcogenide Homobilayers. *Phys. Rev. Lett.* **2019**, *122*, 086402.

(231) Devakul, T.; Crépel, V.; Zhang, Y.; Fu, L. Magic in Twisted Transition Metal Dichalcogenide Bilayers. *Nat. Commun.* **2021**, *12*, 6730.

(232) Yu, H.; Chen, M.; Yao, W. Giant Magnetic Field from Moiré Induced Berry Phase in Homobilayer Semiconductors. *Natl. Sci. Rev.* **2020**, *7*, 12−20.

(233) Crépel, V.; Fu, L. Anomalous Hall Metal and Fractional Chern Insulator in Twisted Transition Metal Dichalcogenides. *Phys. Rev. B* **2023**, *107*, L201109.

(234) Anderson, E.; Fan, F.-R.; Cai, J.; Holtzmann, W.; Taniguchi, T.; Watanabe, K.; Xiao, D.; Yao, W.; Xu, X. Programming Correlated Magnetic States with Gate-Controlled Moiré Geometry. *Science* **2023**, *381*, 325−33.

(235) Lin, J. X.; Siriviboon, P.; Scammell, H. D.; Liu, S.; Rhodes, D.; Watanabe, K.; Taniguchi, T.; Hone, J.; Scheurer, M. S.; Li, J. I. A. Zero-Field Superconducting Diode Effect in Small-Twist-Angle Trilayer Graphene. *Nat. Phys.* **2022**, *18*, 1221−1227.

(236) Halbertal, D.; Turkel, S.; Ciccarino, C. J.; Hauck, J. B.; Finney, N.; Hsieh, V.; Watanabe, K.; Taniguchi, T.; Hone, J.; Dean, C.; et al. Unconventional Non-Local Relaxation Dynamics in a Twisted Trilayer Graphene Moiré Superlattice. *Nat. Commun.* **2022**, *13*, 7587.

(237) Lu, X.; Stepanov, P.; Yang, W.; Xie, M.; Aamir, M. A.; Das, I.; Urgell, C.; Watanabe, K.; Taniguchi, T.; Zhang, G.; et al. Superconductors, Orbital Magnets and Correlated States in Magic-Angle Bilayer Graphene. *Nature* **2019**, *574*, 653−657.

(238) Waters, D.; Thompson, E.; Arreguin-Martinez, E.; Fujimoto, M.; Ren, Y.; Watanabe, K.; Taniguchi, T.; Cao, T.; Xiao, D.; Yankowitz, M. Mixed-Dimensional Moiré Systems of Twisted Graphitic Thin Films. *Nature* **2023**, *620*, 750−755.

(239) Uri, A.; de la Barrera, S. C.; Randeria, M. T.; Rodan-Legrain, D.; Devakul, T.; Crowley, P. J. D.; Paul, N.; Watanabe, K.; Taniguchi, T.; Lifshitz, R.; et al. Superconductivity and Strong Interactions in a Tunable Moiré Quasicrystal. *Nature* **2023**, *620*, 762−767.

(240) Koshino, M.; Oka, H. Topological Invariants in Two-Dimensional Quasicrystals. *Phys. Rev. Res.* **2022**, *4*, 013028.

(241) Tran, D. T.; Dauphin, A.; Goldman, N.; Gaspard, P. Topological Hofstadter Insulators in a Two-Dimensional Quasicrystal. *Phys. Rev. B* **2015**, *91*, 085125.

(242) Huang, H.; Liu, F. Quantum Spin Hall Effect and Spin Bott Index in a Quasicrystal Lattice. *Phys. Rev. Lett.* **2018**, *121*, 126401.

(243) Else, D. V.; Huang, S. J.; Prem, A.; Gromov, A. Quantum Many-Body Topology of Quasicrystals. *Phys. Rev. X.* **2021**, *11*, 041051.

(244) Sakai, S.; Takemori, N.; Koga, A.; Arita, R. Superconductivity on a Quasiperiodic Lattice: Extended-to-Localized Crossover of Cooper Pairs. *Phys. Rev. B* **2017**, *95*, 024509.

(245) Liu, Y. B.; Zhang, Y.; Chen, W. Q.; Yang, F. High-Angular-Momentum Topological Superconductivities in Twisted Bilayer Quasicrystal Systems. *Phys. Rev. B* **2023**, *107*, 014501.

(246) Kraus, Y. E.; Ringel, Z.; Zilberberg, O. Four-Dimensional Quantum Hall Effect in a Two-Dimensional Quasicrystal. *Phys. Rev. Lett.* **2013**, *111*, 226401.

(247) Kamiya, K.; Takeuchi, T.; Kabeya, N.; Wada, N.; Ishimasa, T.; Ochiai, A.; Deguchi, K.; Imura, K.; Sato, N. K. Discovery of Superconductivity in Quasicrystal. *Nat. Commun.* **2018**, *9*, 154.

(248) Deguchi, K.; Matsukawa, S.; Sato, N. K.; Hattori, T.; Ishida, K.; Takakura, H.; Ishimasa, T. Quantum Critical State in a Magnetic Quasicrystal. *Nat. Mater.* **2012**, *11*, 1013−1016.

(249) Dubois, J. M. Properties- and Applications of Quasicrystals and Complex Metallic Alloys. *Chem. Soc. Rev.* **2012**, *41*, 6760−6777.

(250) Mullan, C.; Slizovskiy, S.; Yin, J.; Wang, Z.; Yang, Q.; Xu, S.; Yang, Y.; Piot, B. A.; Hu, S.; Taniguchi, T.; et al. Mixing of Moiré-Surface and Bulk States in Graphite. *Nature* **2023**, *620*, 756−761.

(251) Karunadasa, H. I.; Montalvo, E.; Sun, Y.; Majda, M.; Long, J. R.; Chang, C. J. A Molecular MoS2 Edge Site Mimic for Catalytic Hydrogen Generation. *Science (1979)* **2012**, *335*, 698−702.

(252) González, J. R.; Alcántara, R.; Tirado, J. L.; Fielding, A. J.; Dryfe, R. A. W. Electrochemical Interaction of Few-Layer Molybdenum Disulfide Composites vs Sodium: New Insights on the Reaction Mechanism. *Chem. Mater.* **2017**, *29*, 5886−5895.

(253) Yu, Y.; Huang, S. Y.; Li, Y.; Steinmann, S. N.; Yang, W.; Cao, L. Layer-Dependent Electrocatalysis of MoS2 for Hydrogen Evolution. *Nano Lett.* **2014**, *14*, 553−558.

(254) Jiang, Z.; Zhou, W.; Hong, A.; Guo, M.; Luo, X.; Yuan, C. MoS2Moiré Superlattice for Hydrogen Evolution Reaction. *ACS Energy Lett.* **2019**, *4*, 2830−2835.

(255) Hsieh, V.; Halbertal, D.; Finney, N. R.; Zhu, Z.; Gerber, E.; Pizzochero, M.; Kucukbenli, E.; Schleder, G. R.; Angeli, M.; Watanabe, K.; et al. Domain-Dependent Surface Adhesion in Twisted Few-Layer Graphene: Platform for Moiré-Assisted Chemistry. *Nano Lett.* **2023**, *23*, 3137−3143.

(256) Weston, A.; Castanon, E. G.; Enaldiev, V.; Ferreira, F.; Bhattacharjee, S.; Xu, S.; Corte-León, H.; Wu, Z.; Clark, N.; Summerfield, A.; et al. Interfacial Ferroelectricity in Marginally Twisted 2D Semiconductors. *Nat. Nanotechnol.* **2022**, *17*, 390−395.

(257) Bian, R.; Cao, G.; Pan, E.; Liu, Q.; Li, Z.; Liang, L.; Wu, Q.; Ang, L. K.; Li, W.; Zhao, X.; Liu, F. High-Performance Sliding Ferroelectric Transistor Based on Schottky Barrier Tuning. *Nano Lett.* **2023**, *23*, 4595−4601.

(258) Wu, J.; Chen, H. Y.; Yang, N.; Cao, J.; Yan, X.; Liu, F.; Sun, Q.; Ling, X.; Guo, J.; Wang, H. High Tunnelling Electroresistance in a Ferroelectric van Der Waals Heterojunction via Giant Barrier Height Modulation. *Nat. Electron.* **2020**, *3*, 466−472.

(259) Ma, J.; Gu, Q.; Liu, Y.; Lai, J.; Yu, P.; Zhuo, X.; Liu, Z.; Chen, J. H.; Feng, J.; Sun, D. Nonlinear Photoresponse of Type-II Weyl Semimetals. *Nat. Mater.* **2019**, *18*, 476−481.

(260) Chen, G.; Jiang, L.; Wu, S.; Lyu, B.; Li, H.; Chittari, B. L.; Watanabe, K.; Taniguchi, T.; Shi, Z.; Jung, J.; et al. Evidence of a Gate-Tunable Mott Insulator in a Trilayer Graphene Moiré Superlattice. *Nat. Phys.* **2019**, *15*, 237−241.

(261) Wang, H.; Qian, X. Ferroelectric Nonlinear Anomalous Hall Effect in Few-Layer WTe2. *NPJ. Comput. Mater.* **2019**, *5*, 119.

(262) Yang, J.; Zhou, J.; Lu, J.; Luo, Z.; Yang, J.; Shen, L. Giant Tunnelling Electroresistance through 2D Sliding Ferroelectric Materials. *Mater. Horiz.* **2022**, *9*, 1422−1430.

(263) Velev, J. P.; Burton, J. D.; Zhuravlev, M. Y.; Tsymbal, E. Y. Predictive Modelling of Ferroelectric Tunnel Junctions. *npj Comput. Mater.* **2016**, *2*, 16009.

(264) Luo, B.; Ma, X.; Liu, J.; Wu, W.; Yu, X.; Hu, S.; Gao, H.; Jia, F.; Ren, W. Enhanced Photogalvanic Effect in a 2D Ferroelectric ZrI2 by Interlayer Sliding. *Physica E. Low Dimens. Syst. Nanostruct.* **2022**, *142*, 115297.

(265) Yang, D.; Wu, J.; Zhou, B. T.; Liang, J.; Ideue, T.; Siu, T.; Awan, K. M.; Watanabe, K.; Taniguchi, T.; Iwasa, Y.; et al. Spontaneous-Polarization-Induced Photovoltaic Effect in Rhombohedrally Stacked MoS2. *Nat. Photonics* **2022**, *16*, 469−474.

(266) Wu, J.; Yang, D.; Liang, J.; Werner, M.; Ostroumov, E.; Xiao, Y.; Watanabe, K.; Taniguchi, T.; Dadap, J. I.; Jones, D.; et al. Ultrafast Response of Spontaneous Photovoltaic Effect in 3R-MoS$_2$ -Based Heterostructures. *Sci. Adv.* **2022**, *8*, No. eade3759.

(267) Yu, H.; Liu, G.-B.; Tang, J.; Xu, X.; Yao, W. Moiré Excitons: From Programmable Quantum Emitter Arrays to Spin-Orbit-Coupled Artificial Lattices. *Sci. Adv.* **2017**, *3*, No. e1701696.

(268) Baek, H.; Brotons-Gisbert, M.; Koong, Z. X.; Campbell, A.; Rambach, M.; Watanabe, K.; Taniguchi, T.; Gerardot, B. D. Highly Energy-Tunable Quantum Light from Moiré-Trapped Excitons. *Sci. Adv.* **2020**, *6*, 8526−8537.

(269) Roch, J. G.; Leisgang, N.; Froehlicher, G.; Makk, P.; Watanabe, K.; Taniguchi, T.; Schönenberger, C.; Warburton, R. J. Quantum-Confined Stark Effect in a MoS2Monolayer van Der Waals Heterostructure. *Nano Lett.* **2018**, *18*, 1070−1074.

(270) Brotons-Gisbert, M.; Branny, A.; Kumar, S.; Picard, R.; Proux, R.; Gray, M.; Burch, K. S.; Watanabe, K.; Taniguchi, T.; Gerardot, B. D. Coulomb Blockade in an Atomically Thin Quantum Dot Coupled to a Tunable Fermi Reservoir. *Nat. Nanotechnol.* **2019**, *14*, 442−446.

(271) Zheng, H.; Wu, B.; Li, S.; Ding, J.; He, J.; Liu, Z.; Wang, C. T.; Wang, J. T.; Pan, A.; Liu, Y. Localization-Enhanced Moiré Exciton in Twisted Transition Metal Dichalcogenide Heterotrilayer Superlattices. *Light Sci. Appl.* **2023**, *12*, 117.

(272) Lin, Q.; Fang, H.; Liu, Y.; Zhang, Y.; Fischer, M.; Li, J.; Hagel, J.; Brem, S.; Malic, E.; Stenger, N.; Sun, Z.; Wubs, M.; Xiao, S. A Room-Temperature Moiré Interlayer Exciton Laser. *arXiv* **2023**; DOI: 10.48550/arXiv.2302.01266 (accessed 2023-07-25).

(273) Mao, X. R.; Shao, Z. K.; Luan, H. Y.; Wang, S. L.; Ma, R. M. Magic-Angle Lasers in Nanostructured Moiré Superlattice. *Nat. Nanotechnol.* **2021**, *16*, 1099−1105.

(274) Mak, K. F.; Lee, C.; Hone, J.; Shan, J.; Heinz, T. F. Atomically Thin MoS2: A New Direct-Gap Semiconductor. *Phys. Rev. Lett.* **2010**, *105*, 136805.

(275) Xiong, L.; Tang, T.; Fan, X.; Liu, H.; Zhu, P.; Zhang, X.; Qiao, W.; Wang, Q.; Wang, Z.; Niu, B.; et al. Twist Angle-Dependent Interlayer Exciton in MoS2 Bilayers Revealed by Room-Temperature Reflectance. *Crystals (Basel)* **2022**, *12*, 761.

(276) Zhang, Y.; Zhan, Z.; Guinea, F.; Silva-Guillen, J. A.; Yuan, S. Tuning Band Gaps in Twisted Bilayer Mo S2. *Phys. Rev. B* **2020**, *102*, 235418.

(277) He, J.; Hummer, K.; Franchini, C. Stacking Effects on the Electronic and Optical Properties of Bilayer Transition Metal Dichalcogenides MoS2, MoSe2, WS2, and WSe2. *Phys. Rev. B* **2014**, *89*, 075409.

(278) Han, Y.; Gao, L.; Zhou, J.; Hou, Y.; Jia, Y.; Cao, K.; Duan, K.; Lu, Y. Deep Elastic Strain Engineering of 2D Materials and Their Twisted Bilayers. *ACS Appl. Mater. Interfaces.* **2022**, *14*, 8655−8663.

(279) Terrones, H.; López-Urías, F.; Terrones, M. Novel Hetero-Layered Materials with Tunable Direct Band Gaps by Sandwiching Different Metal Disulfides and Diselenides. *Sci. Rep.* **2013**, *3*, 1549.

(280) Khlyustova, A.; Sirotkin, N.; Kusova, T.; Kraev, A.; Titov, V.; Agafonov, A. Doped TiO2: The Effect of Doping Elements on Photocatalytic Activity. *Mater. Adv.* **2020**, *1*, 1193−1201.

(281) Qian, Z.; Yan, Y.; Liang, Z.; Zhuang, X.; Zhang, K. A. I. Enhancing Charge Separation in Conjugated Microporous Polymers for Efficient Photocatalytic Hydrogen Evolution. *Mater. Adv.* **2021**, *2*, 7379−7383.

(282) Dean, C. R.; Wang, L.; Maher, P.; Forsythe, C.; Ghahari, F.; Gao, Y.; Katoch, J.; Ishigami, M.; Moon, P.; Koshino, M.; et al. Hofstadter's Butterfly and the Fractal Quantum Hall Effect in Moiré Superlattices. *Nature* **2013**, *497*, 598−602.

(283) Hunt, B.; Sanchez-Yamagishi, J. D.; Young, A. F.; Yankowitz, M.; LeRoy, B. J.; Watanabe, K.; Taniguchi, T.; Moon, P.; Koshino, M.; Jarillo-Herrero, P.; et al. Massive Dirac Fermions and Hofstadter Butterfly in a van Der Waals Heterostructure. *Science* **2013**, *340*, 1427−1430.

(284) Bistritzer, R.; MacDonald, A. H. Moiré Bands in Twisted Double-Layer Graphene. *Proc. Natl. Acad. Sci. U. S. A.* **2011**, *108*, 12233−12237.

(285) Yu, Y.; Zhang, K.; Parks, H.; Babar, M.; Carr, S.; Craig, I. M.; Van Winkle, M.; Lyssenko, A.; Taniguchi, T.; Watanabe, K.; et al. Tunable Angle-Dependent Electrochemistry at Twisted Bilayer Graphene with Moiré Flat Bands. *Nat. Chem.* **2022**, *14*, 267−273.

(286) Daviddi, E.; Gonos, K. L.; Colburn, A. W.; Bentley, C. L.; Unwin, P. R. Scanning Electrochemical Cell Microscopy (SECCM) Chronopotentiometry: Development and Applications in Electroanalysis and Electrocatalysis. *Anal. Chem.* **2019**, *91*, 9229−9237.

(287) Aikens, D. A. Electrochemical Methods, Fundamentals and Applications. *J. Chem. Educ.* **1983**, *60*, A25.

(288) Zhang, K.; Yu, Y.; Carr, S.; Babar, M.; Zhu, Z.; Kim, B. J.; Groschner, C.; Khaloo, N.; Taniguchi, T.; Watanabe, K.; et al. Anomalous Interfacial Electron-Transfer Kinetics in Twisted Trilayer Graphene Caused by Layer-Specific Localization. *ACS Cent. Sci.* **2023**, *9*, 1119−1128.

(289) Kim, K. S.; Lee, D.; Chang, C. S.; Seo, S.; Hu, Y.; Cha, S.; Kim, H.; Shin, J.; Lee, J. H.; Lee, S.; et al. Non-Epitaxial Single-Crystal 2D Material Growth by Geometric Confinement. *Nature* **2023**, *614*, 88−94.

(290) Lee, J.-H.; Lee, E. K.; Joo, W.-J.; Jang, Y.; Kim, B.-S.; Lim, J. Y.; Choi, S.-H.; Ahn, S. J.; Ahn, J. R.; Park, M.-H.; et al. Wafer-Scale Growth of Single-Crystal Monolayer Graphene on Reusable Hydrogen-Terminated Germanium. *Science* **2014**, *344*, 286−289.

(291) Li, J.; Chen, M.; Samad, A.; Dong, H.; Ray, A.; Zhang, J.; Jiang, X.; Schwingenschlögl, U.; Domke, J.; Chen, C.; et al. Wafer-Scale Single-Crystal Monolayer Graphene Grown on Sapphire Substrate. *Nat. Mater.* **2022**, *21*, 740−747.

(292) Li, T.; Guo, W.; Ma, L.; Li, W.; Yu, Z.; Han, Z.; Gao, S.; Liu, L.; Fan, D.; Wang, Z.; et al. Epitaxial Growth of Wafer-Scale Molybdenum Disulfide Semiconductor Single Crystals on Sapphire. *Nat. Nanotechnol.* **2021**, *16*, 1201−1207.

(293) Naik, M. H.; Regan, E. C.; Zhang, Z.; Chan, Y. H.; Li, Z.; Wang, D.; Yoon, Y.; Ong, C. S.; Zhao, W.; Zhao, S.; et al. Intralayer Charge-Transfer Moiré Excitons in van Der Waals Superlattices. *Nature* **2022**, *609*, 52−57.

(294) Strasser, A.; Wang, H.; Qian, X. Nonlinear Optical and Photocurrent Responses in Janus MoSSe Monolayer and MoS2-MoSSe van Der Waals Heterostructure. *Nano Lett.* **2022**, *22*, 4145−4152.

(295) He, C.; Chao, H.; Wu, R.; Li, S.; Lei, Q.; Cao, X.; Cao, Z.; Zhu, L.; Wang, H.; Zhao, Q.; et al. Structural Symmetry-Breaking-Driven Giant Optical Second Harmonic Generation in Janus Monolayer ReSSe. *J. Phys. Chem. C* **2023**, *127*, 14991−14998.

(296) Pike, N. A.; Pachter, R. Angular Dependence of the Second-Order Nonlinear Optical Response in Janus Transition Metal Dichalcogenide Monolayers. *J. Phys. Chem. C* **2022**, *126*, 16243−16252.

(297) Bian, C.; Shi, J.; Liu, X.; Yang, Y.; Yang, H.; Gao, H. Optical Second-Harmonic Generation of Janus MoSSe Monolayer. *Chin. Phys. B* **2022**, *31*, 097304.

(298) Wei, Y.; Xu, X.; Wang, S.; Li, W.; Jiang, Y. Second Harmonic Generation in Janus MoSSe a Monolayer and Stacked Bulk with

Vertical Asymmetry. *Phys. Chem. Chem. Phys.* **2019**, *21*, 21022−21029.

(299) Wu, Q.; Xue, Y.; Chao, S.; Wu, F.; Li, L.; Javed, M. S.; Zhang, W. Moiré Superlattice MXene Nanosheets Constructed from Twisted Hexagon-Ti3AlC2 by Microwave-Assisted Lewis Molten Salt Etching: Implications for Structural Stability in Electrochemical Energy Storage. *ACS Appl. Nano. Mater.* **2023**, *6*, 677−684.

(300) Wu, Q.; Xue, Y.; Chao, S.; Wu, F.; Javed, M. S.; Li, L.; Zhang, W. Moiré-Superlattice MXenes Enabled Ultra-Stable K-Ion Storage in Neutral Electrolyte. *Nano. Res.* **2023**, *16*, 5006−5017.